Czech Technical University in Prague
Faculty of Electrical Engineering

# Doctoral Thesis

January 2019

Jan Bednář

Czech Technical University in Prague
Faculty of Electrical Engineering
Department of Radioelectronics

# Quality Evaluation Methods for Advanced Optical Materials

Doctoral Thesis

*Ing. Jan Bednář*

Prague, January 2019

Ph.D. Programme: Electrical Engineering and Information Technology
Branch of study: Radioelectronics

Supervisor: Prof. Mgr. Petr Páta, Ph.D.

**Supervisor:**
Prof. Mgr. Petr Páta, Ph.D.
Department of Radioelectronics
Faculty of Electrical Engineering
Czech Technical University in Prague
Technická 2
166 27 Prague 6
Czech Republic

# Declaration

I hereby declare that I worked out the presented thesis independently and I quoted all the sources used in this thesis in accord with Methodical instructions about ethical principles for writing academic thesis.

*Praha, 31 January 2019* Jan Bednář

# Acknowledgements

I want to thank my supervisor Prof. Mgr. Petr Páta, Ph.D. for the support of my Ph.D. study, for his guidance and his great patience. I would also like to thank Prof Ing. Miloš Klíma, CSc. for his inspiring comments to all researches, great insight and life experiences. Special thanks to all my present and former colleagues from the Department of Radioelectronics for everyday discussions and motivations. Special thanks to Mgr. Martin Blažek, Ph.D. for being my role model and for luring me to the Ph.D. study. I want to thank my mother and brother for supporting me all the time in my life.

This work was partially supported by Grant no. SGS18/141/OHK3/2T/13 "Analysis and advanced algorithms for ultra-wide imaging systems", SGS16/165/OHK3/2T/13 "Algorithms for Advanced Modeling and Analysis of Optical Systems with Variable Impulse Response" and SGS13/212/OHK3/3T/13 "Advanced Algorithms for Processing and Analysis of Scientific Image Data" of the Student Grant Agency of the Czech technical university and by Grant No. GA14-25251S "Nonlinear imaging systems with spatially variant point spread function", and GA17-05840S "Multicriteria Optimization of Shift-Variant Imaging Systems" of The Grant Agency of the Czech Republic.

Praha, 31 January 2019 Jan Bednář

# Abstract

The doctoral thesis under the title Quality Evaluation Methods for Advanced Optical Materials is focused on describing and developing methods for defining the quality of optical material with advanced properties. The material of interest for the evaluation is Calomel. It is a birefringent, uniaxial optical material with prospective use in LWIR range of optics to build polarisers or an AOTF. The thesis is focused on selecting methods to test the quality of the material for use methods in the production of the material. The thesis presents approaches based on optical scattering, conoscopy imaging, a traditional imaging method for PSF/MTF description, surface interferometry and techniques based on Optical Fourier transformation. A new method for quality evaluation based on OFT is presented, the OFT details are described, and spatial optical filtration of the image is presented. The setup for realising the OFT methods is detaily described, with automatic software control and method for analysing the spatial spectrum images. The presented methods are then compared with a proposed new one.

**Keywords:** Advanced materials, Calomel, Optical Fourier Transform, Conoscopy

# Abstrakt

Dizertační práce na téma Metody hodnocení moderních optických materiálů je zaměřena na popis a vývoj metod pro hodnocení kvality optických materiálů pro pokročilé aplikace. Tato práce je zaměřena optický materiál Kalomel (chlorid rtuťný). Jedná se o dvojlomný, opticky jednoosý materiál s perspektivním využitím ve vzdálené infračervené oblasti LWIR ke konstrukci např. polarizátorů nebo akustooptických laditelných filtrů (AOTF). Dizertační práce se zaměřuje na výběr metod vhodných pro měření kvality materiálu s ohledem na možné využití metod při produkci tohoto materiálu. Práce presentuje metody založené na různých přístupech, kterými jsou rozptyl světla, konoskopická analýza, popis pomocí PSF či MTF zobrazovací soustavy, interferometrické metody měření tvaru povrchu materiálu a Optická Fourierova transformace (OFT). Jsou představeny nové metody hodnocení kvality založené na OFT. OFT je detailně představena včetně demonstrace optické filtrace v prostorové doméně. V práci je prezentován optický měřící systém založený na OFT, který je realizován včetně měřicího programového vybavení. Je představena metoda pro analýzu Fourierovského prostorového spektra obrazu. Vybrané metody jsou pak porovnány s metodou na bázi OFT.

**Klíčová slova:** Pokročilé materiály, Calomel, Optická Fourierova transformace, Konoskopie

# Contents

# List of Figures

# List of Tables

# Glossary

**DC**

**DEMON** Development of Quality Evaluation Methods for Calomel Optical Elements

**DFT** Discrete Fourier Transformation

**ESF** Edge Spread Function

**FFT** Fast Fourier Transformation

**FT** Fourier Transformation

**HDR** High Dynamic Range

**HP** High Pass

**LF** Low Frequency

**LP** Low Pass

**LSF** Line Spread Function

**MTF** Module Transfer Function

**OFT** Optical Fourier Transformation

**OTF** Optical Transfer Function

**PDF** Portable Document Format

**PSF** Point Spread Function

**PTF** Phase Transfer Function

**SAD** Scratch and Digs

**SDR** Standard Dynamic Range

**SNR** Signal to Noise Ratio

**STFT** Short Time Fourier Transformation

**SVPSF** Space-Variant Point Spread Function

**TIS** Total Integrated Scatter

**UWFOV** Ultra-Wide Field-of-View

**XML** Extensible Markup Language

# Introduction

In everyday life, we all are surrounded by optical devices of a different type and usage: small photography cameras with multiple chips and advanced image processing in our cell-phones, security and surveillance cameras, TV and video production cameras, optical communications, biomedicine imaging, astronomy and all other science areas. All these applications require more or less high-quality imaging or high spatial resolution. There is a wide range of optical systems based on special properties, construction or on special of light and material, like Ultra-Wide Field-of-View (UWFOV) systems, devices containing unique optical materials, e.g. Calomel or based on e.g. acousto-optics (AO) interaction.

The UWFOV systems are used in microscopy, security cameras or all-sky cameras. The wide angle of the system comes with a large number of aberrations. This affects observed objects and makes image processing e.g. for astrometry and photometry complicated. Systems based on AO interaction are used in optical communication, laser optics or hyperspectral imaging. In general, optical systems can be described with its Point Spread Function (PSF). But, due to the optical design and material properties of the components, these systems have a spatial dependency of the PSF, that is, they have Space-Variant Point Spread Function (SVPSF). Description of such systems is currently not perfectly addressed. This thesis deals with one of the parts affecting the PSF of the optical system, i.e. its performance, on the material quality. It focuses especially on the quality of Calomel crystals. The Calomel is a promising material for applications in the long wave infrared region (LWIR) like hyperspectral imaging or polarizers. This material was until recently exclusively produced by the czech company BBT-Materials Processing Ltd. and our research group on Czech Technical University is cooperating with BBT on projects focused on this material, its properties, quality testing for optical components production and optical device design, i.e. DEMON[15] and THETIS[16].

## Aims of the Doctoral Thesis

1. Selection and description of multiple methods for testing the quality of optical materials concerning Calomel, as a promising modern material, and ability to use methods in the material production process.

2. Propose a new method and quality evaluation metric based on described methods.

3. Compare selected methods to the proposed method.

## Structure of the Doctoral Thesis

The thesis is organised into six chapters as follows:

1. *State-of-the-Art:* Chapter 1 establishes the position of the thesis in the field of optics design, optics materials and quality evaluation.

2. *Advanced Optical Materials:* Chapter 2 introduces advanced optical materials used in modern optics. It is focused on Calomel as a promising crystalline material for applications especially in the infrared region like polarisers or depolarisers, waveplates, acousto-optical modulators (AOM) and acousto-optical tunable filters (AOTF).

3. *Methods for Quality Evaluation:* Chapter 3 describes multiple methods which can be used to determinate the quality of the tested materials. With respect to defects appearing in the Calomel influencing the quality of the material, most of these methods are focused on the quality of the crystal volume, one method for the surface quality is also presented. Initial tests of methods are provided. One of the described methods is based on Optical Fourier transformation. The OFT is derived in Section 3.3, its properties are presented and the filtration in the spatial domain is demonstrated.

4. *Quality Evaluation with OFT:* Chapter 4 describes measuring setup based on Optical Fourier transformation (Section 3.3) and provides its detailed description. In this chapter, the novel quality metric called ICQ is described. The described setup was developed in the Development of Quality Evaluation Methods for Calomel Optical Elements project (DEMON)[15] provided by the European Space Agency. In the chapter, the software control for automatic material quality measurement is also presented. The Section 4.5 presents sectorial analysis method for evaluating the crystal spatial spectrum images.

5. *Comparison of Selected Methods:* Chapter 5 compares two methods selected from Chapter3 (Conoscopy, Light scattering) and compares them with the ICQ measurement presented in Chapter 4. These methods are used to measure the quality of multiple Calomel crystal samples, and results from all three methods are compared together.

6. *Conclusion:* The last chapter summarises the results and relates them to the objectives set in the introduction.

# 1 State of the Art

Any optical imaging system can be described by spatial impulse response function, usually referred to as PSF (Point Spread Function). PSF is used to represent aberrations of the system. A similar way to describe the aberration of the system is to represent it with a wavefront deformation. Both descriptions start to be difficult when the described system is a space-variant, i.e. the amount and type of wavefront deformation or PSF shape varies with position in the field of view of the system. Some conventional methods to overcome this use splitting the field of view to multiple parts saying they are spatial invariant in smaller parts.

The standard approach for obtaining the PSF of the system is to model wavefront aberrations using Zernike polynomials introduced by Zernike in [17] and updated by Noll in [18]. The Zernike polynomials are derived for rotationally symmetric space field independent systems. The Hopkins in [19] uses the field dependent wave aberration. The following works use so-called Bi-Zernike polynomials [20]. All these works use Zernike polynomials for rotationally symmetric systems. Janout in [21] presents the PSF estimation algorithm based on obtaining field-dependent expansion coefficients of the Zernike polynomials by fitting real image data of the analysed system using an iterative approach. In [22] Janout presents adaptation of Zernike polynomials to a non-circular aperture. It allows us to investigate and describe even rectangular optical systems, like a square crystal of a tested sample.

The analyse of space-variant systems, i.e. the ultra-wide field system enhances or even enables image analysis like astrometry on images acquired from astronomical systems. The developed system WILLIAM (Wide-field all-sky monitoring system) [23] is an example of such a system. To provide astrometric calibration of the system, also the type of projection is necessary to take into consideration. We have presented in [24] an alternative way to work with data from ultra wide-field systems usable in astrometry. The method is based on pattern recognition in the image and uses Generalised Hough transform (GHT)[25] to search known star patterns (Big dipper), and when we also get the position of the North pole [26] using the Hough transformation (HT)[27], the base of information for astrometry on all-sky images is ready.

The thesis is focused on the evaluation of the quality of optical materials. There are multiple ways and multiple criteria. Traditional quality criteria are based on the evaluation of the surface imperfections caused by the manufacturing or handling process. This is known as “scratch and digs” (SAD) [28]. Some more advanced method is measuring with the Total Integrated Scatter (TIS), which measure light scattered from an optic accomplished using an integrating sphere. The

tested optic is illuminated with a laser beam and all reflected light from the surface is integrated with the sphere [29]. Detailed method to gain the profile of the surface is using the optical profiling method. These methods are based on interferometrical methods and constructions like Fizeau, Twyman-Green or shearing interferometers [30]

Favourite method to evaluate the properties of the crystal volume is Conoscopy. It is used to classification the birefringent materials and to study changes in the material caused, e.g. by the mechanical stress acting on the crystal. The work is focused on a study of optical uniformity of crystals of $TeO_2$ [31] or to study properties of liquid crystals [32]. Interesting work is a study and analysis of isochrome shapes in the conoscopic patterns by Kolesnikov in [33].

# 2 Advanced Optical Materials

In optics, there is often used a lot of materials like paratellurite $TeO2$, lithium niobate $LiNbO_3$ with exciting properties. Such materials are usually anisotropic, nonlinear and manifest effects like Pockels or Kerr electrooptical effect or Acousto-optic interaction. In this thesis, the material of interest is Calomel. This material has advantages in its wide transparency range, high birefringence and ability to acousto-optic interaction.

## 2.1 Calomel

Calomel is a name of a mineral form of chemical compound $Hg_2Cl_2$, also known as mercury chloride. Mercury chloride is a very heavy, soft, white, odourless and tasteless mineral. It was widely used in medicine since the $16^{th}$ century but from beginning the $20^{th}$ century, it is not used due to its toxicity - because of disassociation into mercury and mercuric chloride. In this work, we are using crystalline form of mercury chloride - Calomel[34]. In 1969, the first Calomel single crystal was produced. Calomel has a high index of refraction and high value of birefringence and provides a wide range of optical transmission - it is ideal to use in the infrared region. It also has extremely high values for acoustooptics figures of merit and low velocity of elastic wave propagation. Table 2.1 shows some basic calomel properties.[35] [36]

Calomel properties are caused mainly by the linear chain-like structure, by the high anisotropy of internal bounds and by the nature of extraordinary heavy cations $Hg_2^{2+}$. The elementary cell (Figure 2.1) is composed of linear molecular chains $Cl^- - Hg^+ - Hg^+ - Cl^-$ which are bound together by very weak bonds, dominantly of the Van der Walls type. Due to this structure, all the physical properties - optical, elasto-optic, mechanical, dielectric, etc. - exhibit an outstanding anisotropy.

Calomel is a very promising material for IR applications like MWIR polarizers, waveplates and depolarizers. Due to its mechanical properties, there is application area in the field of Acousto-optical interaction.

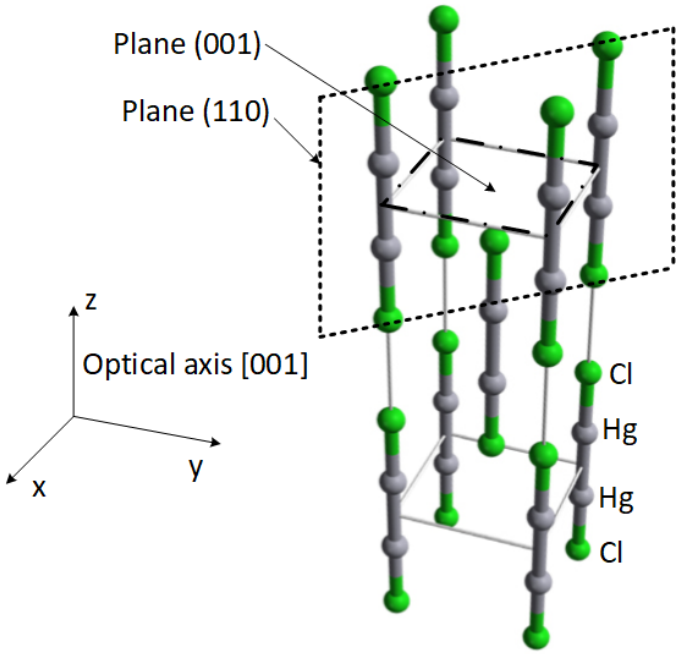


Figure 2.1: Elementary cell of Calomel single crystal.[1]

| | |
|---|---|
| Chemical formula | $Hg_2Cl_2$ |
| Chemical name | Mercurous chloride |
| Mineralogical name | Calomel |
| Crystalographical system | Tetragonal |
| Specific weight $[g \cdot cm^{-3}]$ | 7.18 |
| Vapour tension [Torr] | $10^{-8}$ at 27 °C |
| Index of refraction ($\lambda = 589$nm) | $n_o = 1.973, n_e = 2.656$ |
| Birefringence ($\lambda = 589$nm) | +0.683 |
| Optical transmission [$\mu$m] | 0.38 to 20 |
| Velocity of acoustic wave [m/s] | 347 |
| Acoustooptical figure of merit | $M_2 = 640 \cdot 10^{-15} kg \cdot s^{-3}$ |
| Mohs hardness | 1.5 |

Table 2.1: Basic Properties of Calomel.[12][13]

| Compound | | Density $[g \cdot cm^{-3}]$ | Hardness [Mohs] | Transparency $[\mu m]$ | $n_o$ [-] | $n_e$ [-] | $\Delta n$ [-] | $v_a$ $[kms^{-1}]$ |
|---|---|---|---|---|---|---|---|---|
| Kuzminite | $Hg_2Br_2$ | 7.68 | 1.5 | 0.4 - 30 | 2.12 | 2.98 | 0.86 | 0.27 |
| Calomel | $Hg_2Cl_2$ | 7.15 | 1.5 | 0.36 - 20 | 1.96 | 2.62 | 0.66 | 0.35 |
| Moschelit | $Hg_2I_2$ | 7.68 | 1.5 | 0.45 - 40 | 2.43 | 3.91 | 1.48 | 0.25 |
| Tellurite | $TeO_2$ | 6.00 | 2 | 0.33 - 5 | 2.26 | 2.41 | 0.15 | 0.62 |

Table 2.2: Basic properties of mercurous halides and its comparison to typical representatives of materials used for acoustooptics with common properties $TeO_2$: Name of the compound, chemical formula, density of the material, hardness, transparency range, ordinary and extraordinary index of refraction, birefringence and speed of the acoustic wave. The value is the slowest acoustic speed for the acoustic shear wave in the direction $< 110 >$ for all materials. Index of refraction $n_o, n_e, \Delta n$ for $\lambda = 638nm$. [13][14]

## 2.2 Mercurous Halides

Calomel is a compound from a family of mercurous halides $Hg_2X_2$, where X can be Bromine, Chlorine or Iodine (Br, Cl, I). These compounds have common physical properties given by the same structure of the material and by its anisotropy. Table 2.2 shows the comparison of the main features of the material.

## 2.3 Calomel Quality

There are multiple ways how to describe the quality of the crystal. First, the crystal surface quality has a direct impact on the suitability of use in optical applications. Due to the low crystal hardness, the material can be very easily damaged. For each optical surface, we have to look at these criteria:

- the flatness of the surface,
- the roughness of the surface,
- scratches and digs - mechanical damage,
- more massive mechanical damage, so-called grazes.

Seconds, the main influence on the crystal quality has the inner crystal structure. Defects within the crystal volume can result in changes in its refractive index which causes blurring or optical beam deflections. These defects can be caused by material impurities forming streaks inclusions or bubbles in the crystal or sharp-edged cracks (from the edge of the material to its volume. The structural inhomogeneities may also occur in the form of inclusions in a shape of bubbles. Also,

| Name | Product Nr. | Made | Boule | Polished Surface | Size [mm] |
|---|---|---|---|---|---|
| Sample A | 059.P10.36.2013_114.1993-III | 2013 | 1993 | 2x(110) | 10 x 11 x 17 |
| Sample B | 043.S41.2012_011.2011-I | 2012 | 2011 | 2x(110), 2x(001) | 13 x 13 x 22 |
| Sample C | DEMON1 | 2013 | N/A | 2x(001) | 10.1 x 9.4 x 14 |
| Sample D | DEMON2 | 2013 | N/A | 2x(001) | 10.1 x 9.4 x 14 |
| Sample E | N/A | N/A | N/A | 2x(110) | 20 x 20 x 12 |
| Sample F | N/A | N/A | N/A | 2x(001), 2x(001) | 16.7 x 16 x 26 |
| Sample G | 001.S01.2011_118.1995 | 2011 | 1995 | 2x(110), 2x(001) | 8.5 x 10 x 17.5 |
| Sample H | 019.S17.2012_021.2012-II | 2012 | 2012 | 2x(110), 2x(001) | 14 x 15 x 20 |
| Sample $T_1$ | N/A | N/A | N/A | 2x(110), 2x(001) | 12 x 12 x12 |
| Sample $T_2$ | N/A | N/A | N/A | 2x(110), 2x(001) | 10 x 10 x 11 |

Table 2.3: Properties of Calomel samples used for evaluating. Simplified name, the complete product number of the sample, year of manufacture of the sample, year of production of the boule, polished surfaces of the sample and size of the sample.

mechanical impurities (foreign bodies, spot defects) and chemical impurities (free mercury bubbles, chemical nonstoichiometry and foreign chemical elements presence) may appear.

To evaluate the quality of the material number of methods were tested and a new one was tested. These methods are described in the next sections.

## 2.4 Calomel Samples

To test evaluation methods for quality testing multiple Calomel samples were selected. They differ with their year of manufacture, their original crystal boule, optical orientation, dimensions and number of polished surfaces. All crystals and their properties are in Table 2.3. Some of their properties are unfortunately unknown. To simplify the labelling of the crystal, they were tagged with a simple name. Depending on these properties some samples were not able to be used for all methods.

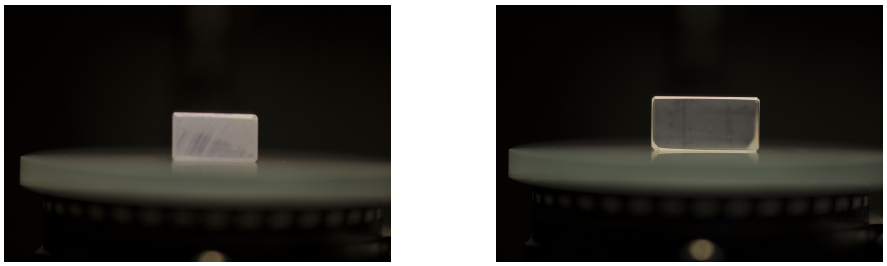

(a) Sample A



(b) Sample B

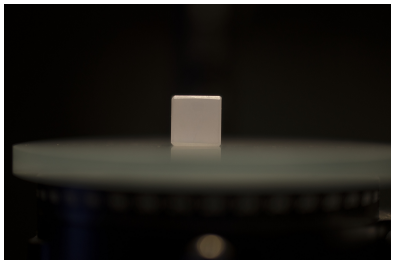

(c) Sample C

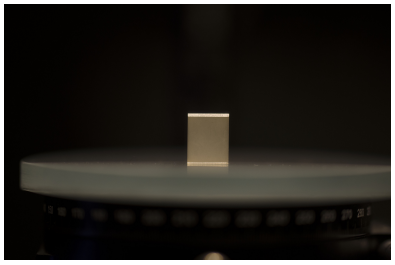

(d) Sample D

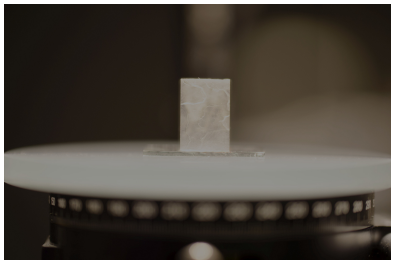

(e) Sample E

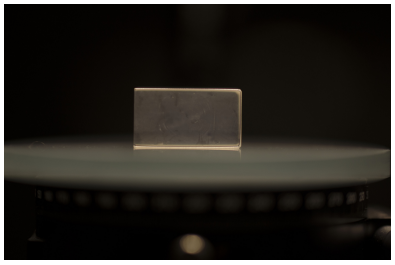

(f) Sample F

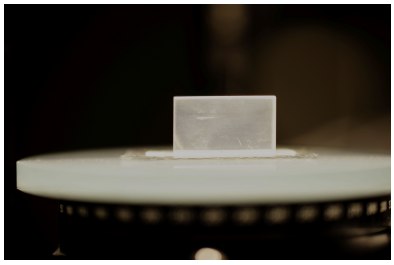

(g) Sample G

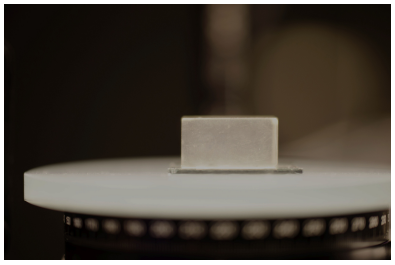

(h) Sample H

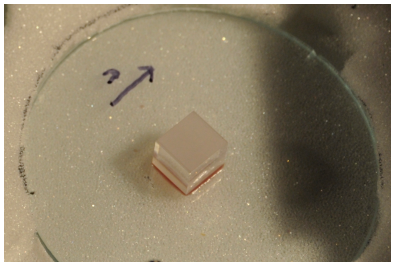

(i) Sample $T_1$

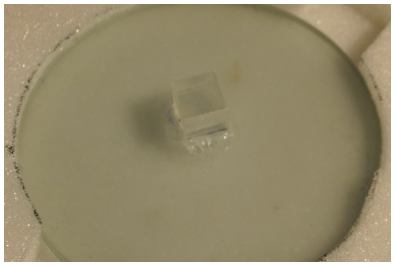

(j) Sample $T_2$

Figure 2.2: All samples A to H are used for methods comparison in Section 5. Samples $T_1$ and $T_2$ are used for initial tests of all methods described in Section 3.

# 3 Methods for Quality Evaluation

There are multiple criteria, that can describe, in some way, the quality of the optical material or properties of the optical element created from the material of our interest. As mentioned in Section 2.3, these criteria can be divided into properties of the surface of the material and properties of the volume of the material. The surface properties are usually described with standard features like the surface flatness, roughness, number of scratches and digs, etc. These are affected by the processing methods of the material, i.e. polishing. In this section, four methods for evaluating the quality of the volume of the material are discussed and one method for surface quality monitoring is also demonstrated.

## 3.1 Light Scattering

Even a light wave goes through a transparent medium with no absorption; still, the light intensity is reduced. The light scattering in the material causes it. The incoming light wave can transmit an amount of the energy to particles. This energy is then irradiated into all directions. This effect depends on the particle size, on the wavelength of the light and it also depends on the type of interaction between light and the particle, namely it is an interaction between electrons in a material and a vector of an electrical intensity of the light. The light scattering corresponds to the homogeneity of the material.

We distinguish between two types of scattering: elastical scattering with no energy losses of the radiation and nonelastic scattering with energy losses. It means, elastical scattered light has the same wavelength as the original wave, nonelastic scattered light has a different wavelength. Elastic scattering is sorted into Rayleigh scattering, Mie scattering and Tyndall effect. The main difference between these effects is a size of scattering particle to a light wavelength.

### 3.1.1 Tyndall Scattering

The light scattering is one of possible optical material quality metrics because the decrease of the material quality decrease is caused by numerous scattering centres. There are several approximations of light scattering on small particles. For our quality evaluations is suitable Tyndalls

approximation of light scattering on particles with a size roughly the same to the optical wavelength or bigger. This effect is similar to the Rayleigh scattering, where the light is scattered on particles much smaller to wavelength. Thought the Rayleigh scattered light increases with the fourth power of radiation frequency, Tyndall effect depends on the second power or radiation frequency.[37][38]

Tyndall effect is observed for scattering centres dimensions from 50 to 1000 nm. Scattering centres are expected to be bubbles, free mercury inclusions or impurity inclusions in the Calomel crystal. The power of the Tyndall effect used for quality measurement is that the scattering is almost negligible in excellent quality materials. Therefore, the experimental setup has to be designed as highly sensitive. The Tyndall scattering is a suitable tool for the evaluation of the crystal bulk optical quality.

### 3.1.2 Optical Setup

Optical setup for this method is shown in Figure 3.1. The crystal is illuminated by the narrow laser beam and the scattered light is measured in the plane perpendicular to the optical beam direction. With respect to the laser beam diameter and size of the crystal, it is necessary to map the volume of the crystal with the beam. Therefore the Calomel sample is placed on a PC controlled XY translational stage. The scattered light from the sample is collected with an integrating lens to a photodetector. There is a spatial mask near the sample used for masking the scattered light from edges of the sample.

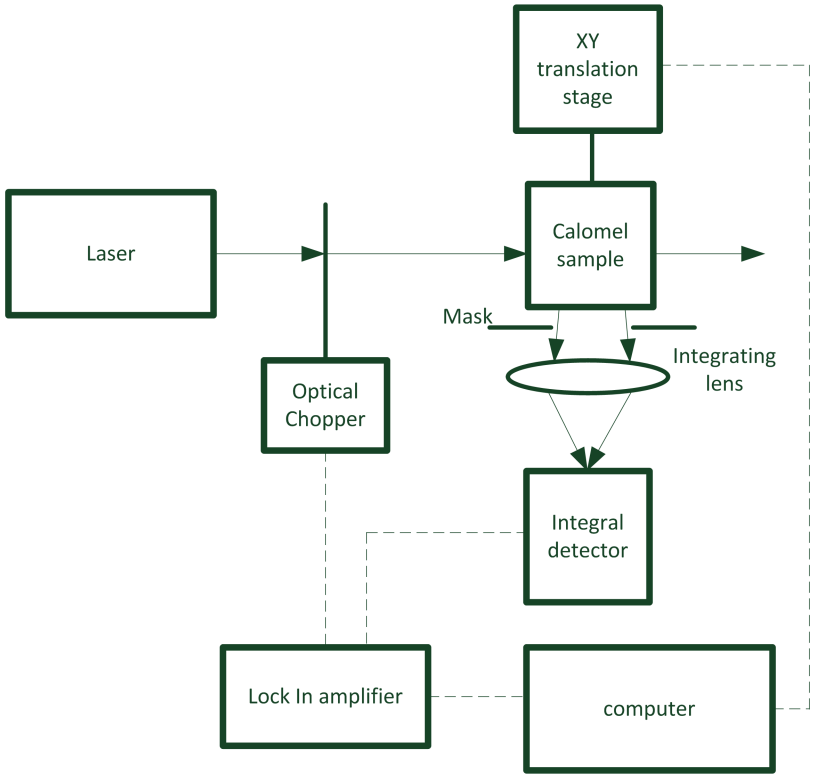


Figure 3.1: Schema of optical setup based on Tyndall effect.

For higher precision and better performance of the system, the synchronous detection (homodyne detection) is used in the system. It consists of an optical chopper and a lock-in amplifier. The chopper chops the laser light with a known reference frequency, thus the scattered light detected by the detector is also chopped. The signal from the detector is then mixed with the reference from the chopper in the lock-in amplifier, and the amplitude of the detected signal is recovered. This solution is very suitable for signal recovery at a low SNR (signal-to-noise) ratios. The high sensitivity and noise immunity are necessary because of the very low scattering level in very high-quality Calomel crystals. The synchronous detection also eliminates the background illumination influence.

Figure 3.2 shows a visible scattering of the light in the volume of a tested sample and also shows how shines edges of the crystal.

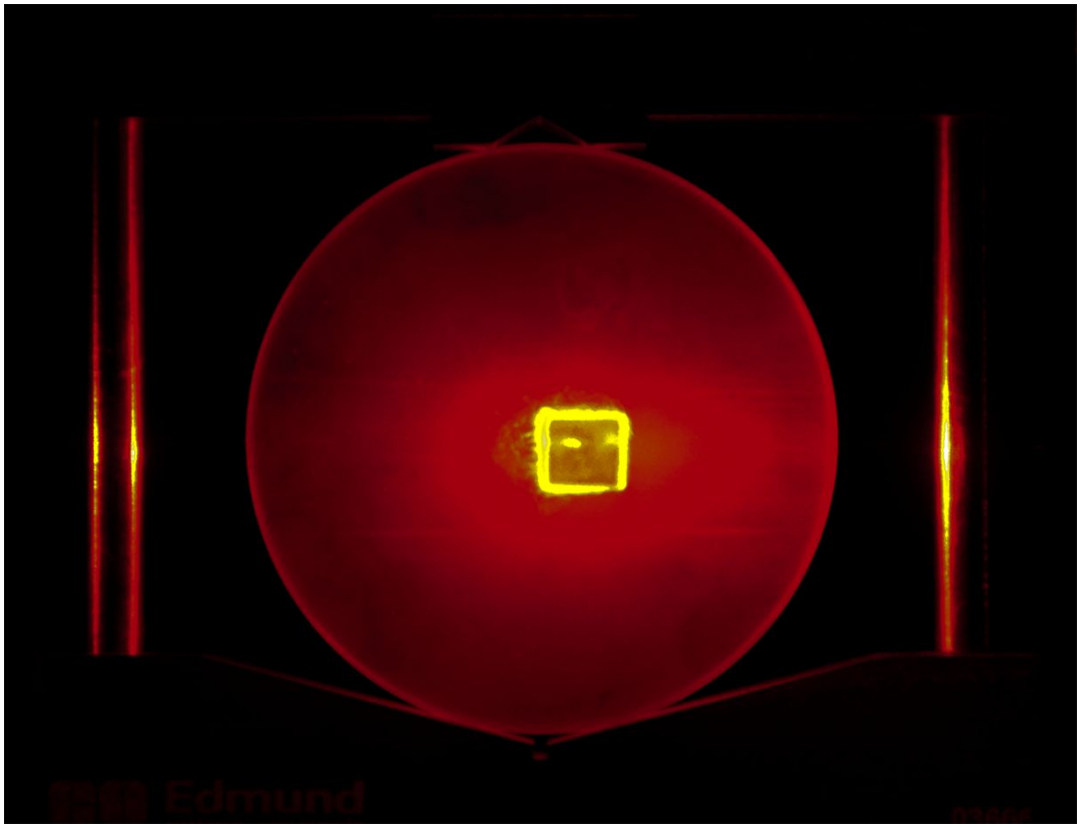

Figure 3.2: Photo of a crystal sample with visible scattering.

The Tyndall scattering can indicate the existence of rough scattering centres such as bubbles or inclusions (mercury or impurities). The bubbles or inclusion causes a significant discontinuity of index of refraction and produces larger scattering. There are two sets of cleavage planes in Calomel which may also lead to the appearance of small cracks in the material. They are frequently close to calomel surface but can appear even in a crystal volume. Impact of such cracks depends on the laser beam orientation to crystal orientation of the sample. Cleavage planes are (110) and (1-10) and cracks are parallel to them. Laser beam directions [110] or [1-10] pass perpendicular to the cracks and scattering is massive. [2]

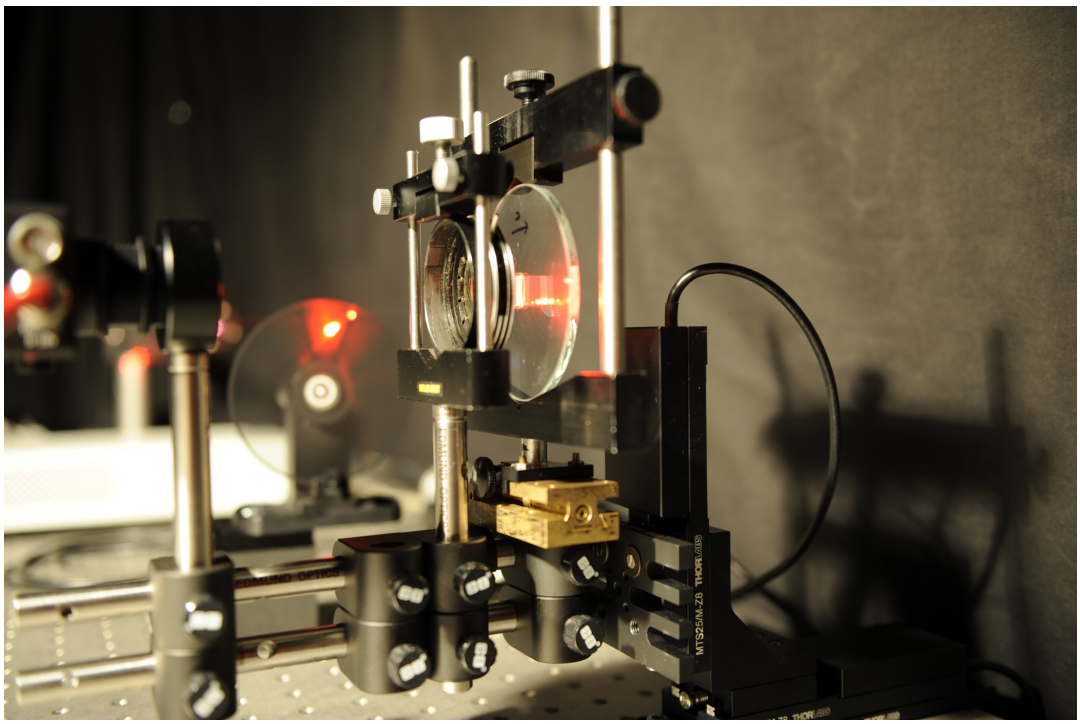


Figure 3.3: Photo of the optical setup with tested sample.

### 3.1.3 Experimental Results

Photo of the experimental setup is shown in Figure 3.4. Tested samples are scanned with a 1 mm steps in a rectangular scan grid and the power of the power of the scattered light is measured in each point. The result is then a scattering map of the tested crystal as shown in Figure 3.4. The amount of scattered light in Test 1 sample is in most part same as in Test 2 sample (there are different colour scales to demonstrate the accuracy of the method). There is a high amount of scattered light in Test 2 sample in the bottom left part of the crystal. The right side of Test 2 crystal also has a high amount of scattering, but in this part, the scanning beam already touched or crossed the edge of the crystal.[2]

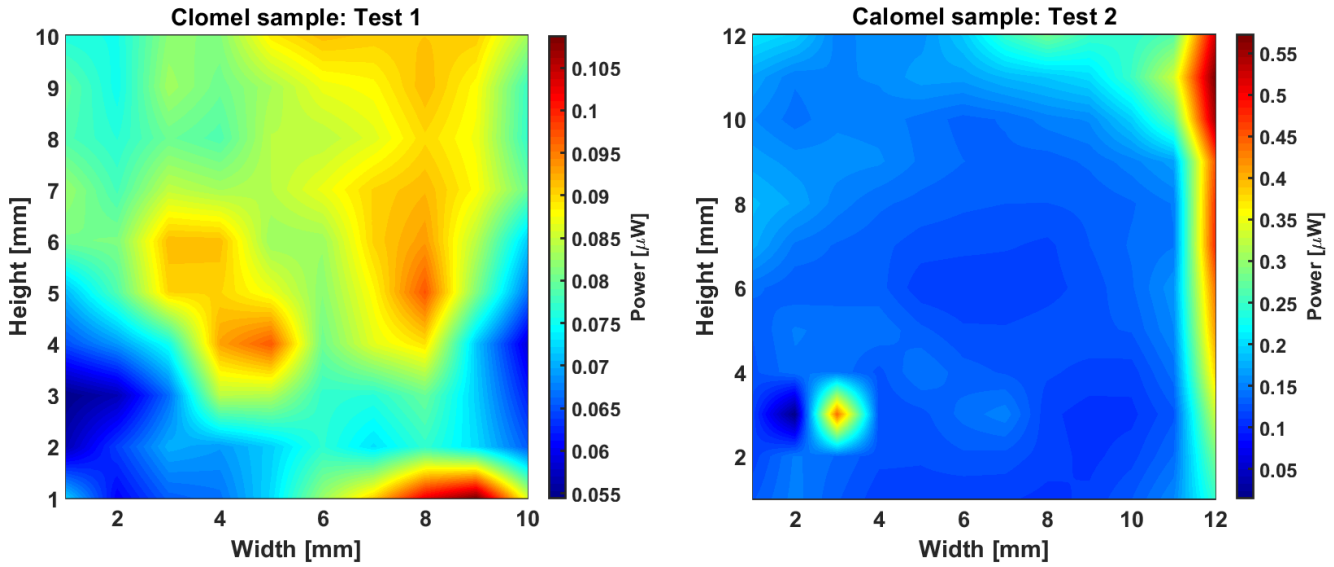


Figure 3.4: Maps of the power of scattered light from tested crystals. Sample Test 1 was measured in 10x10 grid with 1 mm size of the step. Sample Test 2 was measured in 12x12 grid with 1mm size of the step.

## 3.2 Conoscopy

The conoscopic analysis is a standard method for the evaluation of optical birefringent materials. It is very suitable for the assessment of the index of refraction homogeneity and birefringence homogeneity. The homogeneity is essential for application based on the birefringence of the material, i.e. for use in polarising optics or devices using the acousto-optical interaction.

### 3.2.1 Optical Setup

The schema of the optical setup for conoscopic analysis is presented in Figure 3.5. The beam expander expands the laser beam from the HeNe laser (633 nm). Because the conoscopy analysis provides us information over the entire area irradiated by the laser, the expansion ratio (the output beam diameter) has to be selected. It can be set to irradiate the whole aperture of the tested sample or, as in other techniques described in this section (3, the diameter is set to be smaller to provides the possibility of mapping the quality in the whole volume of the tested crystal. The selected output diameter is 5 mm. The lens L1 forms the converging laser beam as it is recommended for the conoscopy. The plane of the polarizer P1 is set to be parallel to the plane of polarisation of the laser and improves the polarisation ratio of the light. The light then passes to the tested crystal in the direction of the optical axis of the crystal [001], i.e. input and output optical planes are (001).

The sample holder is built from two main parts. First, it is equipped with two manual rotation stages. One is used to horizontal rotation of the tested sample; the second is used as a tilting stage. These are used to provide the exact alignment of the optical axis of the sample to the optical axis of the setup. The setting of these stages is done manually according to the Malta cross image sensed by the camera.

Second, the crystal holder is built from two motorised translational stages in the XY configuration. This provides the system with the ability to scan the volume of the sample. The scanning is controlled by the computer to provide the repeatability of the measurement and automatic scanning. For the scanning purposes, the ANSI IT7.215 standard can be adopted. The standard relates to the evaluation of homogeneity of displays. It uses nine points uniformly spread over the active aperture of the sample. Figure 3.6 illustrates the order of the points and XY coordinates used later in this work. It is shown for the observer watching the input surface of the crystal.

The output polarizer P2 is an analyser for the system. It is mounted on a manually rotated holder, and its polarisation plane is set to maximum contrast of the conoscopy image (Malta cross).

The sensed conoscopy image is captured with the camera with a zooming lens. The zoom is adjusted manually and provides the scale transformation of the image. The zoom is useful when varies the thickness of the tested crystal sample; thicker the sample - bigger the conoscopic image. The acquisition of the images is controlled via the computer which controls the scanning of the tested sample volume. [2]

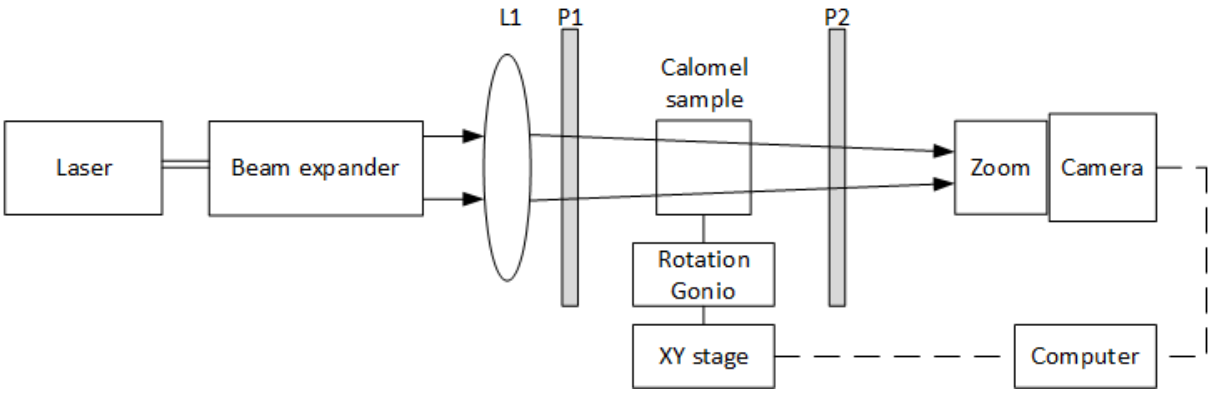


Figure 3.5: Schema of conoscopy setup.[2]

### 3.2.2 Experimental Results

The ideal forms of conoscopic patterns are shown in Figure 3.7. The 3.7a presents the conoscopic image of a uniaxial crystal, resp. 3.7b presents one of possible conoscopic shape for optically biaxial crystal. These conoscopic images are created with the use of white light, not a monochromatic laser. The metalope corresponds to the position of the optical axis.

Calomel is a tetragonal positively uniaxial crystal, and it has a significant value of elastooptic tensor elements. Under an external pressure (deformation) or due to remaining of internal residual stress, the originally uniaxial material can be transformed into a biaxial one. This is detected as a deformation of the conoscopic pattern.

The presented setup (Figure 3.5) provides multiple conoscopic images with the scanning of the tested sample. The output for two different tested samples is presented in Figure 3.8 and 3.9.

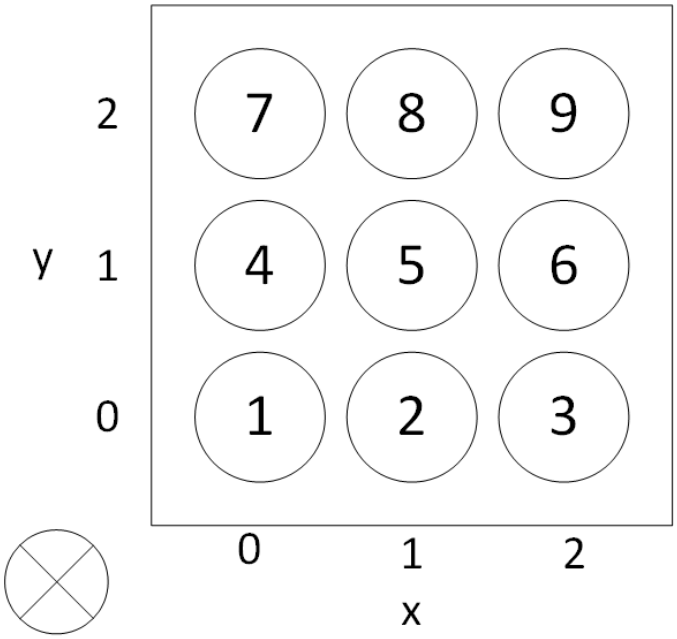


Figure 3.6: Order of points for measurements and their XY coordinates.[2]

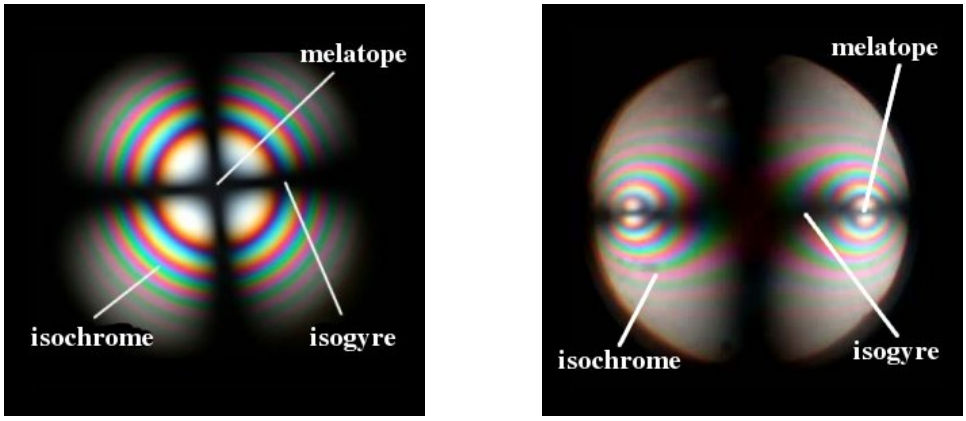


(a) a (b) b

Figure 3.7: White light conoscopy images of a uniaxial (a) and biaxial (b) crystals.[3]

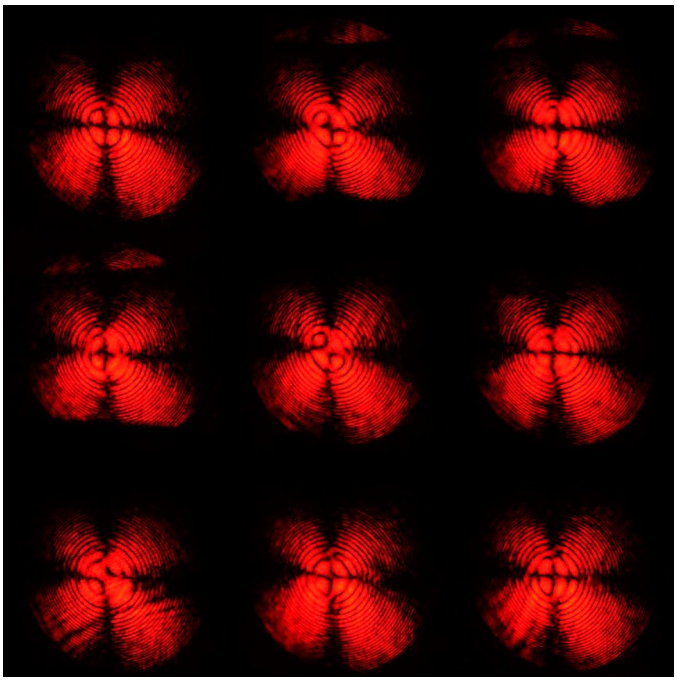

Figure 3.8: Map of conoscopy images, $T_1$ sample.[2]

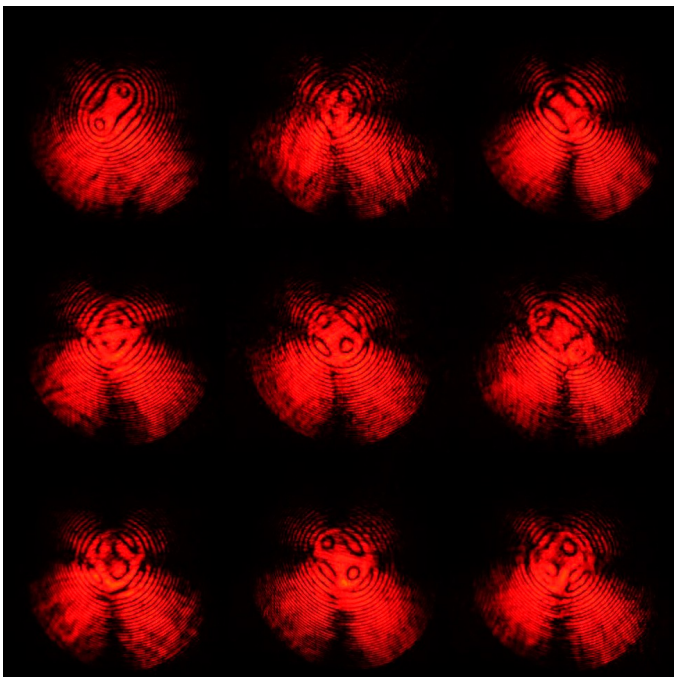

Figure 3.9: Map of conoscopy images, $T_2$ sample.[2]

### 3.2.3 Evaluation Method

The method for evaluation of the conoscopy image is proposed in this section. It utilises the 4-fold symmetry of the conoscopic pattern in the optically uniaxial crystal (Figure 3.7a). The idea is to use two perpendicular profiles of the conoscopic pattern (Figure 3.10) and compare their shape with metric, e.g. correlation function.

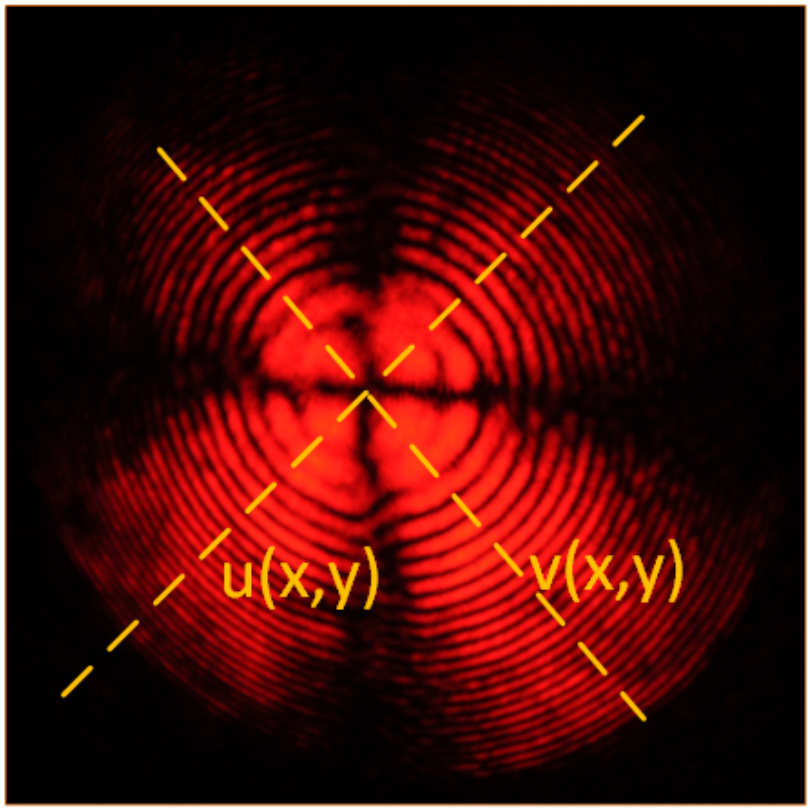


Figure 3.10: Selected profiles in the conoscopic image.

Let $u(x, y)$ and $v(x, y)$ be two perpendicular lines in the image of the conoscopy pattern. It is expected that these lines pass through the metalope, i.e. optical axis. Then the profile functions can be rewritten to the one-dimensional function

$$u(x, y) \to \varphi(\xi) \tag{3.1}$$
$$v(x, y) \to \phi(\xi) \tag{3.2}$$

where $\xi$ is an index of an element in the profile. These profiles can be correlated

$$\varrho_{\varphi\phi}(\xi) \overset{\text{def}}{=} (\varphi \star \phi)(\xi) = \int_{-\infty}^{\infty} \varphi^*(\eta)\phi(\eta + \xi)\mathrm{d}\eta. \tag{3.3}$$

The energy of the correlation function is obtained as

$$E_{\varphi\phi} = \int_{-\infty}^{\infty} |\varrho_{\varphi\phi}(\xi)|^2 \mathrm{d}\xi \tag{3.4}$$

The energy is used as the similarity criterion for the classification of the conoscopy images. Figure 3.11 presents the comparison of two correlation functions from selected conoscopy images from two different samples.

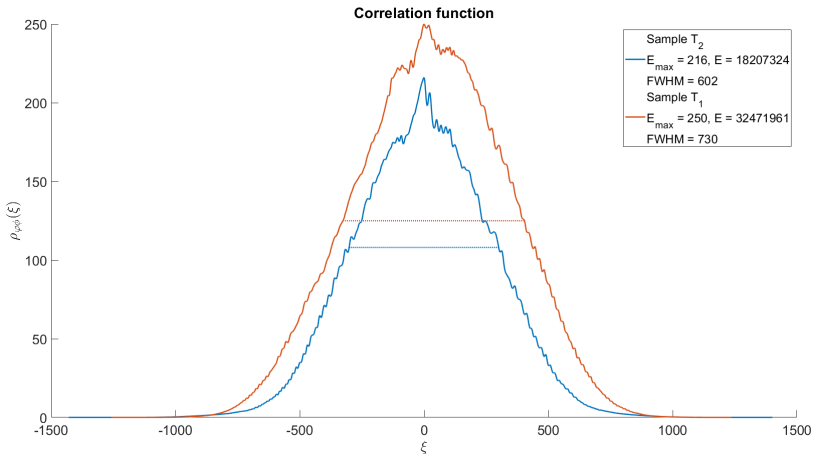


Figure 3.11: Comparison of two correlation functions with maximum energy, energy calculated with equation 3.4 and with FWHM.

## 3.3 Optical Fourier Transformation

Nowadays, Fourier Transformation is used in general in many applications, whether 1-D or n-D signal analysis, e.g. image processing. Even if we are describing Fourier transformation (FT) in all of its typical form, e.g. Discrete Fourier Transformation (DFT) or Short Time Fourier Transformation (STFT), we are always using the algorithm of Fast Fourier Transformation (FFT) when we realise the calculation in the digital domain. But for image processing or optical system analyse, an alternative approach can be used, optical approach. The Fourier Transformation of an image can be made with a simple optical system. The system is also able to process the image, e.g. high pass (HP) or low pass (LP) filtration of the image. The system is performing Optical Fourier Transformation (OFT). The operation of such a system is described later in Section 4.

### 3.3.1 Principle of Fourier Transformation

An essential element of systems realising Optical Fourier Transformation is a focal lens. We can prove, that the distribution of light in the back focal plane of a focal lens corresponds to the Fourier projection of a displayed image. Assume a light wave $W_1$ incoming to the focal lens. This wave is described with intensity distribution of the light $A(x, y)$ and wavefront shape - phase distribution $\varphi(x, y)$ (3.5). In the same way, we can describe the light wave $W_2$ (3.6).(Published in [39]).

$$W_1(x, y) = A_1(x, y) \cdot \mathrm{e}^{\mathrm{i}\varphi_1(x,y)} \tag{3.5}$$
$$W_2(x, y) = A_2(x, y) \cdot \mathrm{e}^{\mathrm{i}\varphi_2(x,y)} \tag{3.6}$$

Using both equations, we can define the transfer function of the focal lens (3.7),

$$t_L(x, y) = \frac{W_2(x, y)}{W_1(x, y)} = \frac{A_2}{A_1} \cdot \mathrm{e}^{\mathrm{i}(\varphi_2 - \varphi_1)} = \begin{cases} a(x, y) \cdot \mathrm{e}^{\mathrm{i}\varphi_L(x,y)}, & (r > \frac{D}{2}) \\ 0, & (r > \frac{D}{2}) \end{cases}, \tag{3.7}$$

where D is the lens diameter and r is the distance from an incidence point of the light on the lens to the optical axis $r = \sqrt{x^2 + y^2}$, $a(x, y)$ is a transition of light wave amplitude. We can assume no optical losses of light intensity in the lens, $a(x, y) = \frac{A_2(x,y)}{A_1(x,y)} \approx 1$. Then, the lens transition is given only with transition of the phase, $t_L(x, y) = e^{\mathrm{i}\varphi_L(x,y)}$. The next assumption is that the projected object is far enough away from the lens, so the light rays are considered to be parallel to the optical axis. We can write the focal lens transition using the image. 3.12.

$$\varphi_L(x, y) = \frac{2\pi}{\lambda} \left[s_1 + s_2 + n \cdot d(x, y)\right] = -\frac{2\pi}{\lambda}(n - 1) \cdot (s_1 + s_2) + \varphi_0. \tag{3.8}$$

The equation $\varphi_0 = \frac{2\pi}{\lambda} n d_0$ describes phase shift given by lens material with refraction index $n$ in dependency of wavelength $\lambda$. This shift is constant for a given wavelength, and it is independent of the light ray position. Therefore, we do not have to take it into account. Expressions $s_1$ and $s_2$ are dependent on coordinates $(x, y)$. If we suppose that curvature radius of both surfaces is much greater than the distance between rays of light and the optical axis, i.e. $x^2 + y^2 \ll r_{1,2}$, we can write the equation for $s_1(x, y)$ and $s_2(x, y)$.

$$s_1(x, y) = r_1 - \sqrt{r_1^2 - (x^2 + y^2)} \approx \frac{x^2 + y^2}{2r_1}, \tag{3.9}$$
$$s_2(x, y) = (-r_2) - \sqrt{(-r_2)^2 - (x^2 + y^2)} \approx -\frac{x^2 + y^2}{2r_2}, \tag{3.10}$$

where $r_1$ and $r_2$ are curvature radii.

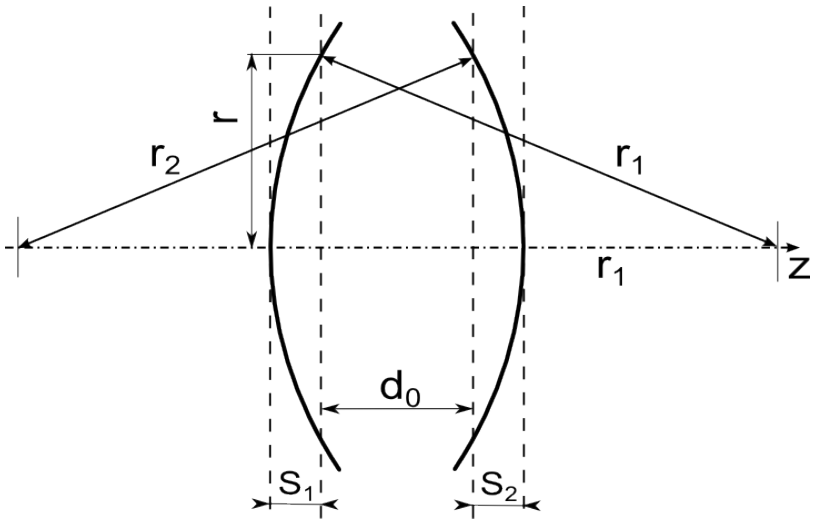


Figure 3.12: Deriving of the focal lens transition.[4]

The phase transition of the lens is expressed after substitution of (3.9) and (3.10) into equation (3.8) as

$$\varphi_L(x,y) = -\frac{2\pi}{\lambda}\left(\frac{1}{r_1}-\frac{1}{r_2}\right)(x^2+y^2) = -k\frac{x^2+y^2}{2f}, \tag{3.11}$$

$$f = \frac{1}{(n-1)\left(\frac{1}{r_1}-\frac{1}{r_2}\right)}, \tag{3.12}$$

where $k = \frac{2\pi}{\lambda}$ is the wave number and $f$ is the focal length of the lens (3.12). After substituting to the equation of the transfer function of the focal lens (3.7) we get the final form of the transfer function,

$$t_L = \mathrm{e}^{\mathrm{i}\varphi_L(x,y)} = \mathrm{e}^{-\mathrm{i}k\frac{x^2+y^2}{2f}}. \tag{3.13}$$

The transfer function of the lens depends on a focal length of a lens $f$, on coordinates $(x, y)$ of the light ray according to the optical axis and on the wavelength $\lambda$ or wave number $k$.

Let us have a point of the source object with coordinates $(x_1, y_1, z_1)$. This is a point source of light. The point is a source of the spherical light wave. According to the premise of light rays parallel to the optical axis and according to the premise of distance $z \gg \sqrt{x^2+y^2}$ large enough from the object to the lens, we can approximate the spherical wave with a parabola (Fresnel approximation)(3.14). The equation (3.15) now describes the wave $W_1$ in the point with coordinates $(x, y, y)$

$$W(x,y,z) = \frac{A(x,y)}{z} \cdot \mathrm{e}^{-\mathrm{i}kz} \cdot \mathrm{e}^{-\mathrm{i}k\frac{x^2+y^2}{2z}} \tag{3.14}$$

$$W_1(x,y,z) = A_1(x_1,y_1) \cdot \mathrm{e}^{\mathrm{i}k\frac{x^2+y^2}{2z_1} - \frac{xx_I+yy_I}{z_1} + \frac{x_1^2+y_1^2}{2z_1}} \tag{3.15}$$

The last part in the exponent in (3.15) can be omitted ($z_1 \gg \sqrt{x_1^2+y_1^2}$). When the distance from the object to the lens is equal to focal length $z_1 = f$, then a projection of the wave $W_1$ to the wave $W_2$ is

$$W_2(x,y) = W_1 \cdot t_L = A_1(x_1,y_1) \cdot \mathrm{e}^{\mathrm{i}k\frac{x^2+y^2}{2f} - \frac{xx_1+yy_1}{f}} \cdot \mathrm{e}^{-\mathrm{i}k\frac{x^2+y^2}{2f}} \tag{3.16}$$

$$= A_1(x_1,y_1) \cdot \mathrm{e}^{-\mathrm{i}k\frac{xx_1+yy_1}{f}}. \tag{3.17}$$

The expression (3.17) represents the projection of a point source from an object plane of the lens to its back image plane. But the point source represents only one point of the entire imaged object. For a complete image of an object, we have to determine contributions from all points on the object. A sum of all contributions gives the complete image,

$$W_2(x,y) = \iint_{-\infty}^{+\infty} W_1(x_1,y_1)\mathrm{e}^{-\mathrm{i}k\frac{xx_1+yy_1}{f}}\mathrm{d}x_1\mathrm{d}y_1. \tag{3.18}$$

Lets look on the equation for 2-dimensional Fourier transformation of a function $g(x,y)$,

$$\mathcal{F}\{g(x,y)\} = G(\omega_x,\omega_y) = \iint_{-\infty}^{+\infty} g(x,y)\mathrm{e}^{-\mathrm{i}(x\omega_x+y\omega_y)}\mathrm{d}x\mathrm{d}y. \tag{3.19}$$

If we compare equations (3.18) and (3.19) we see that wave $W_2$ in back focal plane of the focal lens corresponds to 2D Fourier transformation of an object.

Coordinates $(x,y)$ corresponds to space frequencies $(\omega_x,\omega_y)$. They are given by $\omega_x = k\frac{x}{f}$ and $\omega_y = k\frac{y}{f}$. If we replace direction of light propagation, we can see the focal lens transforms the Fourier image of the object back to the original object; the focal lens is also able to make Inverse Fourier Transformation. Optical system on image 3.13 is formed with two confocal focal lenses $L_1$ and $L_2$. It is called "4f processor" or "4f correlator". The $L_1$ lens is the so-called transformation lens. It makes Fourier transformation of the input image. In the focal plane of both lenses, there is the space spectrum of the input. In this plane, space filtration can be realised using a proper mask. Lens $L_2$ with focal length $f'$ is also producing Fourier transformation. Correctly $L_2$ is

producing double transformation. The $L_2$ lens is called back transformation lens, it makes Fourier transformation of space spectrum back to space domain. Due to double transformation, the output image (wave) $W_3$ is overturned toward original object $W_1$ (3.20). If both lenses have different focal lengths $f \neq f'$, then the size of the original object and its image are proportional to lenses focal length ratio (3.21). [4] [40]

$$\mathcal{F}\{\mathcal{F}\{g(x,y)\}\} = g(-x,-y) \quad \Rightarrow \quad W_3(x,y) = W_1(-x,-y), \tag{3.20}$$

$$W_3(x,y) \quad = \quad W_1(-\frac{f}{f'}x, -\frac{f}{f'}). \tag{3.21}$$

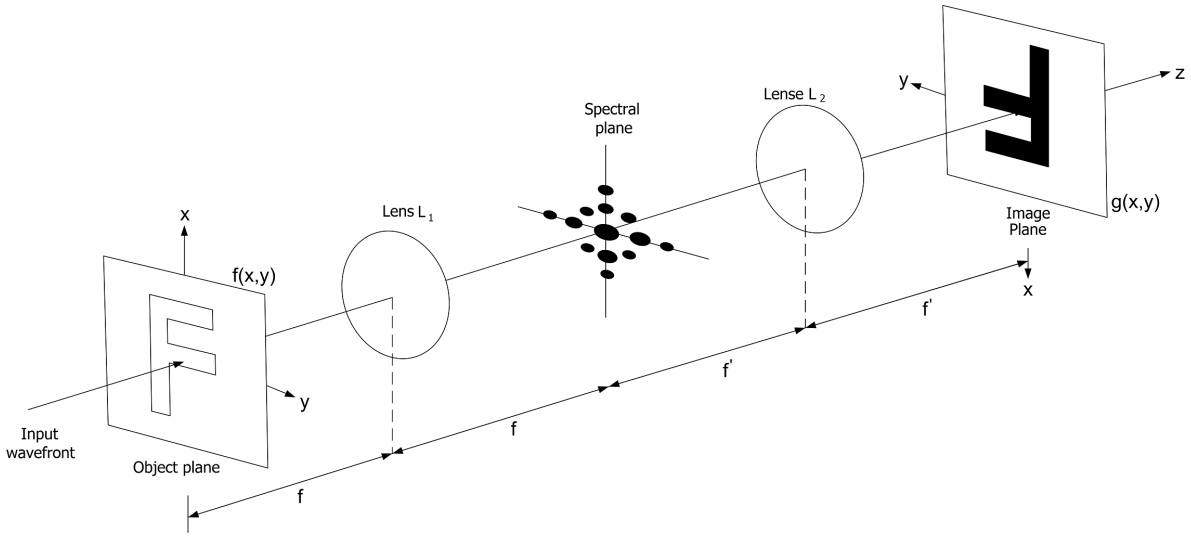


Figure 3.13: System for spatial filtration - the principle of 4-f processor.

### 3.3.2 Demonstration Setup of Optical Fourier Transformation

In this section, the optical demonstration system for OFT is presented in Figure 3.14. This system is used in the next section to demonstrate the process of spatial filtration. It is a 4-f processor, a light source formed with a HeNe laser and a beam expander. Lenses $L_1$ and $L_2$ are transformation and back-transformation lenses. Beam splitter $BS_1$ divides a part of light passing through $L_1$. The beam splitter creates a second spectrum image of the original subject $O$ and allows to save the spectrum with a proper acquisition device. Mask $M$ is located in the common focal plane. Type of filtration caused by mask $M$ is defined via the shape and position of the mask. The lens $L_2$ performs transformation of the filtered spectrum. The output is overturned toward $O$ and is filtered with filter mask $M$. The output is displayed on screen $I$. Beam splitter $BS_2$ provides a second image of the output that is acquired with a camera.

Images shown in next section were acquired on two setups differing in used beam expanders therefore beam diameters and differing in used focal lenses. Setup $S_1$ was based on lenses with focal length

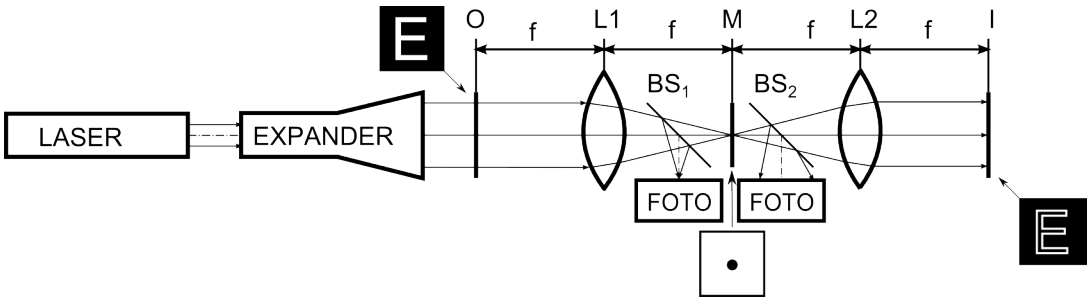


Figure 3.14: Demonstration setup of spatial filtration.

$f = f' = 200$ mm and with the beam diameter 2 cm (after beam expansion). Setup $S_2$ is using beam with the diameter 5 mm and focal lengths of $f = f' = 150$ mm. Images of the spectrum and reconstructed image are acquired with Nikon D5100 cameras. Cameras were equipped with 60mm, 1:2.8 Tamron lens. This lens is also used as a reconstruction lens on the camera used for acquiring the reconstructed image.

### 3.3.3 Demonstration of Filtration Process

Simple geometric shapes and its spectrum and filtered image are presented in this section. Basic space filtrations are presented: low pass filtration (LP), high pass filtration (HP) and directional filtration. Low pass filtration was realized using pinhole with diameter 450 $\mu m$. High pass filters were realized using small aluminium dot with diameter 3 mm and 1 mm. These dots were made from aluminium deposited on a glass plate. The directional filtration was realized with an adjustable slit. When the LP filtration is used, the high spatial frequencies are cut off, and lost of detail precision is expected, vice versa HP filtration cuts off low frequencies and DC part of the image, the output image is expected to be less bright and only edges are shown (high space frequencies represents edges and details). The directional filtration selects only space frequencies in the direction defined by the slit, i.e. vertically set slit selects vertical frequencies which represent horizontal lines and details, it is shown on Figure 3.16f and 3.17c.

The first displayed shape is a grating 3.15a. The spectrum of the grating is in Figure 3.15b. The spectrum is modulated via function $\mathrm{sinc}(x)$ because the grating is formed from a rectangular course of transparency. These images were taken with setup $S_1$ for better clarity. Due to the longer focal length of the transform lens, there is the spectrum more detailed. For a given space frequency $\omega_x$ or $\omega_y$ and two different focal lengths $f_1 < f_2$ applies

$$\omega_x = k\frac{x_1}{f_1} = k\frac{x_2}{f_2} \Rightarrow x_1 < x_2. \tag{3.22}$$

It is apparent that with an increasing focal length increases the distance between space frequencies 3.22.

The same grating is imagined for comparing with setup $S_2$ and all images are shown in Figure

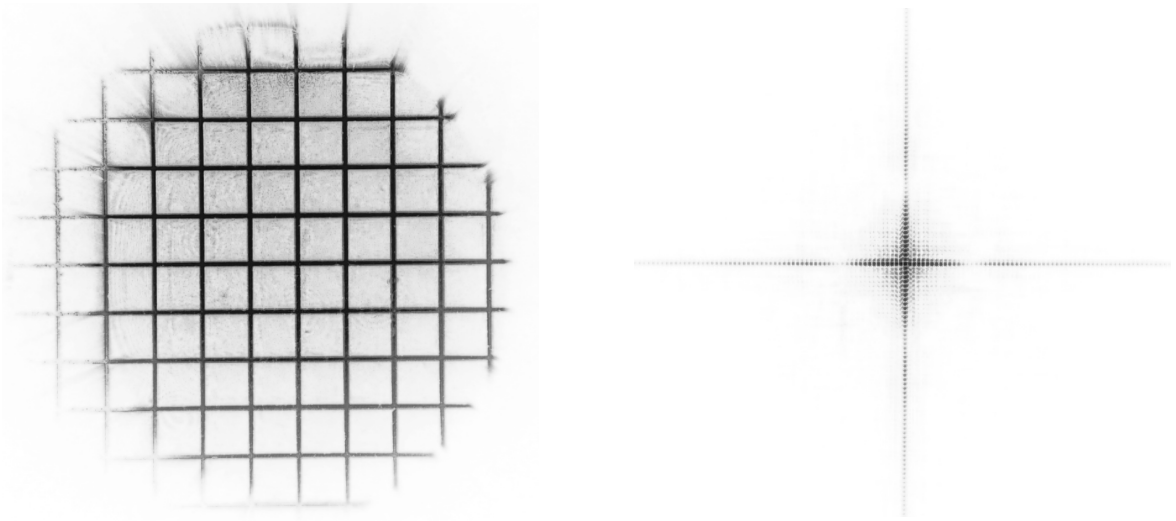

(a) Image of the grating - setup $S_1$

(b) Grating spectrum - setup $S_1$

Figure 3.15: Image of the grating and grating spectrum - setup $S_1$.

3.16a. The spectrum was filtered using the LP 3.16c, the HP -3 mm 3.16d and a directional filter in horizontal 3.16e and vertical 3.16f direction.

Next imaged object is an aperture of shape "E", images are taken with $S_1$ setup.

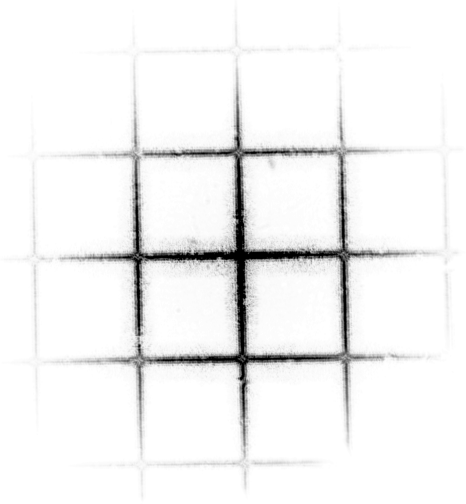

(a) Image of the grating

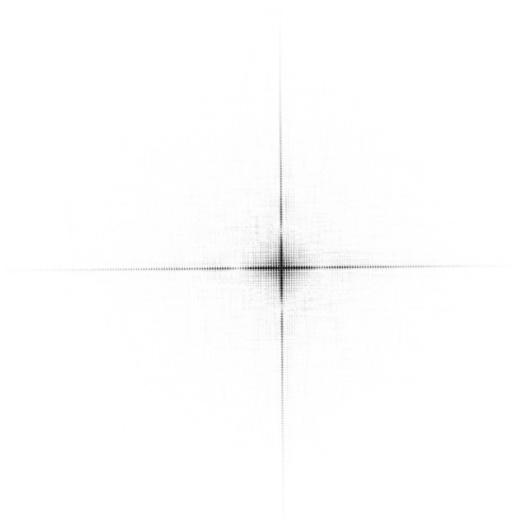

(b) Grating spectrum

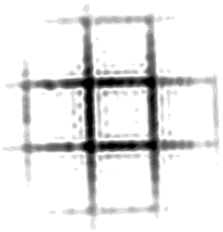

(c) LP grating spectrum filtration.

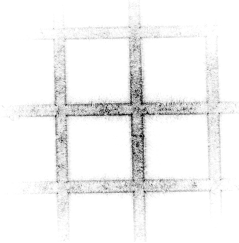

(d) HP grating spectrum filtration - 3mm spot.

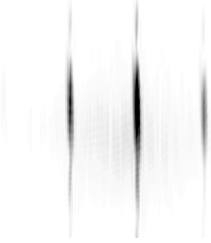

(e) Directional filter in horizontal direction.

(f) Directional filter in vertical direction.

Figure 3.16: Grating image, spectrum and image reconstruction after space filtration - setup $S_2$.

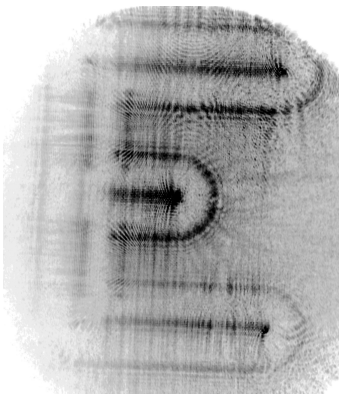

(a) Aperture - letter "E".

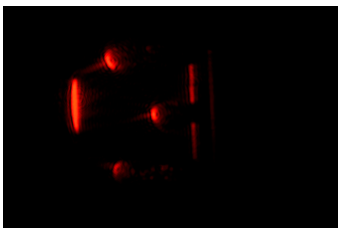

(b) Filtering in horizontal direction.

(c) Filtering in vertical direction.

Figure 3.17: Letter "E" and directional filtering - setup $S_1$.

### 3.3.4 Quality Evaluation of the Crystal with OFT and Spatial Filtration

In the previous sections, the Optical Fourie transformation was introduced and the ability of spatial filtering with OFT setup was demonstrated on basic examples. In this section, three optical setups based on spatial filtration are used with a Calomel sample and its properties are discussed.

#### 3.3.4.1 Spectrum Image

The Calomel sample deforms the wavefront of the passing wavefront (both amplitude and phase). The dimensions of nonuniformities are usually significantly smaller than the sample size and beam diameter, therefore they contribute mostly to the HF spectral components. The photo of the spectrum can be acquired and processed with the computer. Some methods of processing the spectrum are discussed in Section 4.5.

Problem with capturing of the spatial spectrum is a very high dynamic range of the spectrum. The mid part of the spectrum is formed with a DC and LF (Low Frequency) spatial components of the spectrum and high part of the energy is contained here. The way to take a picture of the spectrum is to acquire multiple photos with different exposure times, that is, to create an HDR (High Dynamic Range) picture. Figure 3.18 represents a single image of the spectrum (in SDR - Standard Dynamic Range), an HDR composition and a logarithm view of the HDR.

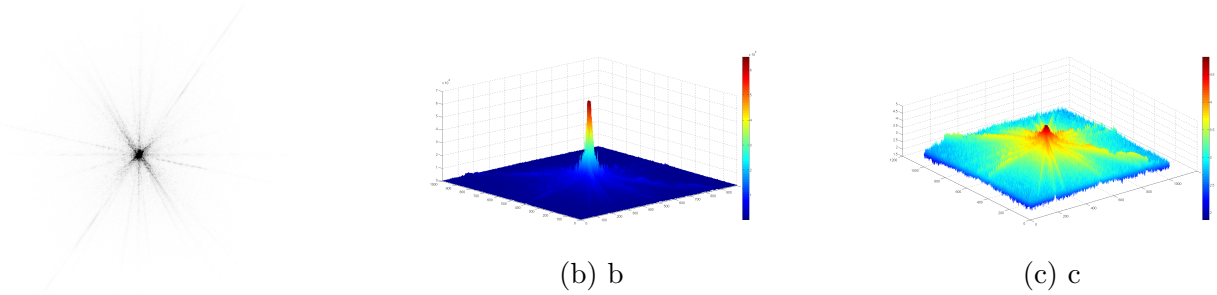

(a) a (b) b (c) c

Figure 3.18: Different representation of the spectrum: (a) SDR image of the spatial spectrum, (b) HDR composition of the spectrum and (c) HDR composition in logarithmic scale.

#### 3.3.4.2 HP Filtered Image

Defects in the material have an influence on higher spatial frequencies. To image these defects the HP spatial filter is used, and a filtered image is captured (Figure 3.19). This method is also a second solution to the previous problem with the high dynamic range of the spectrum - the high energy DC and LF parts are filtered out of the signal and the resulting image is reconstructed and captured.

Figure 3.19: HP spatially filtered image.

#### 3.3.4.3 HP Integral Measurement

This measurement is based on the HP-filtered image, but instead of acquiring the filtered image with a camera and rigorous quantitative evaluation of captured image, only the amount of power of spatially filtered light is measured with a power sensor. The modified setup for HP integral measurement is in Figure 3.20. The form, size and handling of the HP filter will be discussed in Section 4.6.3.

## 3.4 Imaging Properties of the System

There is a wide amount of applications, where the crystal is used for imaging purposes. In this area of interest, the evaluation of the quality can be based on standard properties usually used to describe imaging systems, such as PSF (Point Spread Function) and MTF (Module Transfer Function).

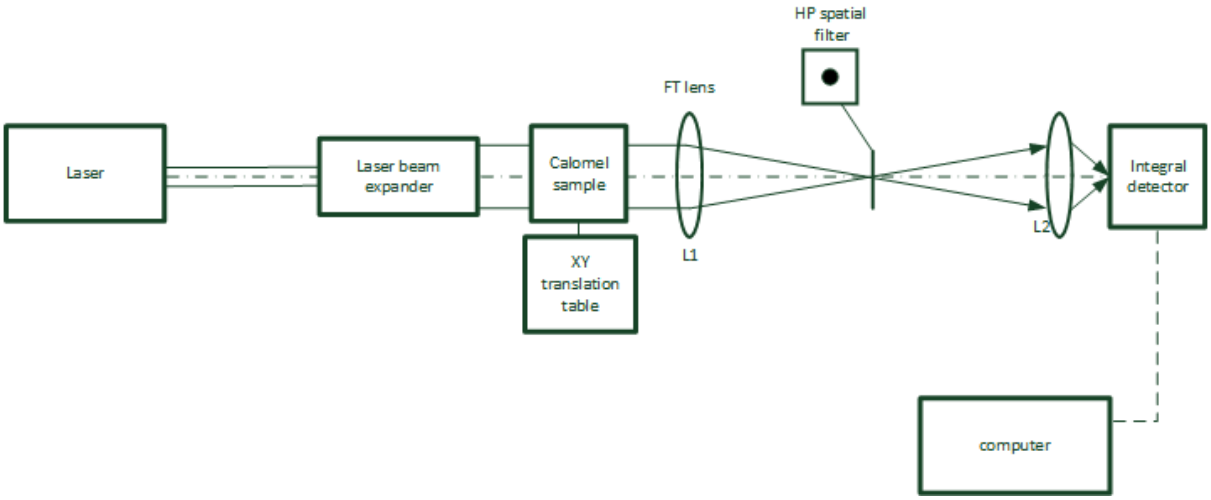


Figure 3.20: Setup for measurement of the power of HP filtered image.

### 3.4.1 Transfer Functions

Let $f(x, y)$ be the input image function. It is affected after passing through the optical element, and the output image function is $g(x, y)$. The input and output of the system are connected via the convolution with a system transfer function $h(x, y)$, in imaging systems called PSF.

$$g(x, y) = f(x, y) \circledast h(x, y). \tag{3.23}$$

Let us assume the linear and shift-invariant system. Then the convolution can be changed with the Fourier transformation

$$\mathcal{F}\{g(x, y)\} = \mathcal{F}\{f(x, y) \circledast h(x, y)\}, \tag{3.24}$$

$$G(\omega_x, \omega_y) = F(\omega_x, \omega_y) \cdot H(\omega_x, \omega_y), \tag{3.25}$$

where $G(\omega_x, \omega_y), F(\omega_x, \omega_y)$ are Fourier transform of the output and input image function with spatial frequency domain $(\omega_x, \omega_y)$. The Fourier transformation of the Point spread of function $H(\omega_x, \omega_y)$ is usually called Optical (or image) Transfer Function - OTF$(\omega_x, \omega_y)$. The OTF is, in general, a complex function with two parts

$$\mathrm{OTF}(\omega_x, \omega_y) = \mathrm{MTF}(\omega_x, \omega_y) \cdot \mathrm{e}^{\imath k \mathrm{PTF}}, \tag{3.26}$$

where MTF$(\omega_x, \omega_y)$ is a Modulation Transfer Function and PTF$(\omega_x, \omega_y)$ is a Phase Transfer Function. The MTF is important for the quality measurement of imaging systems.

There are three possible approaches to measuring the MTF of a tested crystal sample. The first one is based on direct scanning of the PSF. The laser focused beam is used for the realisation of the spatial impulse. A second method is an optical approach. It uses collimated light and an optical slit or edge as a target for optical imaging. The third method has origins in image photonics. The method uses standard test ISO 12233 procedure with a test chart. The last two methods are based

on imagining the test (slit/edge or test chart) through the system with the tested sample inserted in the optical path and without the tested sample. Then the results are compared together.

### 3.4.2 Optical Setup

The setup in Figure 3.21 is based on the third method and uses the tested sample as a filter in the front the camera lens and uses the standard ISO 12233 procedure to evaluate the MTF. The test chart is illuminated with appropriate light sources. There are multiple types of test in the test chart. In this experiment, the calculation the MTF from an ESF (Edge Spread Function) is used. The ESF is a response of the imaging system to the edge source. The MTF in a given direction can be calculated from an LSF (Line Spread Function). The LSF is defined by

$$\mathrm{LSF(x)} = \frac{\mathrm{d}}{\mathrm{d}x}\mathrm{ESF(x)}, \tag{3.27}$$

where $x$ is a variable perpendicular on the slit or edge. The MTF is then calculated

$$\mathrm{MTF}(\omega_x, 0) = |\mathcal{F}(\mathrm{LSF}(x))|. \tag{3.28}$$

With this procedure, the MTF is calculated in one direction. By rotating the reference, the MTF in other directions can be enumerated.

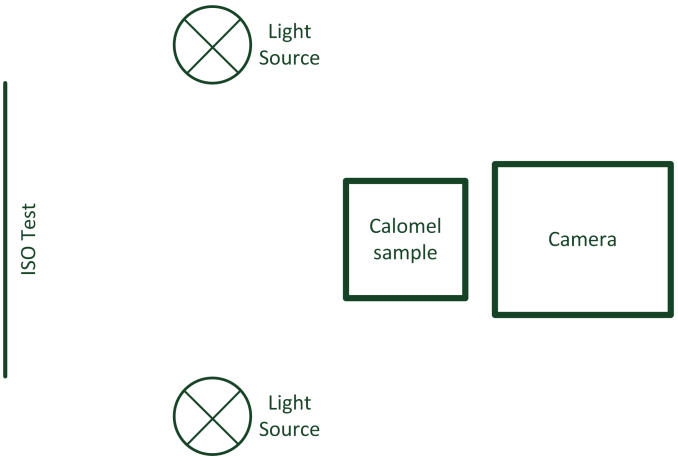


Figure 3.21: The setup for MTF measurement based on the ISO 12233.

### 3.4.3 Experimental Results

Figure 3.22 shows images acquired by the camera without the calomel sample and with two different crystal samples used as a filter. The advantage of this method is robustness and noise reduction. These image tests can be evaluated with standard professional software like IMATEST [41]. Figure 3.23 presents edge profile calculated for all three cases in Figure 3.22. The result MTF chart is

presented in Figure 3.24, Table 3.1 presents values of $MTF_{50}$, these values are usually used to compare the properties of different systems. The value of $MTF_{50}$ is a spatial frequency, where the transfer function decreases to 50 % of the original value.

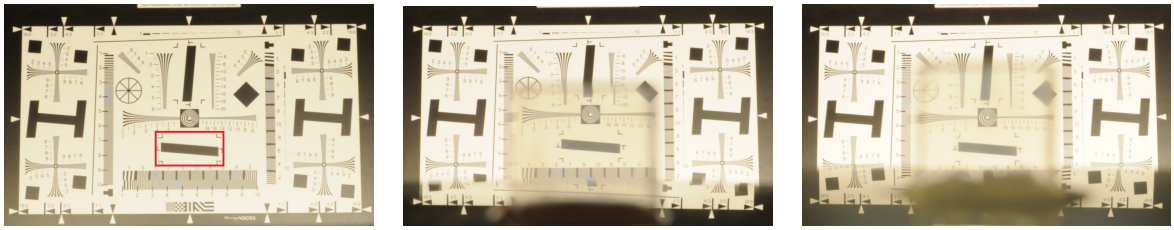

(a) Image with no sample. (b) Sample $T_1$. (c) Sample $T_2$.

Figure 3.22: Images of test chart captured with and without calomel samples. Red rectangle shows part on the ISO test chart used for ESF and MTF evaluation.

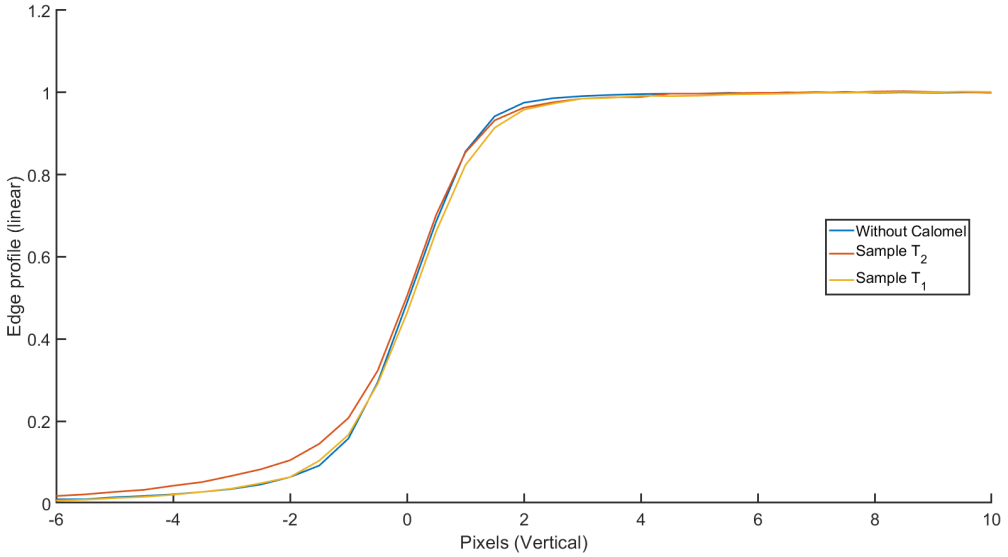


Figure 3.23: Edge profile calculated with IMATEST.

## 3.5 Surface Flatness

This section describes a method to measure the flatness of the tested sample surface. The shape of the surface affects the performance of optical devices. The flatness of the surface is given by the processing technique (polishing). For that reason, a flatness measurement is a useful tool for material production.[7]

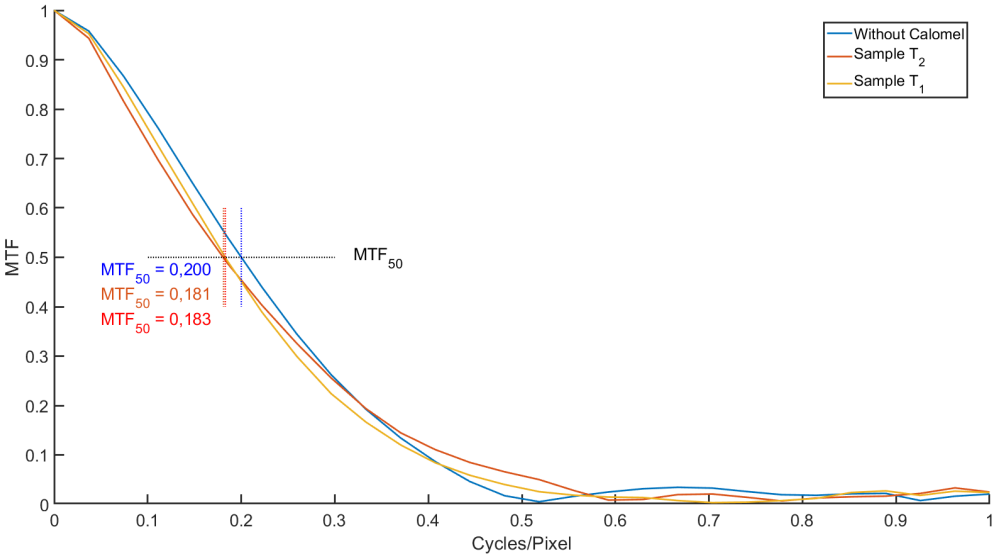


Figure 3.24: MTF of all samples calculated with IMATEST.

### 3.5.1 Optical Setup

The measurement setup is based on well known Fizeau interferometer. It is based on interference of reflected light from the tested surface with light reflected from a known optical flat. The layout of the setup is in Figure 3.25. The laser light (HeNe, 638nm) is spatially filtered with a combination of a microscope lens and a well-positioned pinhole. The filtered light is collimated with a second lens. The high-quality aplanatic lens is used to produce a good quality beam. The flat wavefront goes through the reference flat and reflects from the tested surface. Both reflected wavefronts are diverted from the optical path by the beam splitter. The interference pattern created by reflected wavefronts is imagined with a camera. The reference flat used in the measurement is $\lambda/10$ for 633 nm. The crystal sample is placed on a 2-axis stage - it allows to rotate and tilt the crystal to correct the orientation against the optical flat.

| Configuration | $MTF_{50}$ [cycles/pixel] |
|---|---|
| Without sample | 0.200 |
| Sample $T_1$ | 0.183 |
| Sample $T_2$ | 0.181 |

Table 3.1: Table of $MTF_{50}$

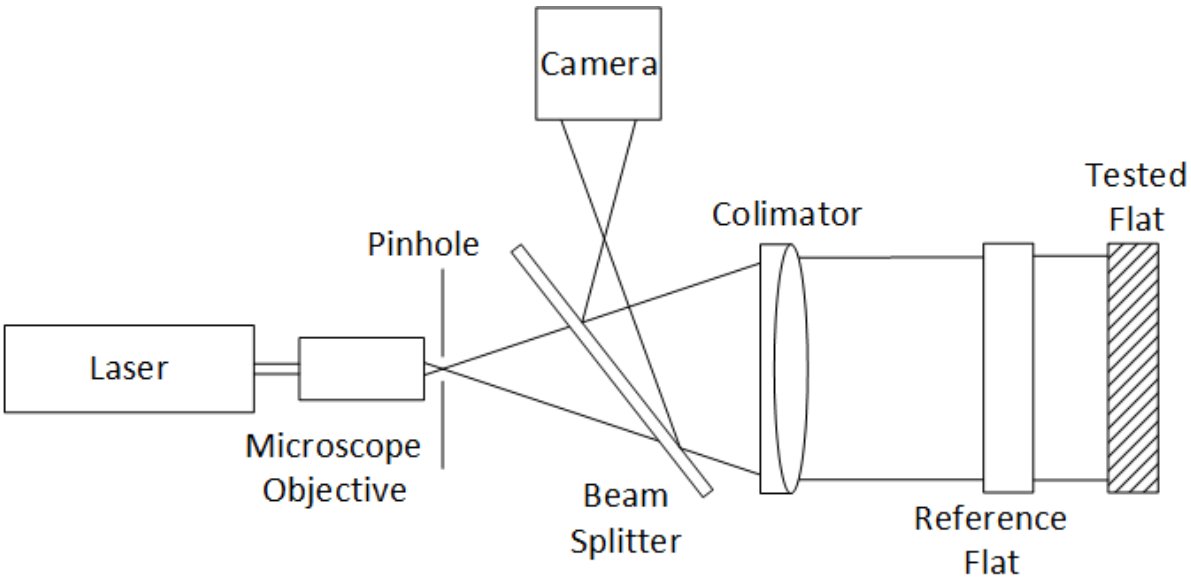


Figure 3.25: Fizeau interferometer used for flatness measurement.[5]

### 3.5.2 Experimental Result

Figure 3.26 illustrates the measurement of the flatness, i.e. flatness error. It shows a reference flat and tested surface with a small wedge. This produces parallel lines in the interferogram. When the tested flat shaped, the lines changed to curves. The flatness of a particular region of the surface is then done by making two parallel lines (Figure 3.26), one between the ends of anyone fringe and the other at the top of that same fringe. The number of fringes located between these lines is used to determine the error of the flatness.

Figure 3.27 presents two different interferograms of different Calomel samples. Figure 3.28 illustrates this evaluation process on the photo of calomel fringes. The used sample shows flatness of the surface containing three fringes, then the error of flatness is $3\times$ the error of flatness of the optical flat, i.e. $3 \cdot \lambda/10, \lambda = 633nm$.

The photo of tested setup is in Figure 3.29.

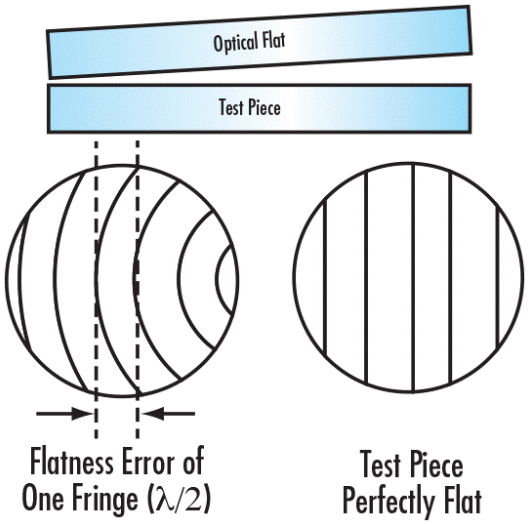


Figure 3.26: Example of the flatness measurement. The number of curves between two straight lines indicates a number of wavelengths, i.e. the flatness error in wavelength.[6]

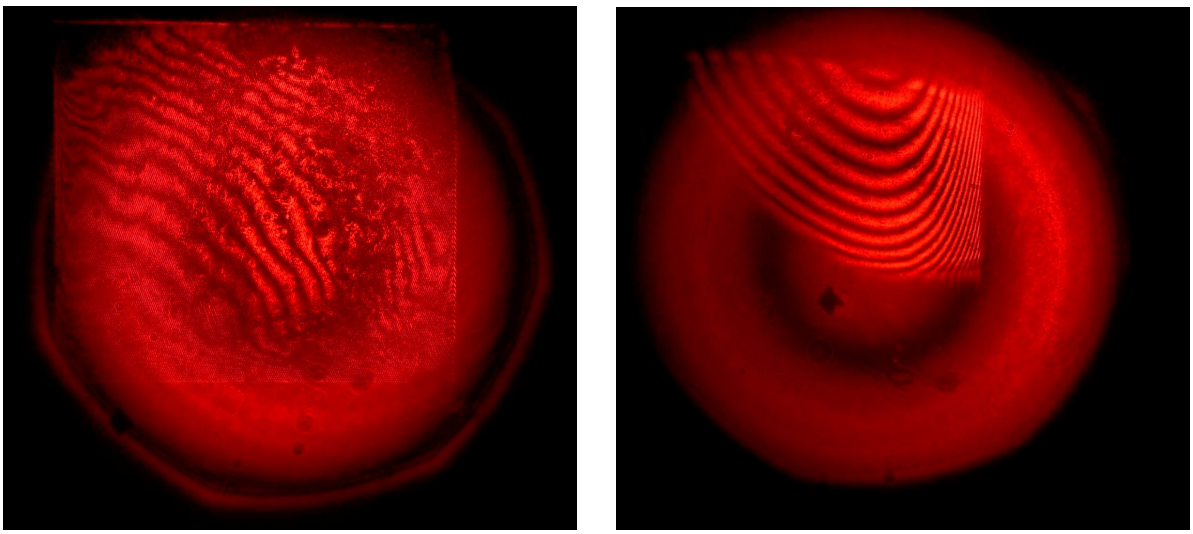

Figure 3.27: Two interferograms of two tested Calomel samples.[7]

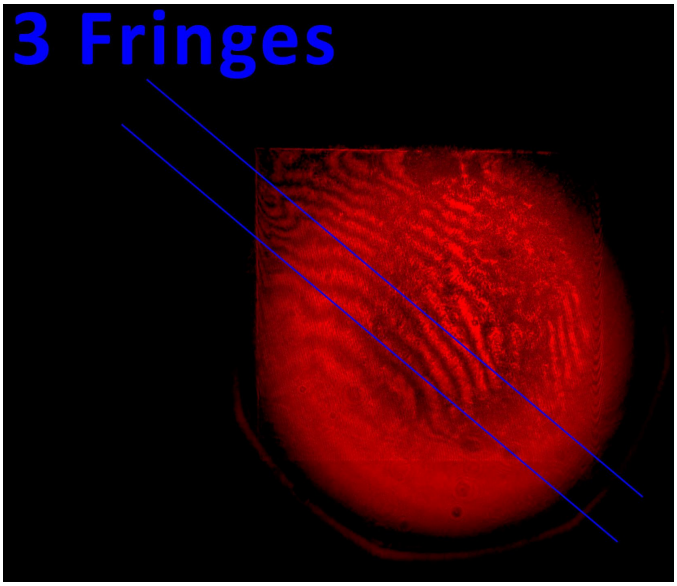


Figure 3.28: Example of fringes measurement with an illustration of a number of fringes.[7]

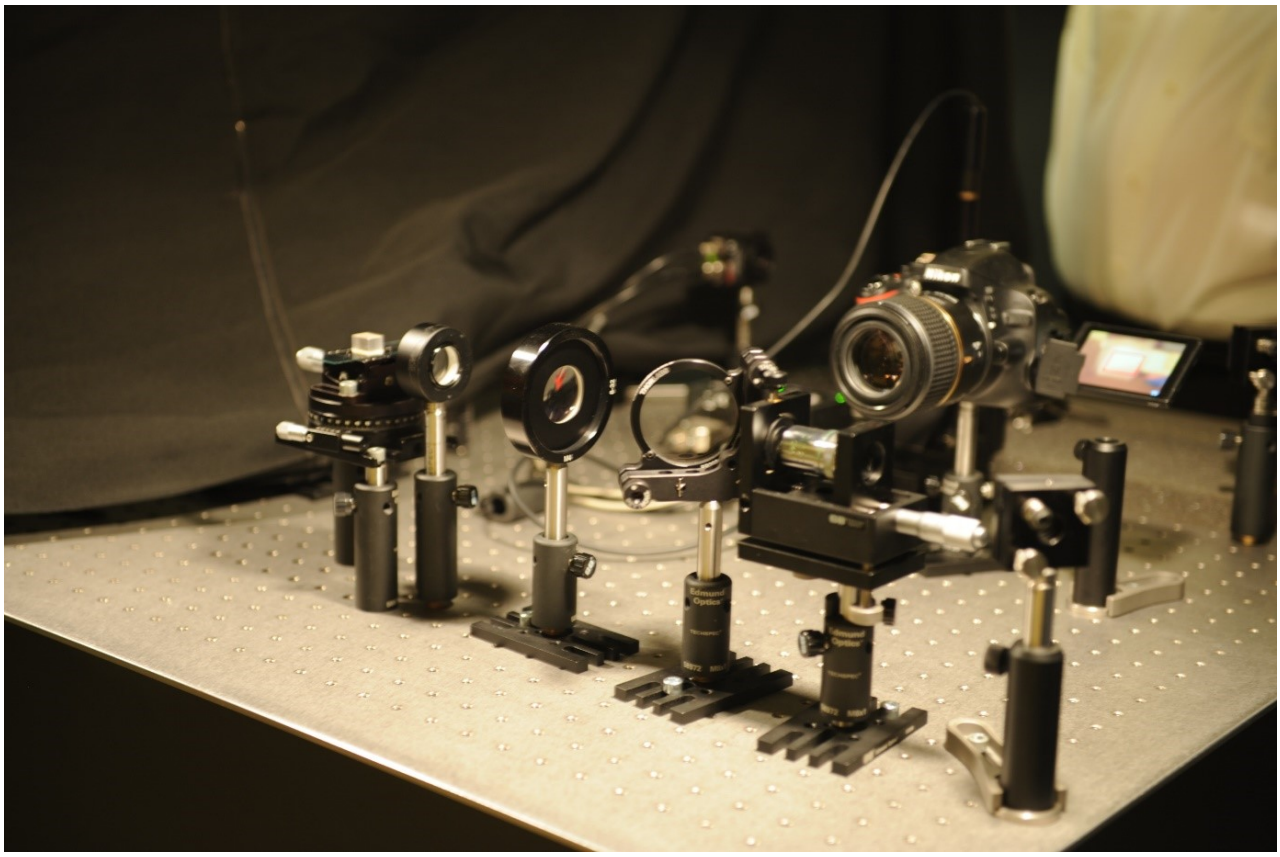

Figure 3.29: Photo of setup for surface flatness measurement.[7]

# 4 Quality Evaluation with OFT

In this section, the complete optical setup for quality evaluation based on OFT is described. This section is focused on a detailed description of the system, on a definition of a quality metric for optical material, properties of the system are discussed and controlling software for the system is also presented. In this section, there is also a description of an advanced method for the evaluation of the spatial spectrum provided by the Optical Fourier transformation.

The calomel crystal cannot be assumed as space invariant system because inhomogeneities are not uniformly distributed in the crystal volume; hence it is necessary to take into account multiple measurements of the crystal in a space distributed points. The crystal is therefore mapped with the laser beam. According to ANSI standard (ANSI IT7.215), it has been used nine points uniformly spread over the active aperture of the sample. This standard relates to the evaluation of homogeneity of displays.

## 4.1 Setup Description

Designed optical setup (Figure 4.1) can be divided into few working blocks. These blocks allow obtaining various information about the light after passing the crystal. Photo of the system is presented in Section 4.9.

### 4.1.1 Light Source

The first part of the setup is a block of the light source. The main part is assembled from a laser power source and a laser beam expander, which produce a collimated beam. A beam splitter BS3 and a Power detector are placed in this source block to monitor an actual power of the laser beam. Photo of the block is in Figure 4.2.

- Laser
  - Thorlabs HNL008L-EC

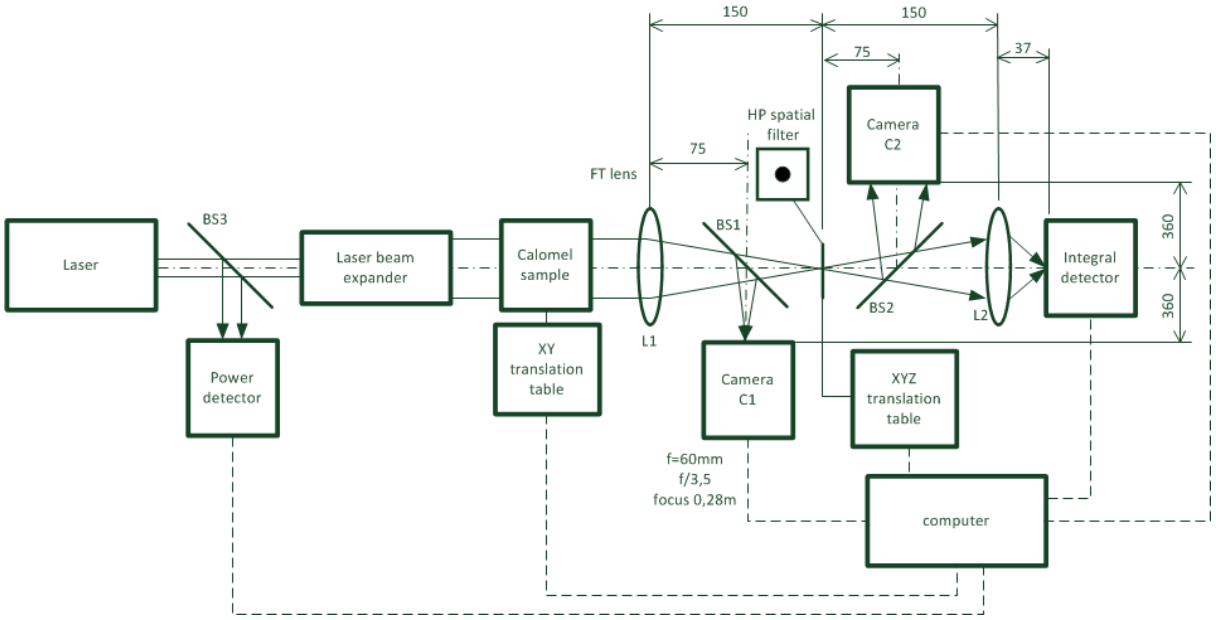


Figure 4.1: The DEMON measuring setup.[8]

  - Wavelength: 632,8 nm
  - Type: HeNe
  - Linearly polarized, ratio 500:1
  - Output power 0.8 mW

- Beam expander
  - Thorlabs BE10M-A
  - Expansion ratio 10x

- Beam splitter
  - Thorlabs BP108
  - Type: Pellicle beam splitter
  - Splitting ratio T:R = 92:8

- Power monitor
  - Thorlabs S120C
  - Si Photodiode, 400-1100 nm
  - Power range 50 nW - 50mW
  - USB interface: Thorlabs PM100USB

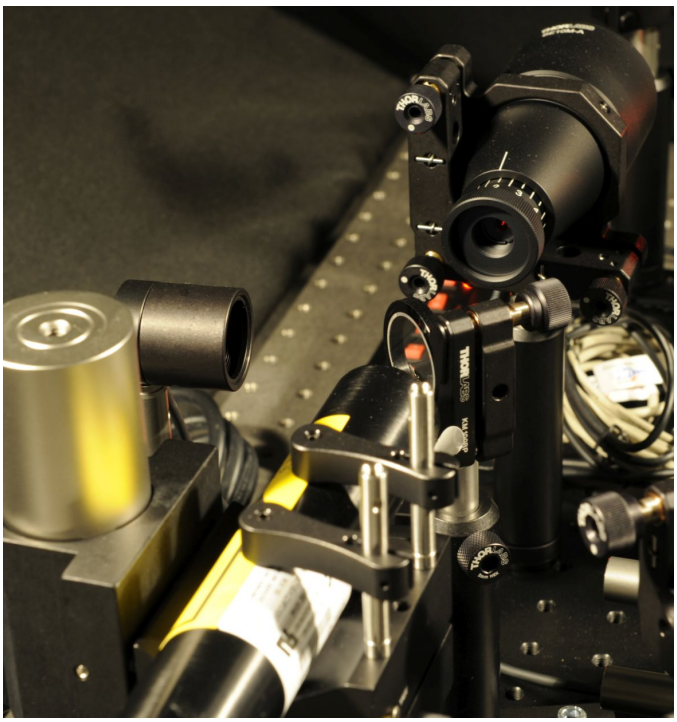

Figure 4.2: Photo of the light source block.[8]

### 4.1.2 Calomel Stage

The second part of the setup is a calomel stage. This block is used to adjust a proper position of the crystal into the laser beam and to move the crystal in the laser beam to scan the crystal. The stage consists of an XY motorised translation stage used to map the crystal and from two manually rotation stages used for tilt and rotation of the sample.

- Translational stage
  - 2x Thorlabs PT1/M-Z8
  - Travel range 25mm
  - 2x USB controller Thorlabs TDC001
- Rotation stage
  - 2x Thorlabs PR01/M

### 4.1.3 Fourier Transforming Lens (FT Lens)

The main part of the complete measuring setup is a lens that realises the OFT. The quality of this element and the influence the quality is the most important to measurement accuracy. Therefore, the element L3 is a high-quality optical lens with corrected geometrical aberrations. This is an

aplanat lens, and it is specially designed for interferometric systems. In the focal plane of this lens, the spatial spectrum of the light passing through the sample is produced.

- Fourier lens
  - Melles Griot LAP - 150.0-30.0-633-PM
  - f = 150 mm
  - Aplanatic lens, corrected for 633 nm
  - Diameter 30 mm

### 4.1.4 Acquisition of the Image of the Fourier Spatial Spectrum

This part is located in space between FT lens L3 and its focal plane and consist from a beam splitter BS1 and a camera C1. The amplitude part of the Fourier spectrum is imaged on the sensor of the CMOS sensor of the camera. The camera is a standard photo camera with an attached macro lens of $f = 60mm$. The camera is focused into the focal plane of the L3 lens created with the beam splitter. Focusing the camera is a part of the calibration process of the setup.

The acquired spatial spectrum has a high dynamic range of power in its spatial components. This implies that the HDR composition is necessary. It is done by acquiring the spectrum with different expositions and merging them with an HDR algorithm.

- Beam splitter
  - Thorlabs BP108
  - Type: Pellicle beam splitter
  - Splitting ratio T:R = 92:8
- Camera
  - Nikon D5100
  - Resolution 4928 x 3264
  - Size of chip 23.6 x 15.7 mm
  - Lens Tamron AF 60mm f/2.0 Macro

### 4.1.5 HP Filtration in the Fourier Spatial Spectrum Domain

A mask realises the filtration of the high spatial frequencies. The mask is a small circle target created from aluminium on optical glass. The spatial filter is mounted on an XYZ translation

motorised stage. The XY direction is used for setting the right position of the mask in the central part of the spectrum (low spatial frequencies and zero-order Fourier coefficient). The Z axis of the stage is used to set the spatial filter into the right Fourier spectral plane, i.e. the back focal plane of lens L3.

- Translational stage
  - 3x Thorlabs PT3/M, 25mm
  - 3x USB controller Thorlabs TDC001

### 4.1.6 Acquisition of the HP-Filtered Image

This part is built the similar way as the part for acquiring the spatial spectrum. It consists from a beam splitter BS2 and a camera C2. The camera macro lens works as a second-transformation lense for the OTF and reconstructs the filtered image onto the CMOS camera chip. The focus of the lens is set up in the calibration process.

- Beam splitter
  - Thorlabs BP108
  - Type: Pellicle beam splitter
  - Splitting ratio T:R = 92:8
- Camera
  - Nikon D5100
  - Resolution 4928 x 3264
  - Size of chip 23.6 x 15.7 mm
  - Lens Tamron AF 60mm f/2.0 Macro

### 4.1.7 HP Power of High Spatial Frequencies

The last optical part of the setup is used to measure the amount of light power in high order spatial frequencies of the OFT. The value has a relation to the number of inhomogeneities in the crystal, i.e. to the deformation of the optical wavefront by the calomel crystal. The power of the light is measured with an Integral detector and with a lens L2, which focuses the filtered light into the detector.

- Integral detector

  - Thorlabs S140C
  - Si Photodiode, 350 - 100 nm, integrating sphere
  - Power range 1$\mu$W - 500 mW
  - USB interface: Thorlabs PM100USB
- Focusing lens
  - Thorlabs LB1757-A
  - Bi-Convex Lens, f = 30.0 mm

### 4.1.8 Setup Control

Last part of the setup is a software control part, which consists of a PC with connected translational stages for the calomel sample and the filter stage, connected cameras and the Power and Integral detector. The controlling system is described in Section 4.6.

## 4.2 Index of Quality - ICQ

The power of high spatial frequencies looks promising as a simple and precise metric, that can be used to evaluate the quality of the crystal and to describe it with a single number or with a map of numbers when the crystal is mapped with the laser beam. There are two difficulties using only the directly measured HP power; the first is fluctuating power of the laser. We also have to take into consideration the fact, that even without the sample, the optical system has its imperfections. For that reason, the different metric has been created - ICQ (Index of Calomel Quality). Let us measure of the HP power without the tested sample and with a proper set of the HP filter. The HP power measured with the Integral detector is $P_{HP0}$, the actual power of the laser is $P_{Las0}$. We can mark their fraction as $ICQ_0$

$$ICQ_0 = \frac{P_{HP0}}{P_{Las0}}. \tag{4.1}$$

Now, we can measure the HP with proper setup tested crystal in the laser path and the HP power and power of the laser are $P_{HP1}$, resp. $P_{Las1}$. We can mark their fraction as $ICQ_1$. The final ICQ of the sample in a given point is then defined.

$$ICQ = \frac{ICQ_1}{ICQ_0}, \tag{4.2}$$

$$ICQ = \frac{P_{HP1}}{P_{HP0}} \cdot \frac{P_{Las0}}{P_{Las1}}. \tag{4.3}$$

As mentioned above, the crystal is a space-variant system, and thus the quality is measured in many points. Measuring points are spatially distributed into a grid, usually in 3x3 points. With this grid, the quality map can be shown as a map of ICQ distribution (Figure 4.3). Using this map can be concluded about inhomogeneities distribution within the sample, and different samples can be compared. For a comparison of a sample quality to some global scale, the scale must be set first. Although the value of the ICQ is physically exact, the global scale is a bit more empiric. This scale is going to be determined after measuring many samples and comparing results to another quality test.

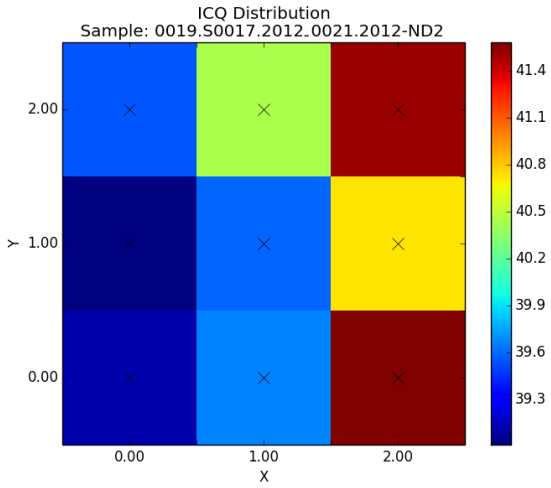


Figure 4.3: ICQ quality map - sample S17

## 4.3 Repeatability

In this section, the repeatability of the measurement in the setup is discussed. This test is done to verify the stability of the optical quality evaluation setup. The quality of the selected sample has been ten times measured with the procedure by the setup in nine points distributed in a spatial grid according to previous sections. Between each quality evaluation, the crystal sample has been removed from the setup and installed again and all functional units (power detectors, translational stages) have been reset. The result of the repeatability test is summarised in Table 4.1. Distribution of ICQ in the crystal sample is shown in Figure 4.4. The variation of the ICQ is smaller than 1 %. This test has verified the stability of the measurement setup.[9]

| **Point** | **M. 1** | **M. 2** | **M. 3** | **M. 4** | **M. 5** | **M. 6** | **M. 7** | **M. 8** | **M. 9** | **M. 10** | **ICQ** | $\sigma_{ICQ}[-]$ | $\sigma_{ICQ}[\%]$ |
|---|---|---|---|---|---|---|---|---|---|---|---|---|---|
| X0 Y0 | 83.2 | 82.9 | 81.2 | 82.2 | 81.7 | 81.8 | 81.1 | 81.4 | 83.2 | 82.3 | 82.1 | 0.57 | 0.694 |
| X1 Y0 | 85.7 | 85.3 | 83.7 | 84.6 | 84.1 | 84 | 83.5 | 83.9 | 85.7 | 84.8 | 84.5 | 0.61 | 0.722 |
| X2 Y0 | 86.9 | 86 | 84.4 | 85.1 | 84.8 | 84.6 | 84.1 | 84.6 | 86.1 | 85.4 | 85.2 | 0.707 | 0.83 |
| X0 Y1 | 81.5 | 81.2 | 79.8 | 80.9 | 80.2 | 80.2 | 79.6 | 80.1 | 81.5 | 80.9 | 80.6 | 0.451 | 0.56 |
| X1 Y1 | 84.7 | 84.7 | 83.4 | 84.4 | 83.7 | 83.7 | 83.1 | 83.5 | 85 | 84.4 | 84.1 | 0.389 | 0.463 |
| X2 Y1 | 88.6 | 88.7 | 87.3 | 88.1 | 87.6 | 87.5 | 86.8 | 87.5 | 88.8 | 87.9 | 87.9 | 0.397 | 0.451 |
| X0 Y2 | 78.1 | 78 | 76.8 | 77.7 | 77.1 | 77.2 | 76.5 | 77 | 78.2 | 77.6 | 77.4 | 0.312 | 0.403 |
| X1 Y2 | 81.7 | 82.3 | 81 | 82.2 | 81.5 | 81.4 | 80.6 | 81.4 | 82.7 | 81.8 | 81.6 | 0.344 | 0.422 |
| X2 Y2 | 89 | 90.3 | 88.8 | 89.8 | 89.2 | 88.8 | 88.2 | 89 | 90.7 | 89.5 | 89.3 | 0.498 | 0.557 |

Table 4.1: Repeteability test - measured ICQ values.

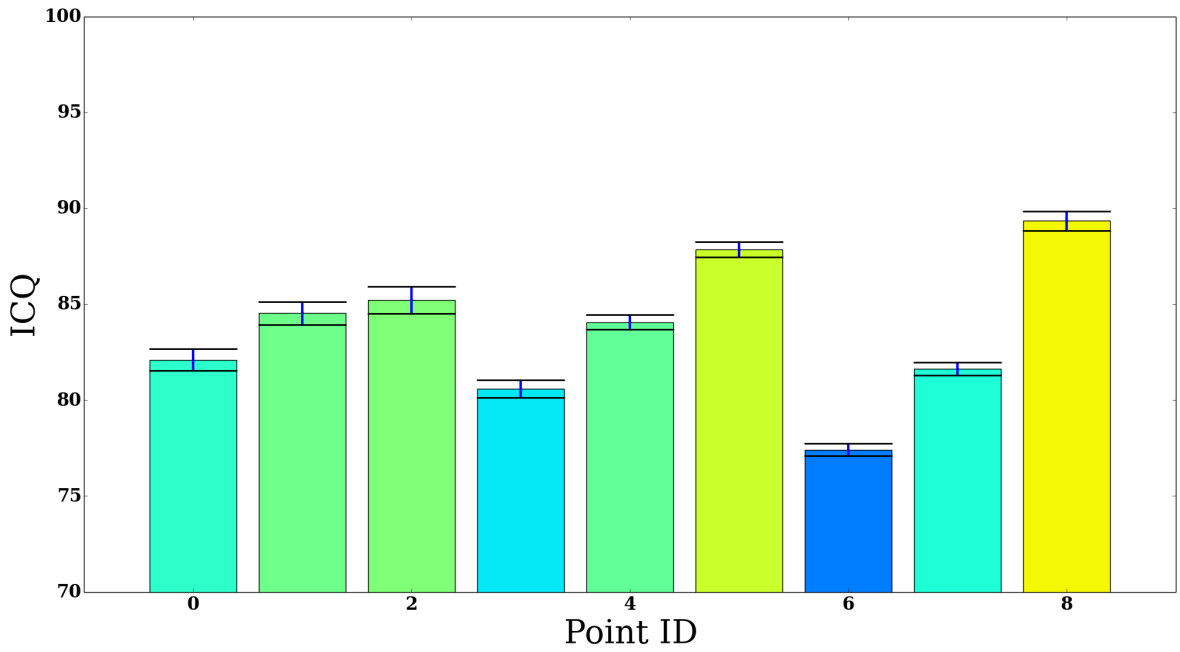


Figure 4.4: Mean value of ICQ in repeatability test and error value.[9]

## 4.4 Size of the HP Filter

In this section, the selection of HP filter diameter is discussed. We have tested a sample of circular HP filters with diameters 0.5 to 2.0 mm. For every filter diameter, the quality test was done, the ICQ was measured in 9 points. Test results are presented in Figures 4.5 and 4.6. It is a relation between HP filter diameter, i.e. spatial frequencies to be filtered and the amount of HP power passed through the filter. Too small filter size leads to high sensitivity to the noise and the precision of the filter position. Big diameter decreases sensitivity to imperfections in the material, which is important to the application. The size of the HP filter is chosen to be 1 mm.

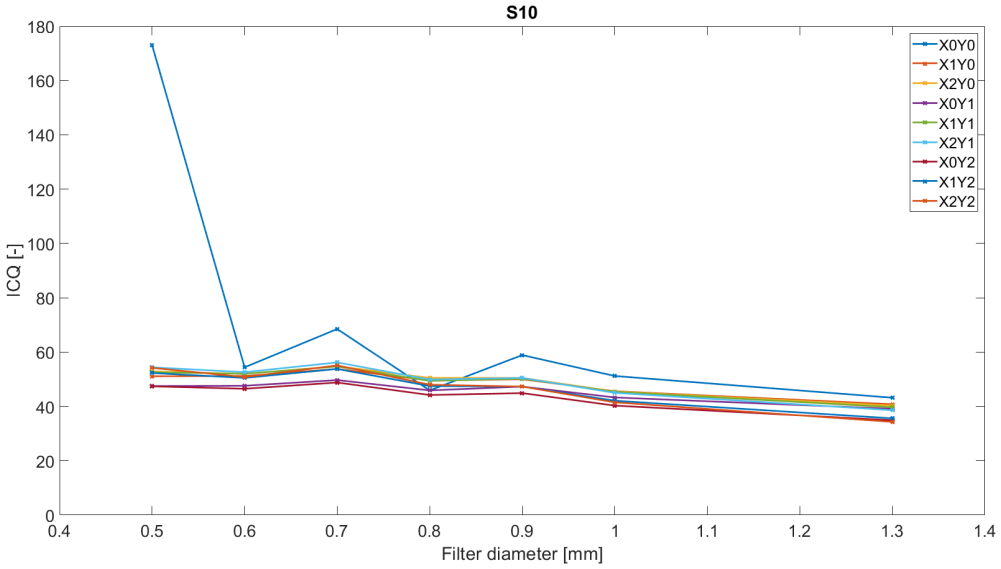


Figure 4.5: ICQ depending on filter diameter, sample S10.[9]

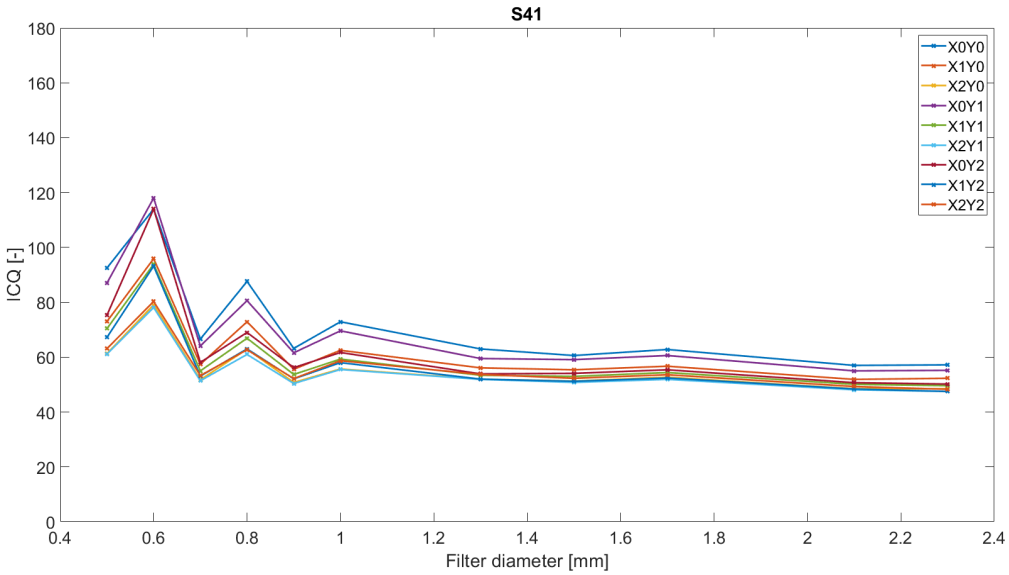


Figure 4.6: ICQ depending on filter diameter, sample S41.[9]

## 4.5 Spectral Sectorization

There are several analytical methods developed to be applied to data acquired by the HDR imaging of the spatial spectrum. They are described in this section. The first method is a sectorial analysis and the second method is a radial analysis. The third method is a combination of both previous methods.

The first step for all analysis is masking the central part of the FT spectrum. The masked part was set by the FWHM (Full-Width at Half Maximum) criterion. The mask diameter was selected as the FWHM value of the DC component value. This leads to reducing the dynamic range of the spectrum and also prevents possible saturation effects in the central part of the spatial spectrum. The second step in the analysis was an interpolation from rectangular scanning raster (provided by the camera chip) to uniform polar scanning raster. The centre of the polar coordinates was calculated as a centre of the mass of the saturated (or highest value) pixels in the image of the spectrum. The analysed picture was also limited by the maximum radius $r_{max}$, defined as the position of the most distant pixel with a value above 1% of the maximum energy value. As a next step, the spatial integration over predefined segments is applied, the size and shape of the segment differ with the used method. The side effect of the integration over the segment is raising the SNR.

The first technique is a directional sectorial analysis. It uses rotating sectors with a given angle for segment energy integration. The result is an angular dependence of integrated energy (Figure 4.7). It demonstrates the angular energy distribution over the complete 360° circle. Segments have been set to 1° wide. There is a strong angular dependence of scattering that correlates to the tetragonal symmetry of the calomel. The energy maximums are approx. at 45, 135, 225 and 315 degrees, that corresponds with the positions of crystallographic axes of the calomel [100] and [010]. [10]

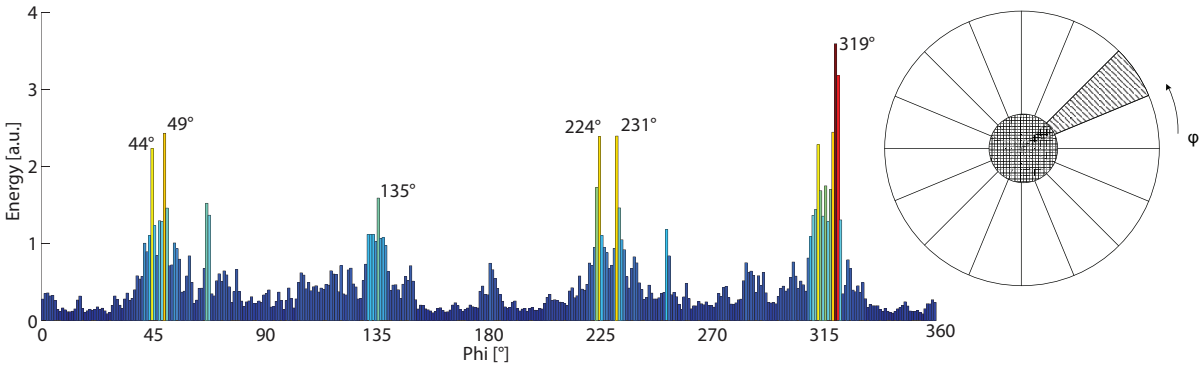


Figure 4.7: Sectorial analysis.[10]

The second technique, the radial analysis, uses segmentation over the complete circle, but the energy is calculated in circular rings. The size of every ring is set to be equiareal, i.e. the width of the ring is decreasing with increasing radius of the circle (Figure 4.8). This analysis provides the initial information about the dimensions of possible scattering centres.

The third method is a combination of previous methods. It is a sectorial-radial analysis. The output of the analysis looks similar to the original FT image but can be used to show the distribution

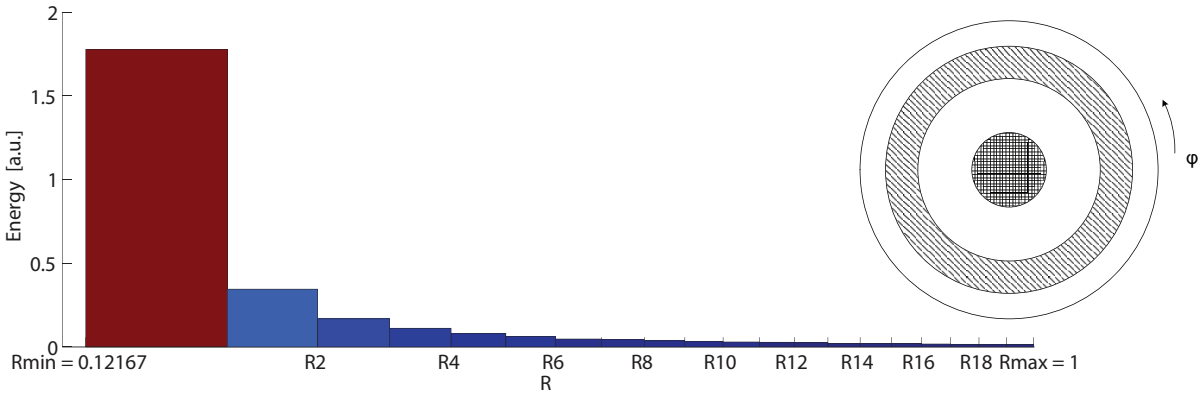


Figure 4.8: Radial analysis.[10]

of the energy. The integration over a region (the annulus sector) improves SNR ratio, eliminates sharp peaks and averages the energy total. Figure 4.9 demonstrates the result of the combined sectorial-radial analysis of a smoothed version of the original spectrum.

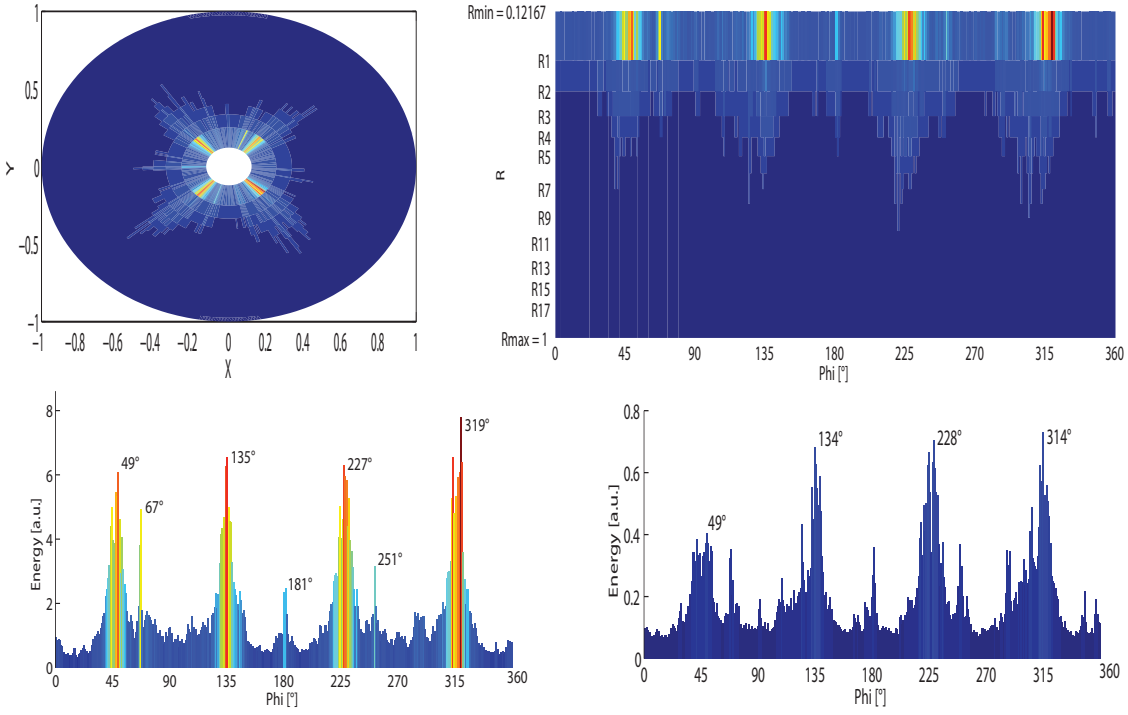


Figure 4.9: Combined sectorial-radial analysis.[10]

## 4.6 Control Software

In this section, the software developed for the optical setup is described. The software is designed to control and drive the measurement and provides all necessary calculations to provide a quality report of the tested crystal sample. The software is developed in Python (version 2.7) as it is a

widely spread language used for computing in science. The software is divided into multiple parts (described below) and provides all necessary functions to calibrate the optical setup itself and to calibrate and control all equipment.[11]

### 4.6.1 Hardware Setup

The software is designed to work with equipment described in Section 4.1. The first step in the software is to connect and test all devices, i.e. translation stages, power meters and cameras. To identify each device, their serial numbers are used. After establishing the connection to translational stages, they are set to go to the zero (home) position (Figure 4.10).[11]

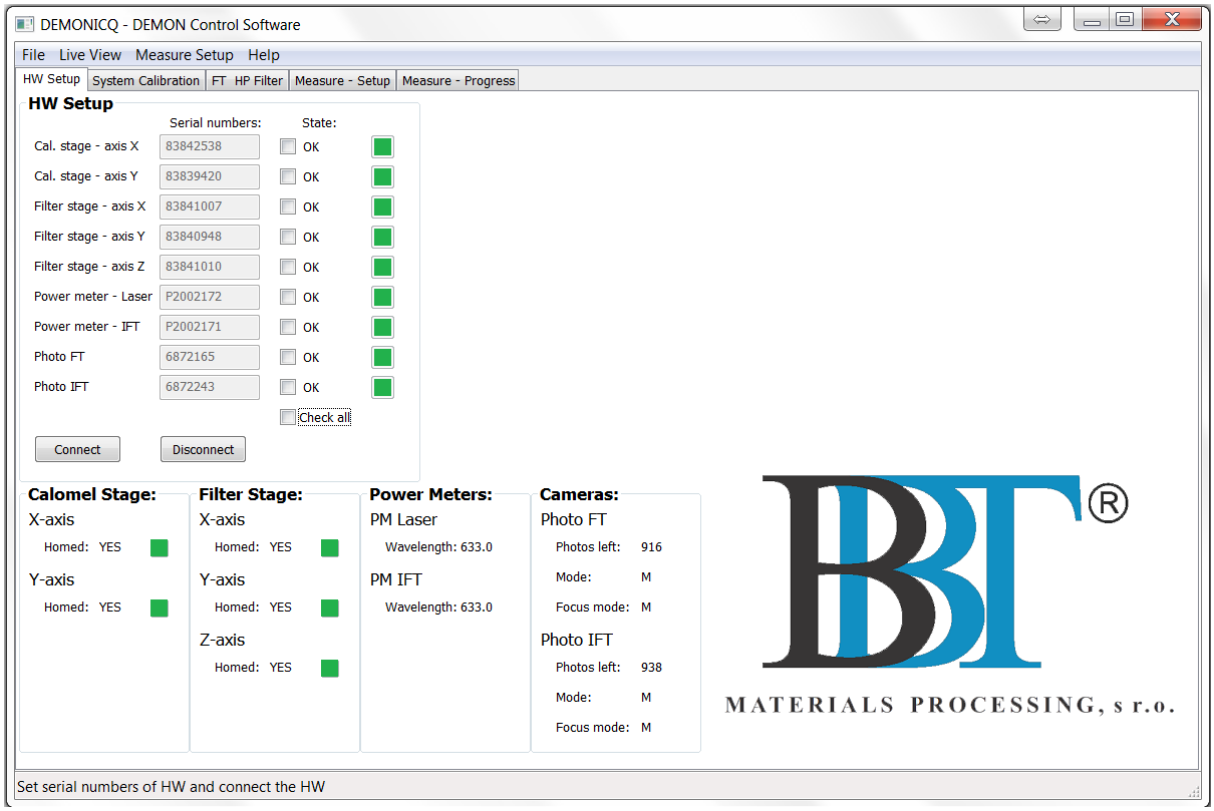


Figure 4.10: Setup of the hardware equipment used and basic hardware informations.[11]

### 4.6.2 System Calibration

This part is used to calibrate the system itself when adjusting the optics. It is also used for an operating calibration, to set the zero power (dark current) of both laser power meter and the power detector. First, the user closes the detector with a closing lid and then set the detectors zero power (Figure 4.11).[11]

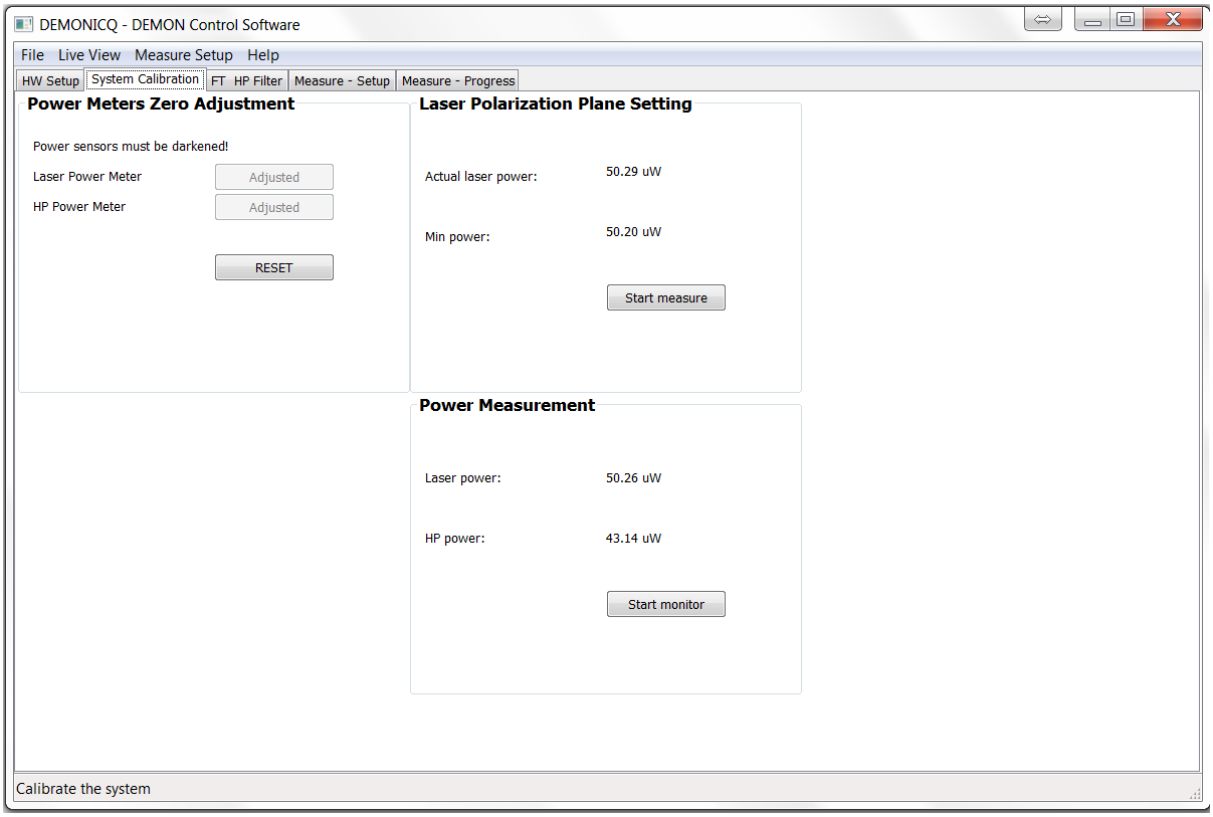


Figure 4.11: System calibration.[11]

### 4.6.3 HP Filter

Next section is used to set the position of the HP spatial filter to the central part of the spatial spectrum. The first step is done by the user manually, he sets the approximate position of the filter manually or reloads the position previously saved. Then, the filter position is automatically set via the scanning of the filter through the XYZ space in a small volume and measuring the actual ICQ. The correct position is the one with the smallest ICQ. This position is saved, and the value of ICQ is set as $ICQ_0$. This setup is done without the crystal sample (Figure 4.12).[11]

### 4.6.4 Measure Setup

In this part of the software, the user can set parameters of the measurement:

- set the ISO, time and number of different expositions taken with cameras for HDR imaging,
- select the type of acquired data (spectrum images, HP filtered images and ICQ measuring),
- the measuring grid, its number of points used and the size of the step between points,
- set the tested sample in the first position of the scanning grid,

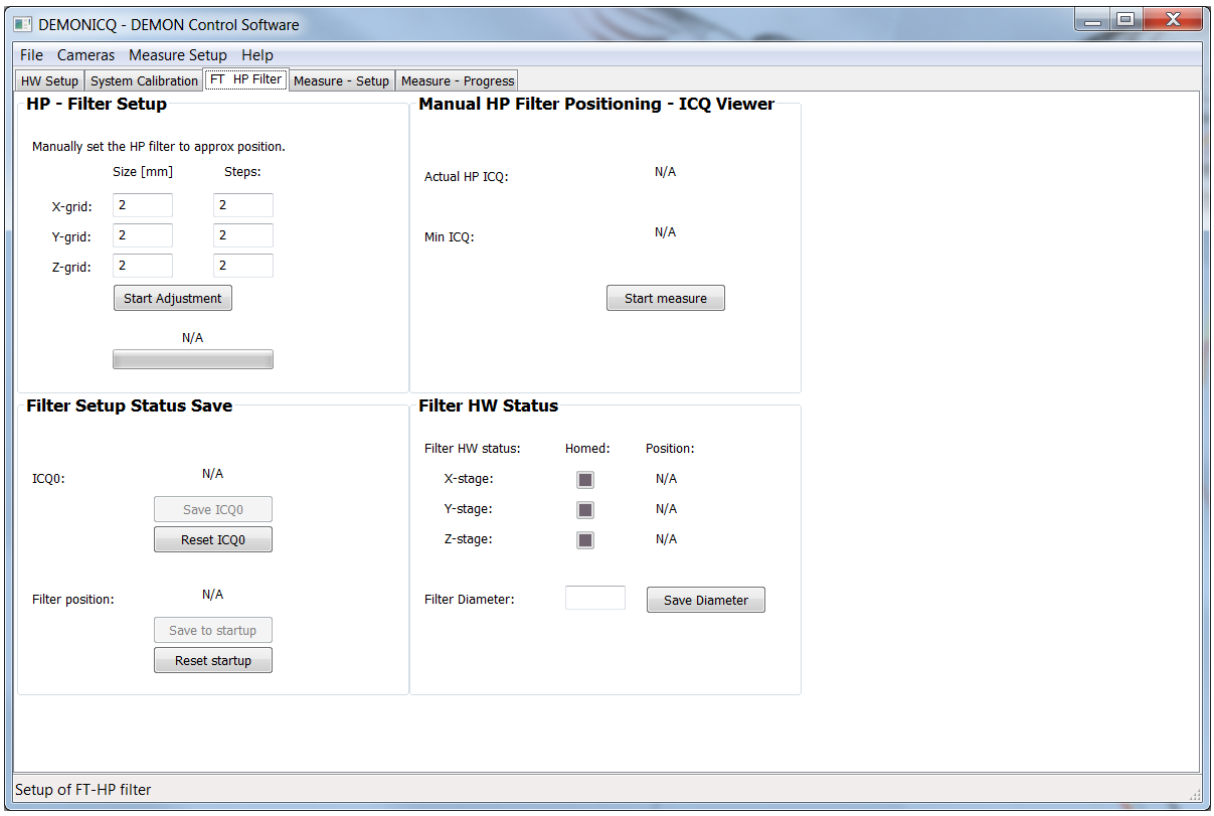


Figure 4.12: Setup of the HP filter. Automaticaly set the accurate position and save $ICQ_0$.[11]

- provide information about the tested sample,
- set the folder for output all measured data and reports.

When the setup is done, the system prepares each step of the measuring process (Figure 4.13).[11]

### 4.6.5 Measuring Process

The measuring section of the software goes through all steps prepared by the measurement setup. That means, to scan the tested sample through the grid, to take every planned measurement, to control expositions of cameras, to measure the power of the laser and HP laser power. After finishing acquiring the data, the process continues with data downloading and processing, i.e. downloading images from cameras and merging them with the HDR process, calculating the ICQ in every point and creating the ICQ map. When all data are collected, the software prepares all data for the measurement report, creates the report and move all data to the user-selected location. The output of the process is a report of the measurement in PDF format including all information about the sample, ICQ map with all values and maps with FT spectrum images and HP filtered images in all measured points. A supplement to the PDF report is a machine-readable report in XML format with all measured data and all source images. This can be later used for additional

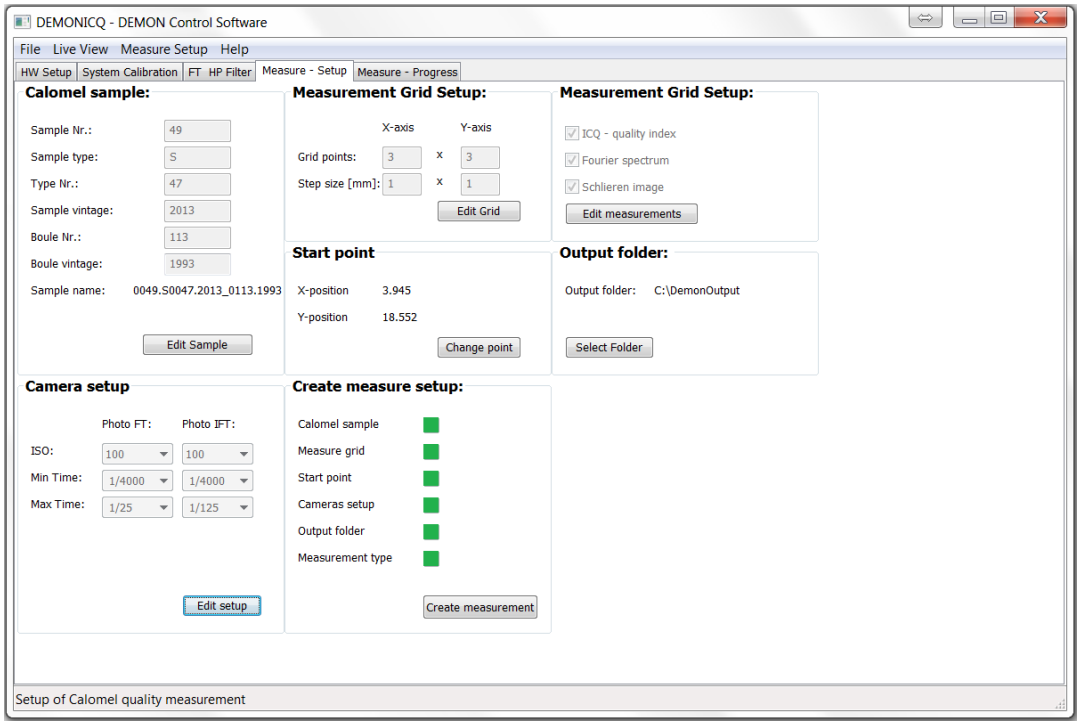


Figure 4.13: Measuring setup, all parameters are set and ready to start measurement.[11]

data mining. Figure 4.14 shows the measurement procedure window with user information and Figure 4.15 shows the measurement procedure schematically.[11]

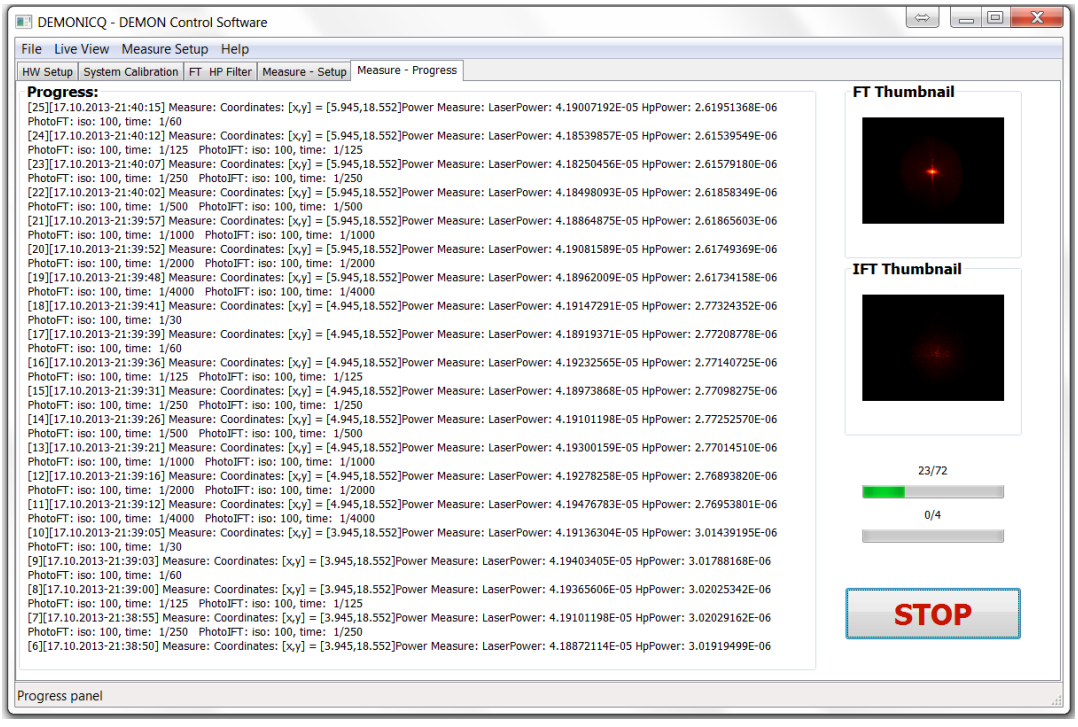


Figure 4.14: Measuring process. The system provides information about actual measured step to the user.[11]

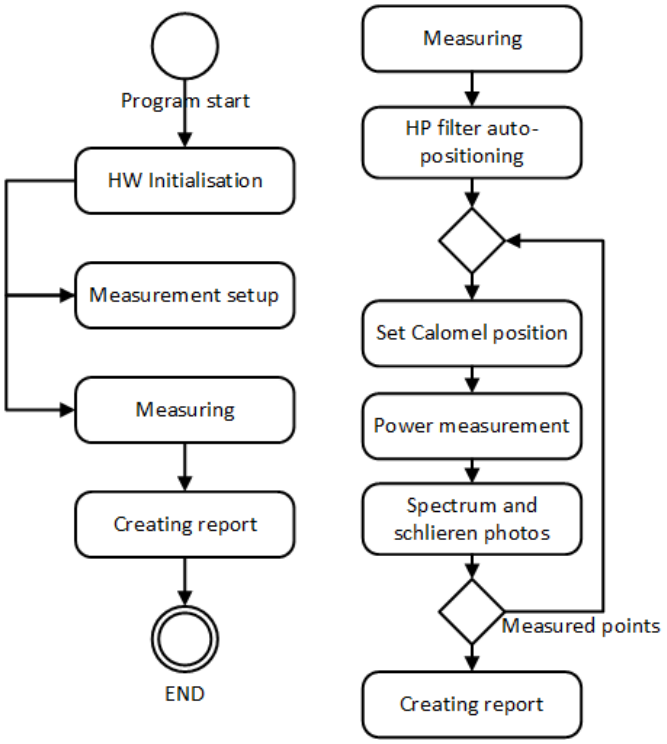


Figure 4.15: Schema of the measuring process.[11]

## 4.7 HDR Processing

In previous sections, there is mentioned, that the 2D FT spectrum image has an extremely high dynamic range. It is estimated as high of 9 or 10 orders. In this section, the used method of HDR is described. Used cameras are not able to record such high dynamic range. The exposure bracketing is used to overcome this limitation. This technique records the FT image of the spectrum with different exposure times sequentially. Also, pictures have to be saved with loss-less compression to eliminate possible compression artefacts and losing the precision of the image.

Let us have a set of images $u_i, i = 1..M$, where $i$ is the index of the image and $M$ is the number of acquired images. Each image is obtained with exposure time $T_i$. The number of images $M$ is selected concerning minimum and maximum values in the picture. The shortest exposure time is as short as possible, to avoid saturation in the DC and LF components of the 2D FT image. Let us define the range of intensity values as $< 0, 1 >$ and a range, where used digital camera has a linear sensitivity curve [42] $< A, B >$. Levels in an image can be expressed as

$$u_i(x, y) = \frac{\pi\tau\gamma}{4} L(x, y) \left(\frac{D}{f}\right)^2 T_i \cos^4\theta, \tag{4.4}$$

where $L(x, y)$ is an intensity profile function in a subject scene (the FT spectrum), $D$ is a lens aperture, and $f$ is a focal length. Then the fraction $f/D$ is an F-number, $\tau$ is lens transparency,

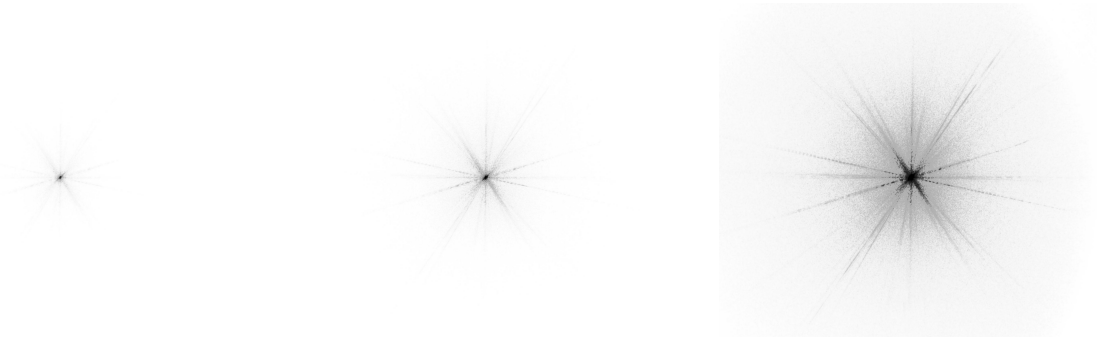

(a) 1/4000 s (b) 1/500 s (c) 1/15s

Figure 4.16: Real FT spectrum of a tested sample for three different exposures. The grayscale is inverted.

and *phi* is an angle in a field of view. This value respects the influence of inhomogeneity of sensor irradiation and sensitivity profile (i.e. flat field). The parameter $\gamma$ is a slope of camera sensitivity curve. The most critical parameter is the exposure time $T_i$.[10]

The pixel on position $x, y$ is underexposed when its value $u_i(x, y) < A$ and similar, the pixel is overexposed when the value $u_i(x, y) > B$. Over- and underexposed pixels are excluded from HDR calculation. To sum contributions from all images in the sequence, we have to convert all levels to values without the influence of exposure time. The pixel levels are converted by

$$\overline{u_i(x, y)} = u_i(x, y)\frac{T_0(x, y)}{T_i(x, y)}. \tag{4.5}$$

Levels in HDR image are then calculated as a mean value of $\overline{u_i(x, y)}$ over a set of images with the level in the $< A, B >$ range,

$$u_{HDR}(x, y) = \frac{1}{N_{HDR}} \sum_{i=1}^{N} \begin{cases} \overline{u_i(x, y)} & \text{if } A \leq u_i(x, y) \leq B \\ 0 & \text{otherwise.} \end{cases} \tag{4.6}$$

where $N_{HDR}$ is a number of images with $A \leq u_i(x, y) \leq B$. Figure 4.16 shows three images of the FT spectrum of a tested sample for three different exposures 1/4000 s, 1/500 s, 1/15 s. Figure 4.17 then presents the final HDR image.

## 4.8 System Outputs

As mentioned in Section 4.6.5, the automated measuring system provides multiple kinds of outputs. The main output is the quality map of ICQ (Figure 4.18). While the setup is scanning the tested sample, the map of 2D spatial spectrums in HDR is created (Figure 4.19) and also the FT HP filtered images map is created (Figure 4.20). All these images are also used to generate a report in PDF via LaTeX engine automatically. The report includes all available information about the measurement and the sample. All measured data are also saved in a machine-readable XML file

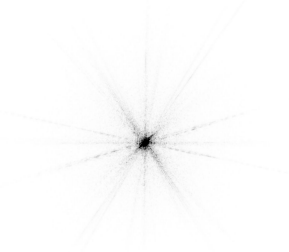

Figure 4.17: Final HDR image of the FT spectrum.

with all source RAW images from cameras. The XML file can be later used for computer analysis of the data. The file also provides all power measurements of the laser and HP power acquired during the measurement.

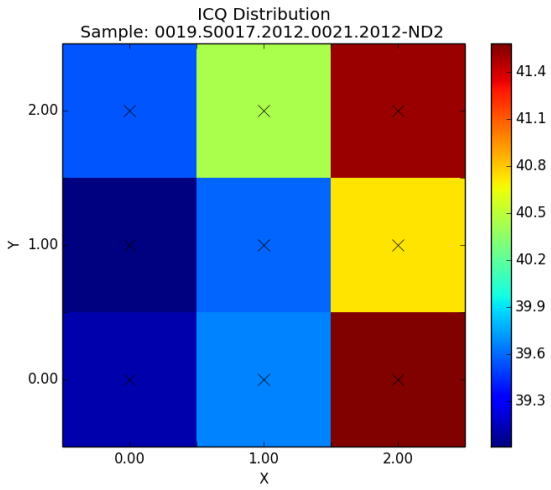


Figure 4.18: ICQ quality map - sample S17.[11]

## 4.9 Photo of the Measuring Setup

Figure 4.1 is a schematical drawing of the real system. Figure 4.21 presents a 3D model of the setup with the description of all parts on the model. The photography of the system is shown in Figure 4.22. The real constructed system differs from Figure 4.1 only in the presence of two mirrors M1 and M2. They are used first to set up the proper alignment of the laser beam to the measuring

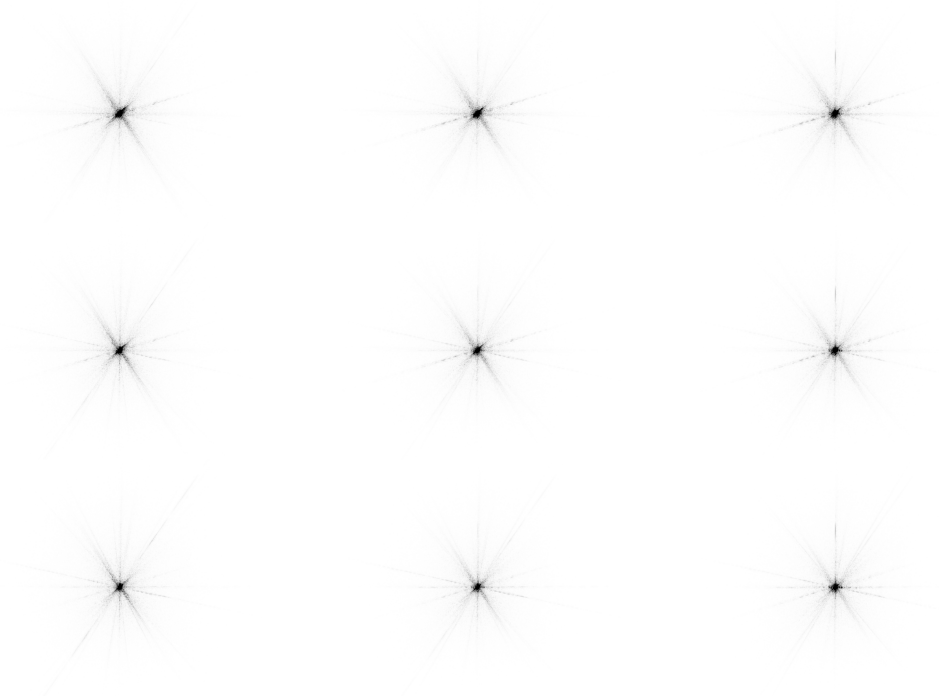

Figure 4.19: Map of 2D FT spatial spectrum.[11]

Figure 4.20: Map of 2D FT HP filtered images. Images are processed with a histogram stretching algorithm to gain higher visibility.[11]

system and second to provide a more compact footprint of the system.[11]

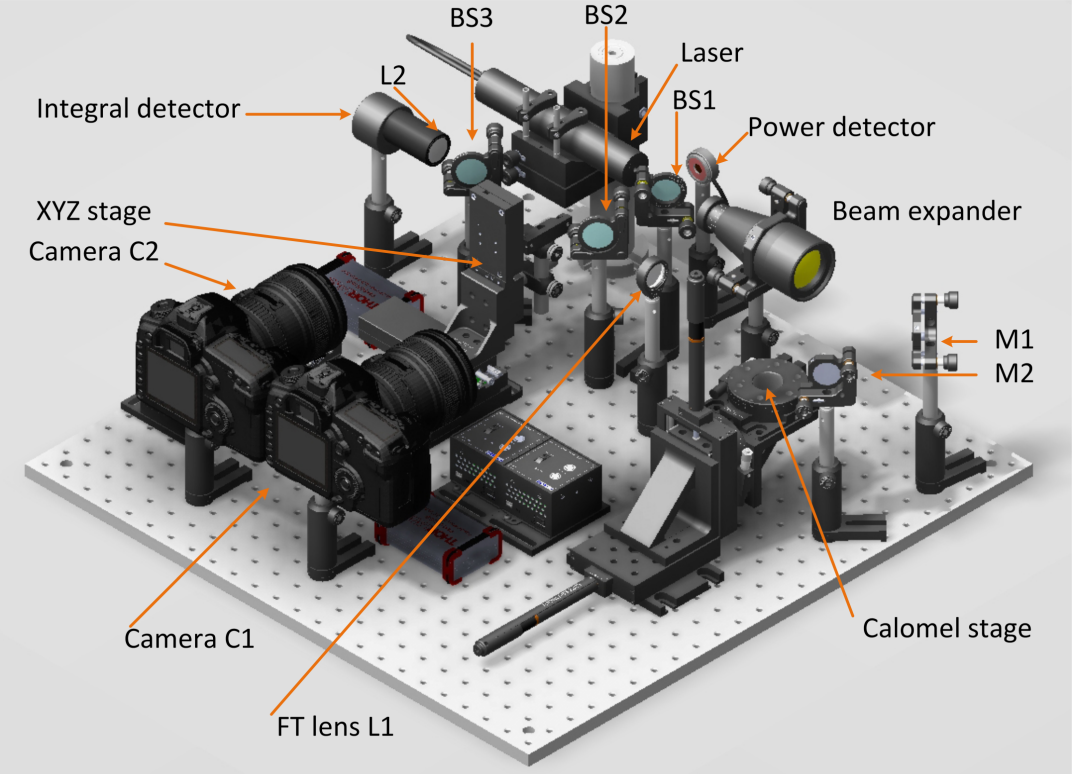


Figure 4.21: 3D drawing of the optical setup with description of all parts.[8]

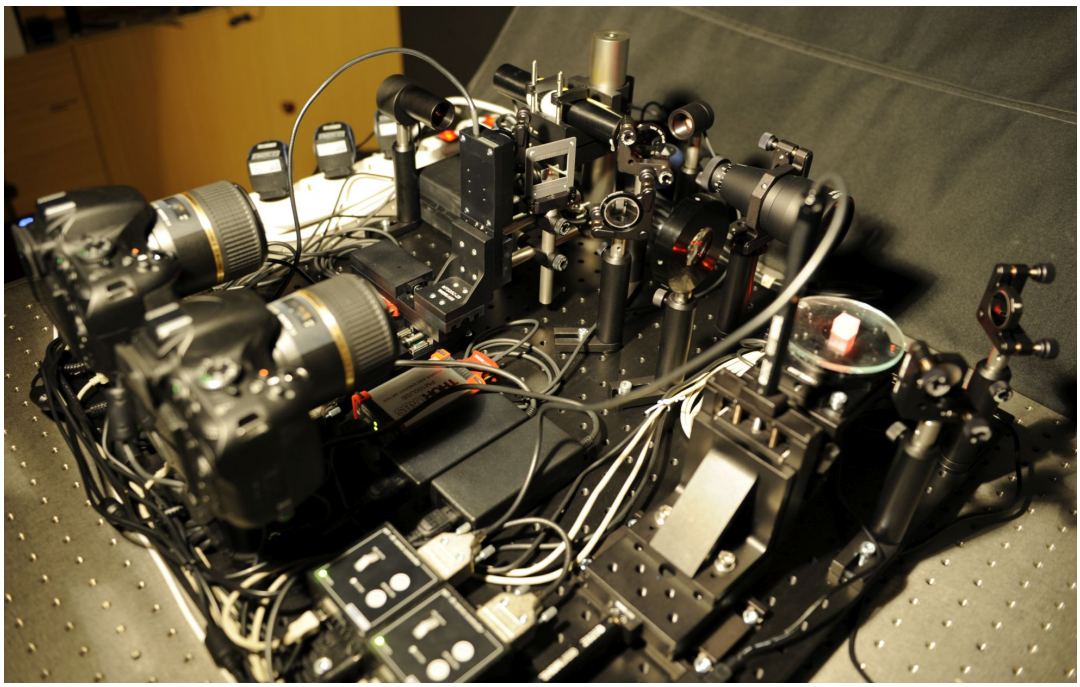

Figure 4.22: Photo of the measuring setup.[11]

# 5 Comparison of Selected Methods

The goal of this section is to select a few evaluation methods described in Section 3 and to compare their results of the quality evaluation. Three methods were selected to compare: the Conoscopy (Section 3.2) as a traditional method used for analysing of the birefringence materials, Light scattering method (Section 3.1) as a fast and straightforward method to study the defects in the material and methods based on Optical Fourier Transformation (Section 3.3) as a novel method.

## 5.1 Optical Fourier Transformation and Light Scattering

The realisation of both OFT and Light scattering optical setups can be combined with one single common setup. The setup is presented in Figure 5.1. The design is based on the setup (Figure 4.1) described in the section devoted to quality evaluation with OFT (Section 4). The setup is expanded with a camera C3. This camera replaces the photodetector with the integrating lens (Figure 3.1). The camera acquires the photo of the tested crystal sample placed on the XY translational stage, and the scattered power is measured by image processing of the picture. Figure 5.2 presents the picture of the optical setup.

Some differences are using the camera instead of the photodetector. First, the photodetector works in connection with the lock-in amplifier and use the synchronous detection to gain high sensitivity and high SNR. Instead of, the camera uses multiple exposures and HDR process (Section 4.7). The second difference is the size of the scanning laser beam. In the OFT setup, the beam is expanded with the beam expander and illuminates a larger surface of the tested sample. The result of higher beam diameter is integrating the influence of the scattering centres (cracks, bubbles,..) from the larger volume of the crystal. The big advantage of combining OFT and Light scattering to single measurement is that all measured parameters are acquired from the same part of the crystal.

### 5.1.1 Scattered Light Power

Figure 5.3a presents an image acquired by the camera C3. In every measuring point (scanning map of the crystal), the camera takes multiple expositions with different length of exposition. The images are merged to HDR image. Then, the central part of the crystal is selected; this is similar to

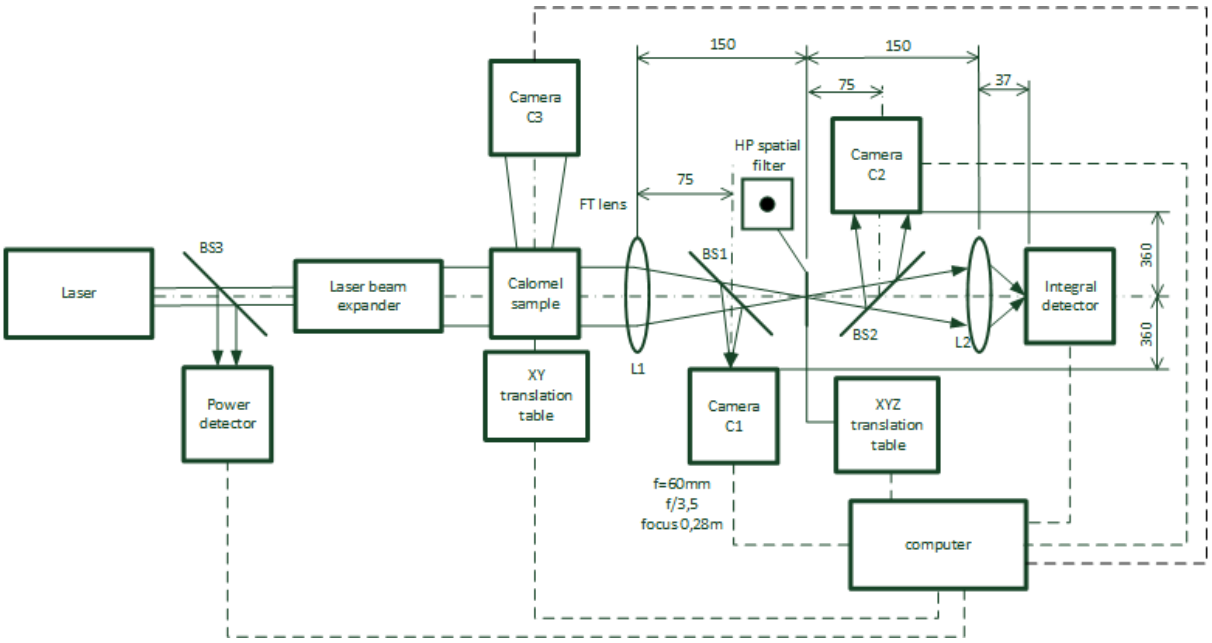


Figure 5.1: Optical setup with combination of Optical Fourier transformation and light scattering setup.

the spatial mask described in Section 3.1.2. The scattered energy $E_i$ is then calculated concerning the area of the crystal Eq 5.1. The selected area marked with the white rectangle in Figure 5.3b.

$$E_i = \frac{1}{N \cdot M} \sum_{n,m=1}^{N,M} E[n, m], \tag{5.1}$$

where the $E_i$ is the calculated energy in measure point $i$, (n,m) are coordinates in the selected part of the picture of size (N, M). The $E[n, m]$ is a value in the image on given coordinates calculated with the HDR process.

The camera has a wide angle shot, on the photo, there is also part of the translational stage and its surrounding. Figure 5.4 shows the acquired picture with the longest exposure time (8s, ISO 200) used for measuring the scattered light and a white-light photo of the same crystal.

### 5.1.2 Experimental Results

Outputs of this combined system are described in previous Sections 4.8 and 3.1.3. For every tested crystal, there are multiple measured properties and data available for evaluating:

- Spatial spectrum images (Figure 5.5a),
- HP filtered images (Figure 5.5b),

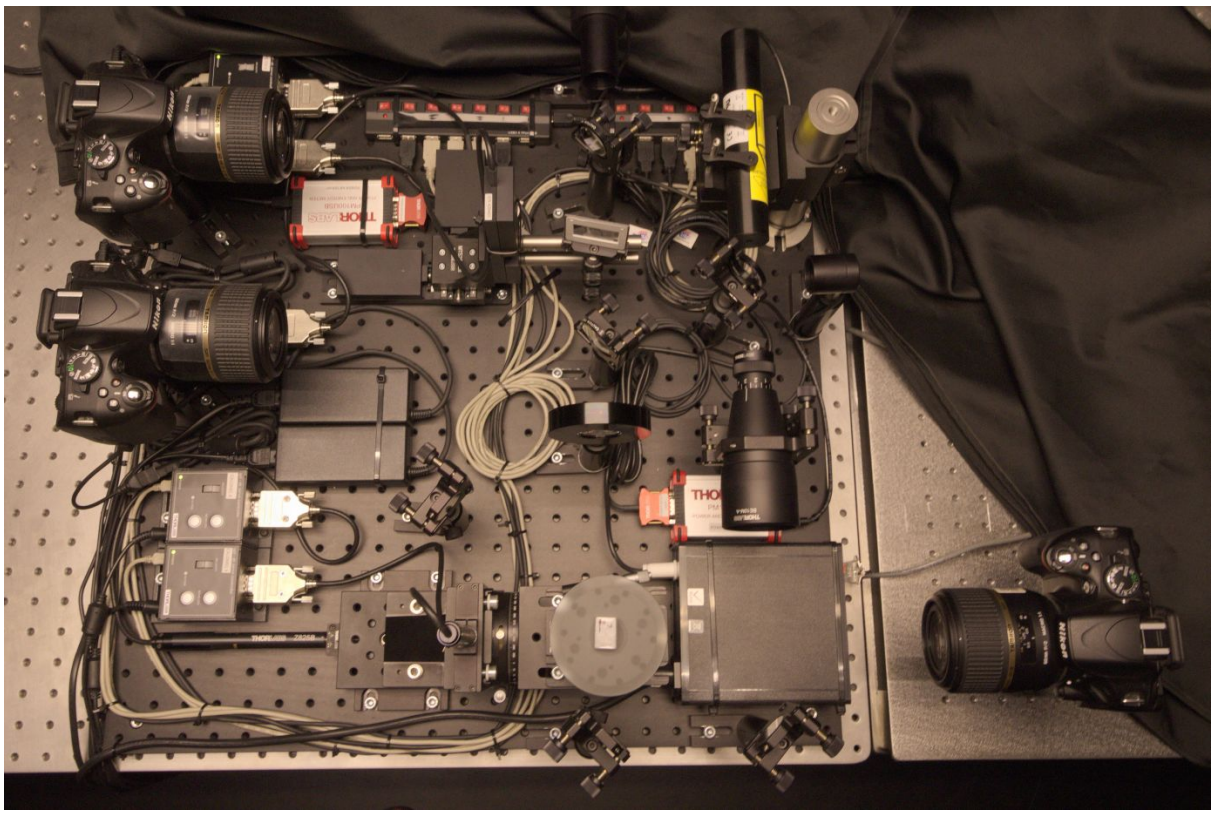

Figure 5.2: Photo of the tested optical setup combined from OFT and light scattering systems.

- ICQ quality map (Figure 5.5c),
- Scattered light power map (Figure 5.5d).

The ICQ quality map and the map of scattered light contain directly numeric values that can be compared together to get a relation between them. The comparison of these datasets is in Section 5.3.

## 5.2 Conoscopy

The conoscopy is a standard and widely used method for the evaluation of optical birefringent materials. It is also a reliable method for designation the optical axis of the material, which turns out to be a method used for material orientation in the material processing and optical elements manufacturing.

(a) a (b) a

Figure 5.3: The image acquired by the camera (a) and the cropped picture of the sample. The white rectangle is the selected area of the crystal (b).

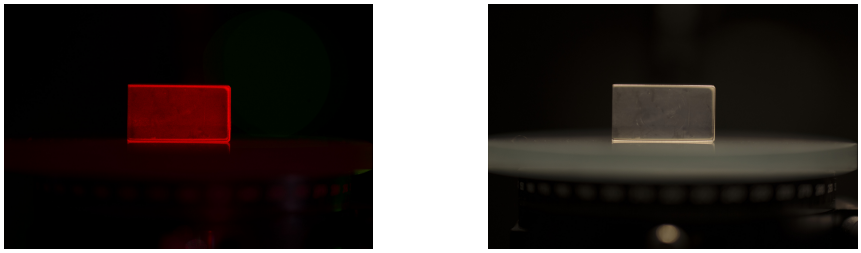

(a) a (b) b

Figure 5.4: Presentation of the wide imaging angle of the camera C3: the photo of the tested sample during the measurement (a) and picture acquired with under the white light illumination (b).

### 5.2.1 Setup

The optical setup in Figure 5.6 is based on the configuration described in Section 3.2.1 with only one significant change. The zoom camera optics is removed, and the conoscopic image is projected directly to the camera sensor. A second change is using a small manual tilting stage instead of the rotation stage as the tilting element). The same software used for OFT 4.6 is used for controlling the conoscopic setup. Photo of the optical setup is presented in Figure 5.7.

### 5.2.2 Experimental Results

The controlling system offers the ability to provide the HDR imaging of the conoscopy image automatically. The output is a map of conoscopic images, that can be analysed with the method described in Section 3.2.3. Figure 5.8 demonstrates the output conoscopic map. The evaluation of the conoscopy images and comparison to other methods are discussed in Section 5.3.

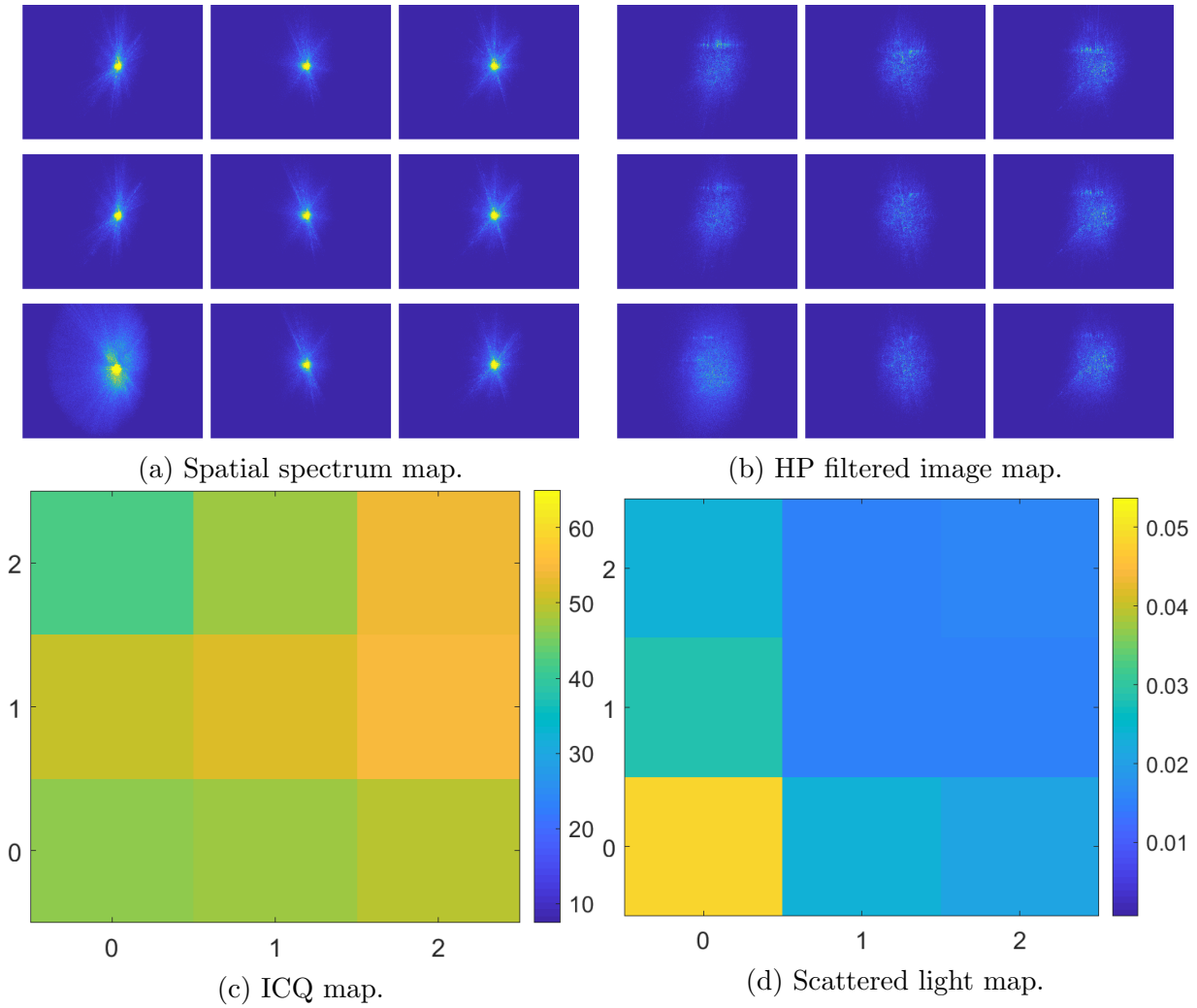


(a) Spatial spectrum map.

(b) HP filtered image map.

(c) ICQ map.

(d) Scattered light map.

Figure 5.5: Example of measured data sets for tested Sample A.

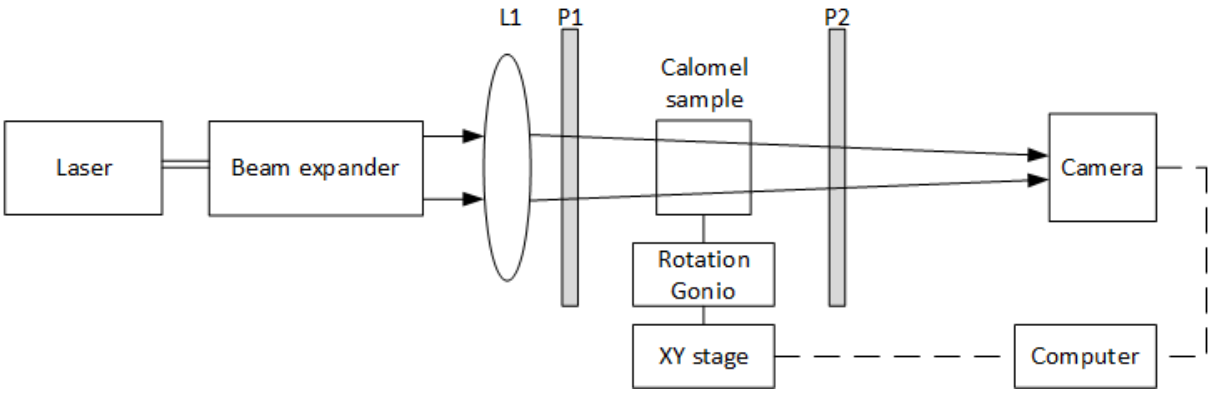


Figure 5.6: Setup of the used conoscopic system.

## 5.3 Methods Comparing

This section is focused on the comparison of a novel method based on Optical Fourier transformation to the light scattering method and a frequently used method of conoscopy imaging. From the OFT method, the ICQ parameter is selected to this comparison. Basic parameters of tested crystal for this comparison are described in Table 2.3. All samples from A to H were tested with all selected methods. Measured values of ICQ, scattered light power and energy calculated from conoscopy are presented in Tables: ICQ -5.1, scattered light - 5.2 and conoscopy - 5.3.

| x | y | Sample A | Sample B | Sample C | Sample D | Sample E | Sample F | Sample G | Sample H |
|---|---|---|---|---|---|---|---|---|---|
| 0 | 0 | 46.6 | 33.6 | 22.3 | 26.7 | 10.8 | 23.8 | 21.8 | 41.3 |
| 1 | 0 | 50.4 | 24.7 | 18.6 | 22.2 | 9.7 | 17.4 | 21.7 | 52.2 |
| 2 | 0 | 42.4 | 24.1 | 16.5 | 29.9 | 8.8 | 40.0 | 27.2 | 65.0 |
| 0 | 1 | 47.2 | 38.9 | 20.5 | 27.6 | 15.4 | 22.0 | 18.6 | 42.0 |
| 1 | 1 | 52.4 | 23.4 | 17.4 | 21.6 | 11.0 | 18.3 | 16.8 | 46.7 |
| 2 | 1 | 47.4 | 20.7 | 15.6 | 33.1 | 8.0 | 29.9 | 24.1 | 58.7 |
| 0 | 2 | 49.5 | 38.6 | 22.5 | 25.9 | 12.0 | 17.7 | 29.1 | 49.8 |
| 1 | 2 | 54.6 | 24.9 | 17.6 | 22.1 | 7.5 | 18.8 | 28.2 | 44.8 |
| 2 | 2 | 53.7 | 19.6 | 16.8 | 31.6 | 10.6 | 21.1 | 33.0 | 63.8 |

Table 5.1: ICQ values.

Let us take a closer look to properties of tested samples in Table 2.3, especially on orientation and number of polished surfaces. To be able to compare parameters, crystals have to be similar, i.e. the same orientation towards the optical axis. The optical axis of crystals is oriented in the direction [001], i.e. when the light is parallel to the optical axis of the crystal, surfaces (001) have to be polished. But Sample A has only (110) polished surfaces, the crystal is oriented perpendicular to the optic path. This is observed from the conoscopy image (Figure 5.8). It means it is not suitable to use Sample A conoscopy results into the comparison. The second measurement in this comparison is the system based on the scattered light. In the setup (principally schema in Figure 3.1), the light passes thru the sample, and the scattered light is measured in the perpendicular direction to the

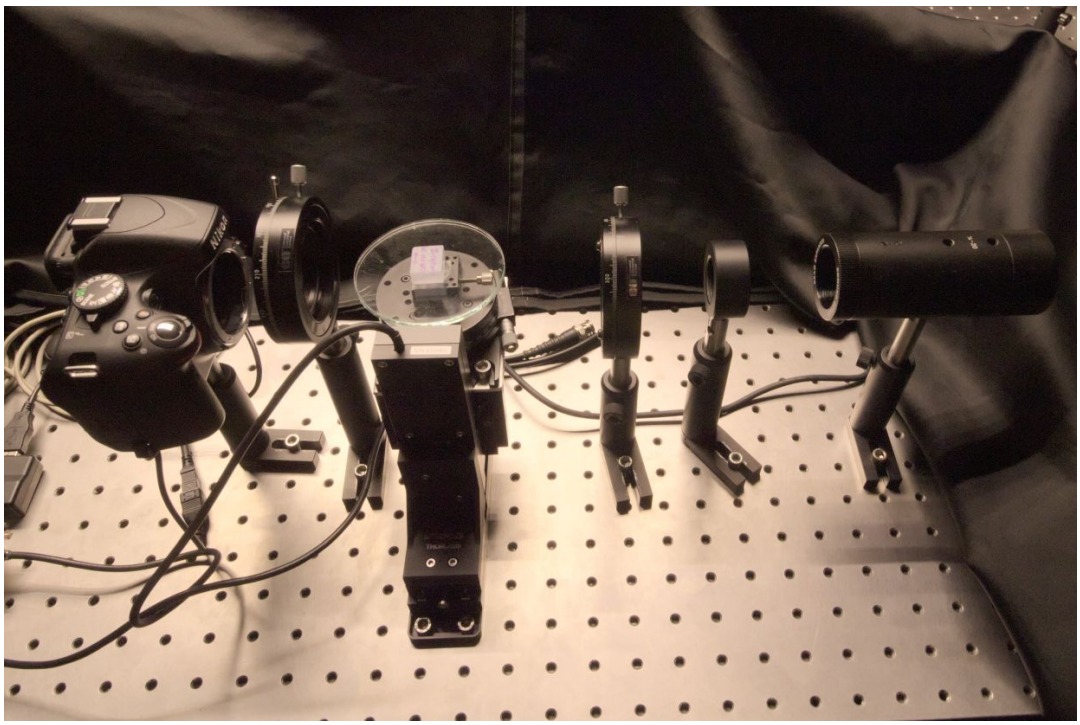

Figure 5.7: Picture of the used conoscopic system.

light axis. This requires polished surfaces in the optical path (001) and also polished surfaces in the perpendicular direction (110). Samples B, F, G and H matches this condition. This mean, we can compare:

- - ICQ and scattered light: Samples B, F, G, H
- - ICQ and conoscopy: Samples B, C, D, E, F, G, H.

Figure 5.9 presents a comparison between values of ICQ and scattered light power. The lower the ICQ value, the better quality the crystal is. It means that the light is less scattered in the direction parallel to the optical axis. The same should be true for the scattered light in the perpendicular direction. There is no strong relationship between those values. If we take a look at Figure 2.2, samples G and H have not nice polished surface, but a dirty one. This is done by applying the external environment, and it is a problem for all Calomel surfaces. This may lead to improper values of scattered light.

Figure 5.10 presents a comparison between the ICQ and a calculated energy value of conoscopic image (Eq 3.4). This comparison seems to be misleading. The conoscopy has a different meaning than the light scattering. The shape of the conoscopy image provides more information. From the shape, we can derive if the material is in good condition or if there is some mechanical stress causing the biaxiality of the material. All conoscopy images are on Figure 5.11. We can see, that Sample E has a typical undeformed Malta cross and the material is in good condition. Sample A, as mentioned before, has characteristic shape of the conoscopy image in the direction parallel to

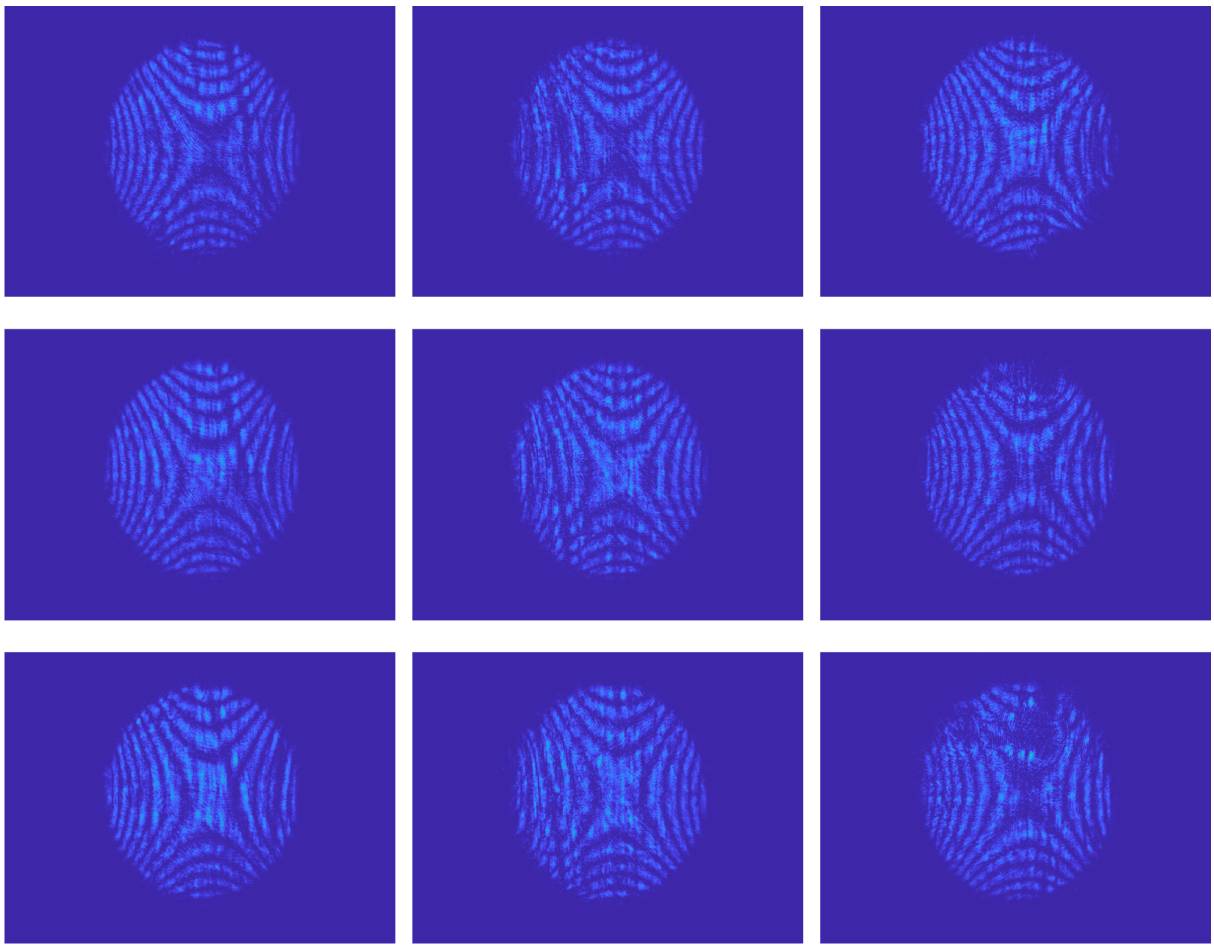

Figure 5.8: Map of conoscopic pictures for tested Sample A.

the optical axis. Other samples exhibit the presence of stress in the material, with the damaged conoscopy image.

| x | y | Sample A | Sample B | Sample C | Sample D | Sample E | Sample F | Sample G | Sample H |
|---|---|---|---|---|---|---|---|---|---|
| 0 | 0 | 4.83E-02 | 3.58E-03 | 4.74E-02 | 1.28E-02 | 1.44E-02 | 3.85E-03 | 8.63E-03 | 5.72E-03 |
| 1 | 0 | 2.88E-02 | 2.17E-03 | 4.20E-02 | 1.10E-02 | 1.92E-02 | 2.28E-03 | 7.43E-03 | 5.86E-03 |
| 2 | 0 | 2.31E-02 | 2.35E-03 | 5.38E-02 | 1.22E-02 | 1.95E-02 | 2.42E-03 | 4.09E-03 | 6.33E-03 |
| 0 | 1 | 2.31E-02 | 2.21E-03 | 5.08E-02 | 1.35E-02 | 2.20E-02 | 2.33E-03 | 2.87E-03 | 7.04E-03 |
| 1 | 1 | 1.50E-02 | 2.00E-03 | 4.89E-02 | 9.01E-03 | 2.17E-02 | 2.19E-03 | 2.48E-03 | 4.39E-03 |
| 2 | 1 | 1.55E-02 | 2.15E-03 | 3.87E-02 | 9.15E-03 | 1.83E-02 | 2.59E-03 | 2.49E-03 | 2.59E-03 |
| 0 | 2 | 2.10E-02 | 1.35E-03 | 3.92E-02 | 1.08E-02 | 1.50E-02 | 1.31E-02 | 1.74E-03 | 1.62E-03 |
| 1 | 2 | 1.52E-02 | 1.27E-03 | 4.36E-02 | 9.33E-03 | 1.13E-02 | 1.95E-02 | 7.35E-03 | 1.00E-03 |
| 2 | 2 | 1.63E-02 | 1.42E-03 | 5.38E-02 | 9.93E-03 | 1.22E-02 | 2.28E-02 | 7.12E-03 | 6.24E-04 |

Table 5.2: Power of scattered light.

| x | y | Sample A | Sample B | Sample C | Sample D | Sample E | Sample F | Sample G | Sample H |
|---|---|---|---|---|---|---|---|---|---|
| 0 | 0 | 4.04E+05 | 4.58E+05 | 5.91E+04 | 3.26E+05 | 4.83E+05 | 4.41E+05 | 5.83E+05 | 5.49E+05 |
| 1 | 0 | 2.87E+05 | 3.12E+05 | 2.51E+04 | 3.09E+05 | 4.42E+05 | 4.74E+05 | 6.68E+05 | 5.77E+05 |
| 2 | 0 | 2.70E+05 | 6.53E+05 | 2.36E+04 | 2.88E+05 | 3.71E+05 | 4.33E+05 | 5.39E+05 | 4.90E+05 |
| 0 | 1 | 2.97E+05 | 6.42E+05 | 4.24E+04 | 3.56E+05 | 3.57E+05 | 4.39E+05 | 3.74E+05 | 5.27E+05 |
| 1 | 1 | 3.06E+05 | 5.56E+05 | 1.68E+04 | 4.26E+05 | 3.62E+05 | 3.50E+05 | 4.45E+05 | 6.72E+05 |
| 2 | 1 | 2.94E+05 | 5.12E+05 | 1.22E+04 | 2.43E+05 | 4.68E+05 | 3.62E+05 | 5.61E+05 | 7.08E+05 |
| 0 | 2 | 1.81E+05 | 4.85E+05 | 3.10E+04 | 3.28E+05 | 3.45E+05 | 4.12E+05 | 5.36E+05 | 5.59E+05 |
| 1 | 2 | 1.94E+05 | 6.55E+05 | 1.90E+04 | 4.51E+05 | 5.03E+05 | 4.00E+05 | 6.03E+05 | 4.93E+05 |
| 2 | 2 | 3.81E+05 | 4.86E+05 | 1.51E+04 | 2.52E+05 | 4.15E+05 | 4.67E+05 | 6.69E+05 | 6.06E+05 |

Table 5.3: Conoscopy energy.

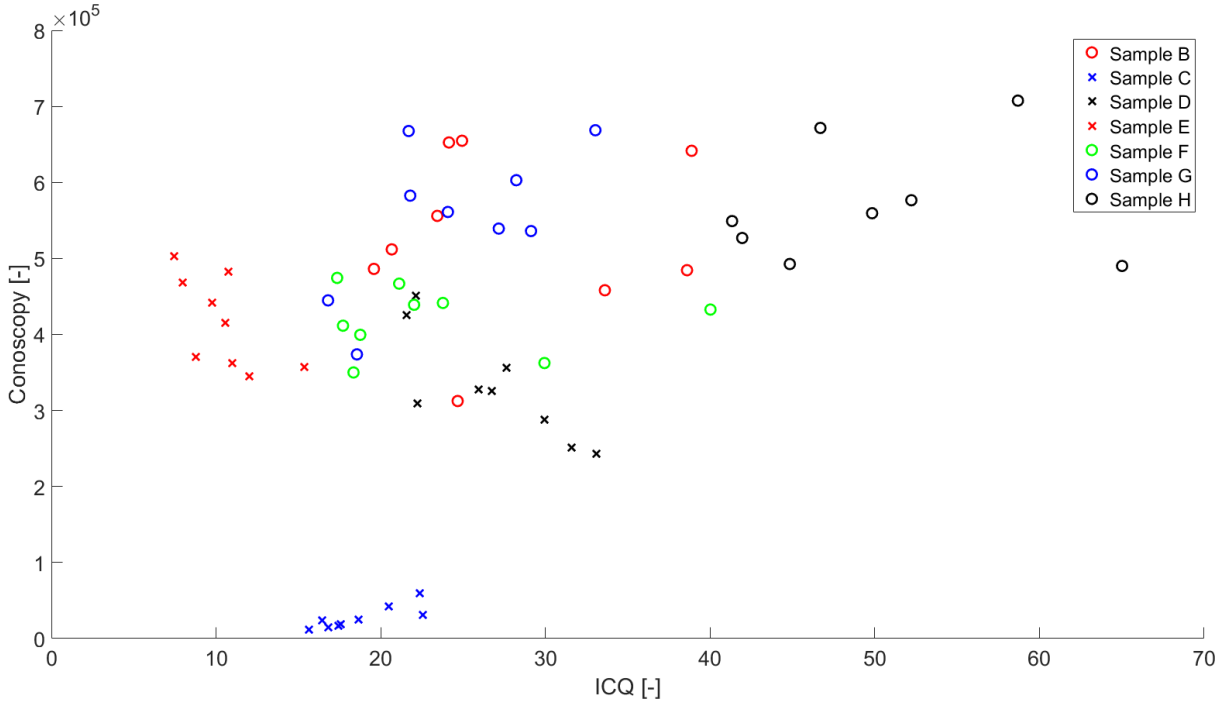


Figure 5.9: Dependency between ICQ value and scattered light power for different crystals..

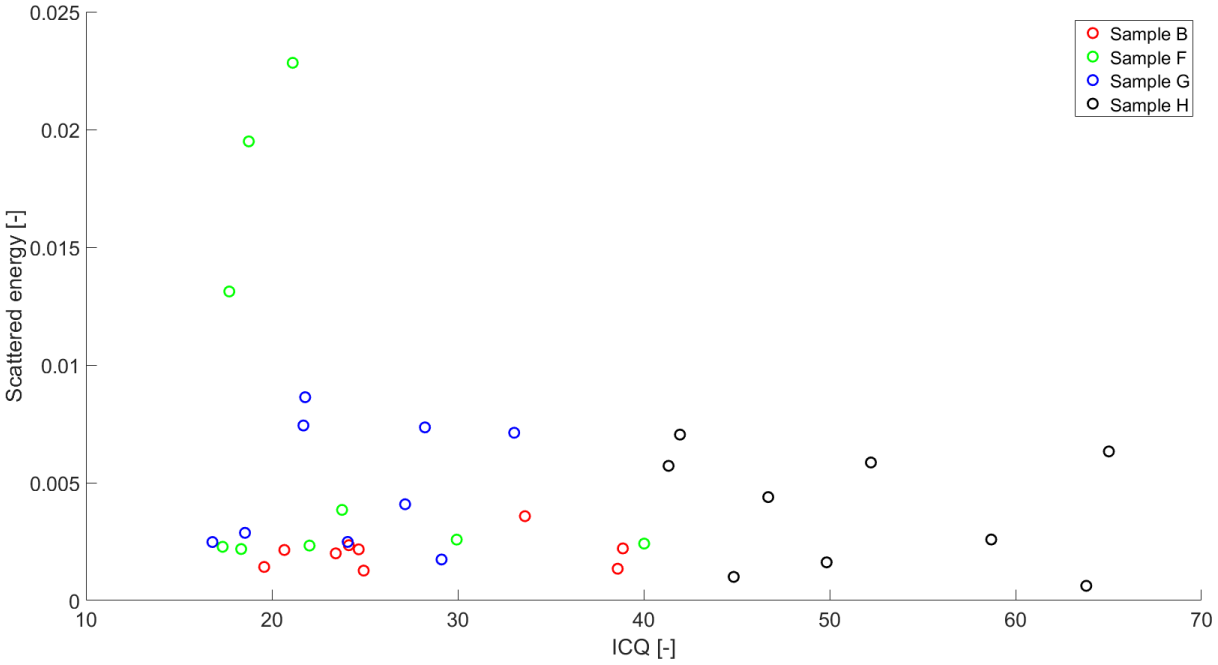


Figure 5.10: Dependency between ICQ value and energy calculated from conoscopic image for different crystals.

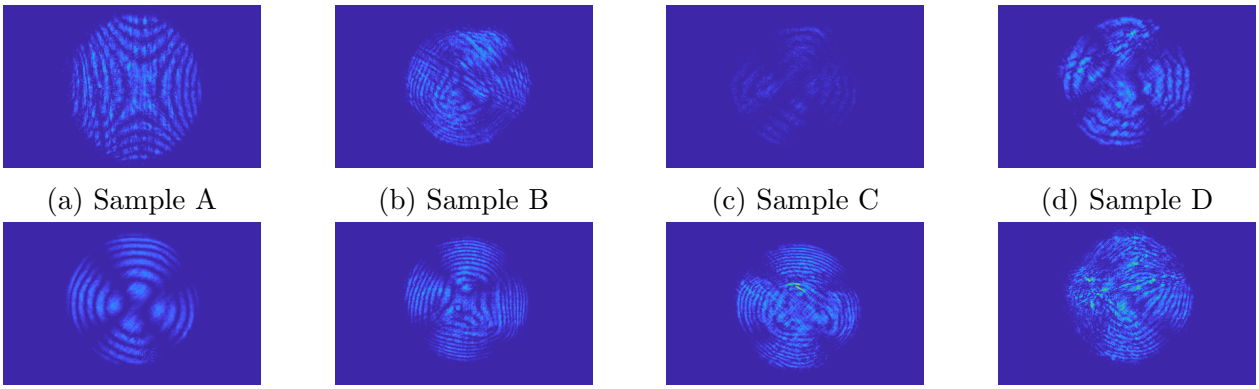

(a) Sample A (b) Sample B (c) Sample C (d) Sample D

(e) Sample E (f) Sample F (g) Sample G (h) Sample H

Figure 5.11: Comparison of conoscopic images (X1y0) of all tested samples.

# 6 Conclusions

Quality Evaluation Methods for Advanced Optical Materials focuses on methods for quality assessment of optical crystalline materials with respect to Calomel crystals. The thesis presents multiple methods for crystal quality evaluation, their properties and compares them to the method based on Optical Fourier transformation.

## 6.1 Summary

The thesis is divided into six parts covering the material description, selection and description of multiple methods for testing the quality of optical materials, development of automated measurement system for quality evaluation and the comparison of selected methods.

Chapter 1 introduces the known description of optical systems with PSF and with the wavefront aberration. There are presented works concerning the spatial variation of PSF. In the second part, it provides related works to the optical quality evaluation focused on both surface and volume quality evaluation methods.

Chapter 2 introduces the Calomel as a modern optical material with promising applications in the LWIR region. This material

Chapter 3 describes multiple selected methods used to determinate the quality of the material. Initial tests of methods are provided. The method based on OFT is described, the OFT is derived, and spatial filtration with OFT optical system is presented.

The OFT setup is selected to be developed into an automated quality evaluating system. Chapter 4 describes this system in detail, its properties, the controlling system and method for evaluating spatial Fourier spectral images. The quality metric ICQ is here presented.

In Chapter 5 are compared results from three different methods. It turns out, that is better to use the conoscopy image directly to assess its shape. The crystal without any internal mechanical stress provides a true Malta cross image. Otherwise, the conoscopy image shows high distortion leading to bi-axiality. The comparison of the ICQ and the scattered light power in the perpendicular direction is difficult due to the dirty crystal surface. Even though the surface is polished, it is getting dirty

(getting grey) by the environment.

## 6.2 Contributions of the Thesis

- Novel method for quality evaluation of optical crystals based on Optical Fourier transformation providing multiple different outputs: the spatial Fourier spectrum, HP filtered image and value of ICQ.
- Optical setup realising the OFT method (Section 4) with software control is presented. This automated setup is used in the BBT Materials processing company for the quality evaluation of produced Calomel crystals.
- Method for analysing the spatial Fourier spectral images from the OFT setup (Section 4.5)[10].
- Comparision of different quality evaluation methods.

## 6.3 Future Work

The thesis describes of methods for quality evaluation of optical crystals. Future work should be address to a deeper understanding of the influence of the inner crystal structure to measured parameters. The future works should also be focused on improving the crystal production process (crystal growth, crystal processing) according to the analysis of tested samples, their quality properties and the dependence on their process of production.

# Bibliography

[1] P. Páta, M. Klíma, J. Bednář, P. Janout, C. Barta, and R. Hasal. Development of quality evaluation methods for calomel optical elements - requirements review. Technical Report TN6, CTU in Prague, BBT-Materials Processing, 2012.

[2] P. Páta, M. Klíma, J. Bednář, P. Janout, C. Barta, and R. Hasal. Development of quality evaluation methods for calomel optical elements - detailed assessment of the two testing techniques and definition of the final testing approach. Technical Report TN8, CTU in Prague, BBT-Materials Processing, 2012.

[3] Polariscope - The Gemology Project.

[4] Li Bin. Fourier Transform Optics, 2001.

[5] M. V. Mantravadi and D. Malacara. Newton, Fizeau, and Haidinger Interferometers. In *Optical Shop Testing*, pages 1–45. John Wiley & Sons, Ltd, 2006.

[6] Optical flats. http://www.edmundoptics.com/resources/application-notes/optics/optical-flats/. Accessed: 20116-11-16.

[7] P. Páta, M. Klíma, J. Bednář, P. Janout, C. Barta, and R. Hasal. Thermal hyperspectral imaging system breadboard requirement definition and design - optical tests design report. Technical report, CTU in Prague, BBT-Materials Processing, 2017.

[8] P. Páta, M. Klíma, J. Bednář, P. Janout, C. Barta, and R. Hasal. Development of quality evaluation methods for calomel optical elements - review of experimental methods for testing calomel material quality and identification of two best approaches. Technical Report TN9, CTU in Prague, BBT-Materials Processing, 2012.

[9] P. Páta, M. Klíma, J. Bednář, P. Janout, C. Barta, and R. Hasal. Development of quality evaluation methods for calomel optical elements - test results analysis report. Technical Report TN7, CTU in Prague, BBT-Materials Processing, 2014.

[10] P. Páta, M. Klíma, J. Bednář, P. Janout, C. Barta, R. Hasal, L. Maresi, and S. Grabarnik. OFT Sectorization Approach to Analysis of Optical Scattering in Mercurous Chloride Single Crystals. 23(16), 2015. Citation Key: Pata15:230788.

[11] P. Páta, M. Klíma, J. Bednář, P. Janout, C. Barta, and R. Hasal. Development of quality evaluation methods for calomel optical elements - design of calomel test setup. Technical Report TN10, CTU in Prague, BBT-Materials Processing, 2013.

[12] BBT Material Processing. About Calomel – Calomel. http://www.calomel.cz/products/about-calomel/, 2019.

[13] Marvin J. Weber. *Handbook of optical materials*. The CRC Press laser and optical science and technology series. CRC Press, Boca Raton, 2003.

[14] C. Barta and Jr. Barta. Physical Properties of single crystals of the Calomel group (Hg2x2 ). *I.Gregora, Proc.Symposium on mercury(I)halides, Liblice*, 1976:91, 1976.

[15] P. Páta, M. Klíma, J. Bednář, P. Janout, C. Barta, and R. Hasal. Demon - development of quality evaluation methods for calomel optical elements. Technical report, CTU in Prague, BBT-Materials Processing, 2012-2014.

[16] P. Páta, M. Klíma, J. Bednář, P. Janout, C. Barta, and R. Hasal. Thetis - thermal hyperspectral imaging system breadboard requirement definition and design. Technical report, CTU in Prague, BBT-Materials Processing, 2017.

[17] von F. Zernike. Beugungstheorie des schneidenver-fahrens und seiner verbesserten form, der phasenkontrastmethode. *Physica*, 1(7-12):689–704, May 1934.

[18] Robert J. Noll. Zernike polynomials and atmospheric turbulence*. *JOSA*, 66(3):207–211, March 1976.

[19] H. H. Hopkins. Image formation by a general optical system. 1: General theory. *Applied Optics*, 24(16):2491, August 1985.

[20] Jingfei Ye, Zhishan Gao, Shuai Wang, Xiaoli Liu, Zhongming Yang, and Congyang Zhang. Bi-Zernike polynomials for wavefront aberration function in rotationally symmetric optical systems. In *Renewable Energy and the Environment (2013), paper JM3A.6*, page JM3A.6. Optical Society of America, November 2013.

[21] Petr Janout, Petr Pata, Petr Skala, and Jan Bednář. PSF Estimation of Space-Variant Ultra-Wide Field of View Imaging Systems, 2017.

[22] Petr Janout and Petr Páta. Analysis and performance of non-circular polynomials in the wavefront modelling. In *Optical Modeling and Performance Predictions X*, volume 10743, page 107430Q. International Society for Optics and Photonics, September 2018.

[23] Petr Janout, Petr Páta, Jan Bednář, Elena Anisimova, Martin Blažek, and Petr Skala. Stellar objects identification using wide-field camera. page 94501I, Prague, Czech Republic, January 2015.

[24] J. Bednar, P. Skala, and P. Pata. Toward astrometric calibration of ultrawide-field images. *Astronomische Nachrichten*, 339(5):403–407, 2018.

[25] D.H. Ballard. Generalizing the Hough transform to detect arbitrary shapes. *Pattern Recognition*, 13(2):111–122, January 1981.

[26] Jan Bednář, Petr Skala, and Petr Pata. Pole searching algorithm for Wide-field all-sky image analyzing monitoring system, 2017.

[27] P. V. C. Hough. Machine Analysis of Bubble Chamber Pictures. *Conf.Proc.*, C590914:554–558, 1959.

[28] Edund Optics. Understanding Surface Quality Specifications based on U.S. Standard MIL-PRF-13830b, 2019.

[29] Quentin Turchette and Trey Turner. Developing a more useful surface quality metric for laser optics. page 791213, San Francisco, California, USA, February 2011.

[30] James C Wyant. Introduction to Interferometric Optical Testing. page 109, 2017.

[31] A.I. Kolesnikov, S.A. Tretiakov, R.M. Grechishkin, K.A. Morozova, K.B. Yushkov, V.Ya. Molchanov, and B.B.J. Linde. A Study of Optical Uniformity of Lithium Niobate and Paratellurite Crystals by the Method of Conoscopy. *Acta Physica Polonica A*, 127(1):84–86, January 2015.

[32] Brett L. Van Horn and H. Henning Winter. Analysis of the conoscopic measurement for uniaxial liquid-crystal tilt angles. *Applied Optics*, 40(13):2089–2094, May 2001.

[33] A. I. Kolesnikov, I. A. Kaplunov, A. I. Ivanova, S. A. Tretiakov, I. V. Talyzin, Yu A. Malyshkin, R. M. Grechishkin, and E. YU Vorontsova. Isochrome Shapes in the Conoscopic Patterns of Uniaxial Crystals. *Ferroelectrics*, 441(1):75–83, January 2012.

[34] Calomel, Hg2cl2, 2018.

[35] Encyclopedia Britannica. Calomel | chemical compound. https://www.britannica.com/science/calomel, 2019.

[36] Calomel, Hg2cl2. http://www.mt-berlin.com/frames_ao/descriptions/calomel.htm, 2019.

[37] Tyndall Effect for Colloidal System - Nanotechnology Review.

[38] Jonathan Blackledge. Electromagnetic Scattering Solutions for Digital Signal Processing. page 298.

[39] J. Bednář, E. Anisimova, P. Janout, and P. Páta. Optick8 Fourierova transformace. 60(11-12), 2015. Citation Key: Bednar15:237948.

[40] Joseph W Goodman. Introduction to Fourier Optics Third Edition. page 98, 2005.

[41] imatest | Image Quality Testing Software & Test Charts.

[42] M. Klíma M. Blažek P. Pata, K. Fliegel and M. Řeřábek. Utilization of consumer level digital cameras in astronomy. *SPIE Optical Engineering+ Applications*, page 77982H–77982H, 2010.

## Publications of the Author Relevant to the Thesis

**Journals with Impact Factor:**

PÁTA, P., et al. OFT Sectorization Approach to Analysis of Optical Scattering in Mercurous Chloride Single Crystals. *Optics Express*. 2015, **23**(16), 21509-21526. ISSN 1094-4087. DOI 10.1364/OE.23.021509.

Shares: 17/17/**17**/17/8/8/8/8

JANOUT, P., et al. PSF Estimation of Space-Variant Ultra-Wide Field of View Imaging Systems. *Applied Sciences*. 2017, **7**(2), ISSN 2076-3417. DOI 10.3390/app7020151. Available from: http://www.mdpi.com/2076-3417/7/2/151

Shares: 25/25/25/**25**

BEDNAR, J. et al. Toward astrometric calibration of ultrawide-field images. Astronomische Nachrichten. 2018, ISSN 0004-6337. DOI 10.1002/asna.201813514

Shares: **33**/33/33

**Reviewed Journals:**

ANISIMOVA, E., J. BEDNÁŘ, and P. PÁTA. The Point Spread Function Variations inside Wide-field Astonomical Images. *Acta Polytechnica*. 2013, **53**(1), 1-4. ISSN 1210-2709.

Shares: 33/**33**/33

ANISIMOVA, E., J. BEDNÁŘ, and P. PÁTA. Zpracování obrazu pomocí vlnkové transformace. *Elektrorevue*. 2013, **15**(4), 238-246. ISSN 1213-1539. Available from: http://elektrorevue.cz/cz/download/zpracovani-obrazu-pomoci-vlnkove-transformace--image-processing-using-the-wavelet-transform-/

Shares: 33/**33**/33

JANOUT, P., et al. Měření vlastností extrémně širokoúhlých zobrazovacích systémů. *Slaboproudý obzor*. 2015, **71**(1), 11-13. ISSN 0037-668X.

Shares: 25/25/**25**/25

BEDNÁŘ, J., et al. Optická Fourierova transformace. *Jemná mechanika a optika*. 2015, **60**(11-12), 311-313. ISSN 0447-6441.

Shares: **25**/25/25/25

ANISIMOVA, E., J. BEDNÁŘ, and P. PÁTA. Astronomical Image Denoising using Curvelet and Starlet Transform. In: *Proceedings of 23th International Conference RADIOELEKTRONIKA 2013*. Radioelektronika 2013, Pardubice, 2013-04-16/2013-04-18. Pardubice: Univerzita Pardubice, 2013. p. 255-260. ISBN 978-1-4673-5516-2. DOI 10.1109/RadioElek.2013.6530927.

Shares: 33/**33**/33

ANISIMOVA, E., J. BEDNÁŘ, and P. PÁTA. Efficiency of Wavelet Coefficients Thresholding Techniques used for Multimedia and Astronomical Image Denoising. In: *18th 2013 International Conference on Applied Electronics*. 18th International Conference on Applied Electronics 2013, Plzeň, 2013-09-10/2013-09-12. Pilsen: University of West Bohemia, 2013. p. 25-28. ISSN 1803-7232. ISBN 978-80-261-0166-6.

Shares: 33/**33**/33

ANISIMOVA, E., et al. Analysis of images obtained from space-variant astronomical imaging systems. In: TESCHER, A. G., ed. *Applications of Digital Image Processing XXXVI*. San Diego, California, 2013-08-25/2013-08-29. Bellingham (stát Washington): SPIE, 2013. p. 885607-1-885607-11. ISSN 0277-786X. ISBN 9780819497062. DOI 10.1117/12.2023904.
Shares: 12.5/12.5/12.5/12.5/**12.5**/12.5/12.5/12.5

ANISIMOVA, E., et al. Estimation and measurement of space-variant features of imaging systems and influence of this knowledge on accuracy of astronomical measurement. In: TESCHER, A. G., ed. *Applications of Digital Image Processing XXXVII*. San Diego, California, 2014-08-17/2014-08-21. Bellingham: SPIE, 2014. p. 92171E-1-92171E-13. Proceedings of SPIE. ISSN 0277-786X. ISBN 978-1-62841-244-4. DOI 10.1117/12.2061736.

Shares: 12.5/12.5/12.5/12.5/**12.5**/12.5/12.5/12.5

FLIEGEL, K., et al. Performance evaluation of image deconvolution techniques in space-variant astronomical imaging systems with nonlinearities. In: TESCHER, A. G., ed. *Applications of Digital Image Processing XXXVIII*. San Diego, California, 2015-08-09/2015-08-13. Bellingham: SPIE, 2015. p. 959927-1-959927-14. Proceedings of SPIE. ISSN 0277-786X. ISBN 978-1-62841-765-4. DOI 10.1117/12.2187888.

Shares: 14.3/14.3/**14.3**/14.3/14.3/14.3/14.3

JANOUT, P., et al. Application of field dependent polynomial model. In: TESCHER, A. G., ed. *Applications of Digital Image Processing XXXIX*. San Diego, California, 2016-08-29/2016-09-01. Bellingham: SPIE, 2016. p. 99710F-1-99710F-9. Proceedings of SPIE. ISSN 0277-786X. ISBN 978-1-5106-0333-2. DOI 10.1117/12.2237310.

Shares: 16.7/16.7/16.7/16.7/16.7/**16.7**

KLÍMA, M., et al. Experimental setup for the quality evaluation of optical materials. In: *2018 28th International Conference Radioelektronika*. 28th International Conference Radioelektronika 2018, Praha, 2018-04-19/2018-04-20. IEEE (Institute of Electrical and Electronics Engineers), 2018. p. 1-4. ISBN 978-1-5386-2485-2. DOI 10.1109/RADIOELEK.2018.8376400. Available from: https://ieeexplore.ieee.org/document/8376400/

Shares: 16.7/16.7/**16.7**/16.7/16.7/16.7

JANOUT, P., et al. Stellar objects identification using wide-field camera. In: TOMÁNEK, P., D. SENDERÁKOVÁ, and P. PÁTA, eds. *Proc. SPIE 9450, Photonics, Devices, and Systems VI*. Photonics Prague 2014, Prague, 2014-08-27/2014-08-29. Bellingham: SPIE, 2015. p. 94501I-1-94501I-9. Proceedings of SPIE. ISSN 0277-786X. ISBN 978-1-62841-566-7. DOI 10.1117/12.2074255.

Shares: 16.7/16.7/**16.7**/16.7/16.7/16.7

**Remaining Publications of the Author**

PÁTA, P., P. JANOUT, and J. BEDNÁŘ. *Čidlo slunečního svitu*. [Research Report] Praha: ČVUT FEL, Katedra radioelektroniky, 2014.

BEDNÁŘ, J., et al. *Studie k tématu vyhodnocení kvality provedení parkovacího manévru*. [Research Report] Praha: České vysoké učení technické v Praze, Fakulta elektrotechnická, 2015.